# WEAK VALUE AMPLIFICATION: NEW INSIGHTS AND APPLICATIONS

**Luis José Salazar Serrano**

ICFO-INSTITUT DE CIÈNCIES FOTÒNIQUES

&

UPC-UNIVERSITAT POLITÈCNICA DE CATALUNYA

BARCELONA, MAY 2016

# WEAK VALUE AMPLIFICATION: NEW INSIGHTS AND APPLICATIONS

**Luis José Salazar Serrano**

under the supervision of

**Professor Juan P. Torres**

submitted this thesis in partial fulfillment

of the requirements for the degree of

DOCTOR

by the

ICFO-INSTITUT DE CIÈNCIES FOTÒNIQUES

&

UPC-UNIVERSITAT POLITÈCNICA DE CATALUNYA

BARCELONA, MAY 2016

*To my beloved wife Isa,*
*with whom* $1+1$ *is*
*always greater*
*than two*

# ACKNOWLEDGMENTS

This thesis is the result of five years of work at the ICFO - The Institute of Photonic Sciences in Barcelona, Spain and at the Universidad de los Andes in Bogotá, Colombia. During this time I've had a lot of positive, neutral and negative experiences that have allowed me to develop at the personal and scientific level. In particular, I am grateful to all those who directly or indirectly contributed to this work.

I want to first thank my advisors, Professor Juan P. Torres (ICFO) and Professor Alejandra Valencia (Uniandes), for giving me the opportunity to actively participate in their research groups: *quantum engineering of light* at ICFO and *quantum optics laboratory* in Uniandes. I am immensely grateful to them for sharing their experiences, knowledge and their guidance during this process.

Regarding ICFO, I have met wonderful people over these years that have become a second family to Isa, Lía and myself. In particular, I want to thank my compadre Carmelo, Robert, Adam, Jiri, Ion, Rafa, Alberto, Yannick, Ramaiah, Anaid, Val, Pao, Clau, Silvana and Cami for being great company inside and outside the laboratory. I also want to especially thank all the management team that give life to the institute and creates the right environment for research. I also want to especially thank Waldimar, who introduced me to the FBGs and with whom I have enjoyed the most productive coffees of my scientific life. I am also very grateful to David Barrera, Salvador Sales and José Capmany at the ITEAM Research Institute at the Universitat Politècnica de Valencia for fabricating the FBGs and their role in the successful experiment described in Chapter 6.

Regarding Uniandes, I want to thank all the people I had the pleasure of working with in the physics laboratories, in the project of physics outreach demonstrations and on a daily basis. I want to give special thanks to Professor Ferney Rodríguez for accompanying me in the early years of the

doctorate. I am also very grateful to David Guzmán, who allowed me to take the first steps in the laboratory. I want to thank Don Alvaro, Andrés, Johnie, George, Lucho, Janet, Juliet, William and generally the whole team that works in the Physics Department who are behind the scenes making everything work. I also want to thank to my friend Ricardo José Gómez for making the great illustrations of the experimental schemes used in chapters 3, 4 and 7.

Last but not least, I am fortunate to have a family that have always supported and believed in me. I am infinitely grateful to my parents, Luis Ernesto and Gloria, and the whole family: my sister Mariana, Salazares, Serranos, Caicedos and Arbelaez. Finally, and more importantly, there are no words to thank my wife and daughter: Isa and Lía. You are the light that makes me happy every day. I am grateful to life because you accompany me day and night.

# ABSTRACT

Weak Value Amplification (WVA) is a signal enhancement technique proposed in 1988 by Aharonov, Albert, and Vaidman that has been widely used to measure tiny changes that otherwise cannot be determined because of technical limitations. It is based on: i) the existence of a weak interaction which couples a property of a system (the system) with a separate degree of freedom (the pointer), and ii) the measurement of an anomalously large mean value of the pointer state (weak mean value), after appropriate pre and post-selection of the state of the system.

The usefulness of weak value amplification for measuring extremely small quantities has been demonstrated under a great variety of experimental conditions to measure very small transverse displacements of optical beams, beam deflections, angular shifts, temporal shifts, phase shifts, frequency shifts, velocity measurements and temperature differences, among others.

In this thesis we make use of this concept to improve current technologies and analyse the true usefulness of this technique with respect to other experimental alternatives. In particular, we have applied the concept to measure femtosecond temporal delays between pulses much smaller than their pulse width. From the theoretical model we estimate that the ultimate sensitivity of this scheme will allow to measure delays of the order of attoseconds using femtosecond laser sources.

In addition, we have developed an innovative experimental scheme that makes use of the interference effect present in a WVA scheme to generate a highly-sensitive tunable beam displacer that can outperform the limitations imposed by the use of movable optical elements. From the experimental results, we were able to perform a scan of a Gaussian beam with waist $600\,\mu$m over an interval of $240\,\mu$m in steps of $1\,\mu$m.

Moreover, we have implemented a proof-of-concept experiment aimed at increasing the sensitivity of Fiber Bragg Grating (FBG) temperature

sensors. The sensors behave as frequency filters whose center is determined by its surrounding temperature. By means of a WVA scheme we were able to measure a polarization dependent frequency shift that is small compared to the width of each FBG spectrum, and from that value we were able to obtain a four-fold enhancement of the sensitivity with respect to current schemes.

Finally, we address the question of what can offer the concept of WVA and what can not in terms of achieving high sensitivity measurements. By using a specific example and some basic concepts from quantum estimation theory, we have found that while WVA cannot be used to go beyond some fundamental sensitivity limits that arise from considering the full nature of the quantum states, WVA can notwithstanding enhance the sensitivity of *real and specific* detection schemes that are limited by many other things apart from the quantum nature of the states involved, i.e. *technical noise*.

# RESUMEN

Weak Value Amplification (WVA) es una técnica experimental propuesta en 1988 por Aharonov, Albert, y Vaidman que ha sido ampliamente utilizada para medir pequeños cambios de variables físicas que en principio no podrían medirse usando otras metodologías debido a limitaciones técnicas. La técnica se basa en: i) la existencia de una interacción débil que acopla una propiedad de un sistema (el sistema) con otro grado de libertad (el metro), y ii) la medición de un valor promedio particularmente grande del metro (*weak mean value*), después de realizar una selección adecuada de los estados inicial y final del sistema.

La utilidad de la técnica para la medición de cantidades extremadamente pequeñas ha sido demostrada en una gran variedad de condiciones experimentales para medir, por ejemplo, desplazamientos transversales de haces ópticos muy pequeños, deflexiones en haces, corrimientos angulares, retardos temporales, cambios de fase, cambios de frecuencia, mediciones de velocidad y diferencias de temperaturas, entre otros.

En esta tesis, hacemos uso del concepto de *Weak Value Amplification* para mejorar el desempeño de algunos esquemas experimentales actuales y también para analizar la verdadera utilidad de esta técnica con respecto a otras alternativas experimentales.

En particular, aplicamos el concepto para medir retardos temporales entre pulsos del orden de femtosegundos mucho más pequeños que su duración y mediante un modelo teórico, determinamos un límite en la sensibilidad del sistema que permite medir retardos del orden de attosegundos utilizando pulsos del orden de femtosegundos.

También desarrollamos un dispositivo que hace uso de la interfencia presente en los esquemas basados en WVA para generar un desplazador de haz sintonizable que puede superar las limitaciones impuestas en resolución por el uso de elementos ópticos móviles. En particular, reportamos el resul-

tado de realizar un barrido de la posición de un haz Gaussiano, con ancho 600 $\mu$m, a lo largo de un intervalo de 240 $\mu$m en pasos de 1 $\mu$m.

Por otro lado, demostramos la viabilidad del uso del concepto de WVA para aumentar la sensibilidad en sensores de temperatura basados en *Fiber Bragg Gratings* (FBG) a través de un experimento. Teniendo en cuenta de que este tipo de sensores se comportan como filtros espectrales cuya frecuencia central está determinada por la temperatura a su alrededor, con el esquema implementado, hemos podido medir medir corriemientos en frecuencia que son pequeños en comparación con el ancho del espectro de cada FBG. En particular reportamos que el esquema implementado permite mejorar en un factor de cuatro la sensibilidad de los esquemas de medición corrientes.

Por último, buscamos dar respuesta a la pregunta: ¿qué puede y qué no puede ofrecer el concepto de WVA cuando se utiliza en mediciones de gran precisión? Mediante el uso de un ejemplo específico y algunos conceptos básicos de la mecánica cuántica, hemos encontrado que los esquemas basados en WVA no son de utilidad para superar límites fundamentales que surgen al considerar la naturaleza cuántica de la luz. Sin embargo, hemos encontado que el concepto de WVA puede ser de gran utilidad para mejorar la sensibilidad de esquemas experimentales específicos en donde la sensibilidad puede estar limitada por otros factores diferentes a la naturaleza cuántica de la luz, como por ejemplo el ruido técnico.

# LIST OF PUBLICATIONS

Most of the contents of this thesis are published in the following papers:

- J. P. Torres, and **L. J. Salazar-Serrano**, "Weak value amplification: a view from quantum estimation theory that highlights what it is and what isn't," Scientific Reports **6**, 19702 (2016).

- **L. J. Salazar-Serrano**, D. Barrera, W. Amaya, S. Sales, V. Pruneri, J. Capmany, and J. P. Torres, "Enhancement of the sensitivity of a temperature sensor based on fiber Bragg gratings via weak value amplification," Optics Letters **40**, 3962 (2015).

- **L. J. Salazar-Serrano**, D. A. Guzmán, A. Valencia, and J. P. Torres, "Demonstration of a highly-sensitive tunable beam displacer with no use of beam deflection based on the concept of weak value amplification," Optics Express **23**, 10097 (2015).

- **L. J. Salazar-Serrano**, A. Valencia, and J. P. Torres, "Tunable beam displacer," Review of Scientific Instruments **86**, 033109 (2015).

- J. Flórez, J. R. Alvarez, O. Calderó-Losada, **L. J. Salazar-Serrano**, A. Valencia, "Spatial interference of light: transverse coherence and the Alford and Gold effect", arXiv:1510.04397 [physics.optics] (2015). Manuscript submitted for publication.

- **L. J. Salazar-Serrano**, A. Valencia, and J. P. Torres, "Observation of spectral interference for any path difference in an interferometer," Optics Letters **39**, 4478 (2014).

- **L. J. Salazar-Serrano**, D. Janner, N. Brunner, V. Pruneri, and J. P. Torres, "Measurement of sub-pulse-width temporal delays via spectral

interference induced by weak value amplification," Physics Review A **89**, 012126 (2014).

- J. P. Torres, G. Puentes, N. Hermosa, and **L. J. Salazar-Serrano**, "Weak interference in the high-signal regime," Optics Express **20**, 18869 (2012).

Other publications by the author:

- R. de J. León-Montiel, J. Svozilík, **L. J. Salazar-Serrano**, and J. P. Torres, "Role of the spectral shape of quantum correlations in two-photon virtual-state spectroscopy," New Journal of Physics **15**, 053023 (2013).

- **L. J. Salazar-Serrano**, D. A. Guzmán, F. J. Rodríguez, and L. Quiroga, "Quantum-correlated two-photon transitions to excitons in semiconductor quantum wells," Optics Express **20**, 4470 (2012).

# CONTENTS

CONTENTS

CHAPTER

# ONE

# INTRODUCTION

*“ Caminante, no hay camino, se hace camino al andar. ”*

Antonio Machado, *1939*

The progress of scientific research, and the successful development and production of new products and technology, is intimately linked to the continuous improvement in our ability to measure physical quantities of interest with increasing sensitivity. Physical theories are tested with even greater precision, opening doors for new knowledge, and new measuring apparatus with better resolution are engineered.

Experimental science is always looking for the limits to what it can be measured. Sometimes the limits are fundamental. For instance, it is well known that when using photons embedded in a single-mode coherent quantum state, an unknown phase $\varphi$ can be determined with an accuracy $\sqrt{\langle(\Delta\varphi)^2\rangle}$ that goes as $\sqrt{\langle(\Delta\varphi)^2\rangle} \sim 1/\sqrt{N}$ [1]. However, when using entangled NOON states, the accuracy goes as $\sim 1/N$. In both cases, it is the statistical nature of the light beams used that determine the ultimate limit to the sensitivity achievable.

In other occasions, the limits might be due to particular characteristics of the detection system, that effectively limit the sensitivity of the measurement beyond what any more fundamental limit can restrict. For instance, it might happen that the noise added in the detection stage (technical noise) makes impossible to distinguish two close values of the physical quantity of

interest. In this case one can look for methods to circumvent the technical limitation.

In order to pursue this approach, one needs to address what is a measurement and how it works. Using Quantum Mechanics language, a measurement can be thought as a process that involves the interaction between two physical subsystems: "the meter" or device where we will *read* the what is the state of the system, and "the system" to be measured. When the two subsystems interact, a correlation between the meter and the system is generated so that the meter changes according to what is the state of the system. An ideal measurement is characterized by a strong interaction, so that the meter can clearly differentiate between the possible states of the system.

As a result of this, the regime of weak interaction may seem disadvantageous for a measurement, since it is expected to produce an uncertainty in the measurement larger than the difference between readings of the meter for different states of the system. However, in 1988 Aharonov, Albert, and Vaidman [2] showed that when the initial and final states of the system to be measured are selected to be nearly orthogonal, the mean value of the reading of the measuring device (weak value) can take a large value beyond the meter's spectrum of eigenvalues. The effect, generally termed Weak Value Amplification (WVA), generates a mean value that can lay outside the range of small displacements of the pointer of the meter caused by each one of the possible states of the system. Unfortunately, this is also accompanied by a severe depletion of the intensity of the signal detected, due to the quasi-orthogonality of the input and final states of the system. Therefore the applicability of this effect is limited by the sensitivity of the detection stage [3].

Shortly after its introduction, it was recognized that WVA can provide a way to enhance the sensitivity of certain measurements [2]. The key idea is as follows: the value of a variable of interest is extremely small, and a particular measurement scheme produces a correspondingly tiny effect on the meter, so small that cannot be detected. However, in a WVA scheme, the mean value of the reading of the meter can be engineered to be surprisingly large, making possible its detection. In this way extremely small values of a long ensemble of physical quantities have been measured along the years.

Although the concept of WVA originates from research on quantum theory, the phenomenon of weak value amplification can be readily understood in terms of constructive and destructive interference between waves [4]. Indeed, most of the experimental implementations of the concept, since its

first experimental demonstration in 1991 [5], belong to the last type. The usefulness of weak value amplification for measuring extremely small quantities has been demonstrated under a great variety of experimental conditions in numerous scenarios.

In spite of this, there is still an on-going debate about its true nature and whether is really needed for achieving high sensitivity measurements. This debate continues up to the present day. On the one hand, some authors claim that from a fundamental perspective, the use of weak value amplification is not optimum and cannot overcome certain fundamental limits. On the other hand, other authors claim that the use of WVA has been demonstrate to be advantageous in many experiments, showing *real* unprecedented improvements in sensitivity. We address this issue in Chapter 7 of this thesis, trying to reconcile both visions.

This is the scientific area of my PhD Thesis research work, carried out as a result of a collaboration between ICFO - Institute of Photonic Sciences, from Universitat Politècnica de Catalunya (Barcelona, Spain) and Universidad de los Andes (Bogotá, Colombia).

Three are the main goals of this thesis:

- To apply the concept of weak value amplification to certain experimental scenarios for detecting tiny changes of certain physical quantities of interest. More specifically, we want to measure extremely small temporal delays between two pulses much longer that the delay to be measured, and explore how far we can go in this direction. (Chapter 4).

- To design and implement new devices based on the concept of weak value amplification. We demonstrate a compact and tunable beam displacer that does not make use of beam deflection (Chapter 5), and a temperature sensor with enhanced sensitivity based on fiber Bragg gratings technology (Chapter 6).

- To analyze from a fundamental point of view the concept of weak value amplification, to know what it can be done and what it cannot be done. The aim is to reconcile different visions of the technique, and understanding their rationale.

Let us be more specific. In Chapter 2, we introduce and explain the concept of weak value amplification (WVA). This is also addressed in Appendix A. Analyzing the notion of a measurement from a quantum mechanics perspective, we present to the reader the concepts of strong and weak

measurements and the relationship of the latter with the concept of weak value amplification. For clarity's sake, we make use of the first demonstration of the concept as example. Moreover, for the purpose of illustrating its usefulness, we provide examples of experiments used to measure very small quantities ranging from femtosecond time delays, nanoradian beam deflections, phase shifts of the order $\approx 10^{-3}$, and beam deflections with sensitivities of the order of angstroms, among others.

In Chapter 3 we present the connection of WVA with the observation of spectral interference in a Michelson interferometer, regardless of the relationship between the temporal path difference introduced between the arms of the interferometer and the spectral width of the light source. The results obtained show that the concept of weak value amplification, originally born in the realm of quantum optics, can be applied indeed to any system that shows interference, such as the case of classical optics. So here WVA is a tool to reveal interference in an scenario where without WVA such interference effect is not observable.

Chapter 4 presents the results of an experimental scheme devised to measure small temporal delays between pulses much smaller than their pulse width. In particular, we reported the measurement of delays of tens of fs using a laser pulse hundreds of femtosecond long. Since this is a proof-of-concept experiment done with the technology available to us at that moment, we also estimate theoretically the ultimate sensitivity that can be achieved with the scheme demonstrated. The result is that delays of the order of attoseconds using femtosecond laser sources can be measured with present day technology. Also as a product of our experiment, we analyze and perform experiments of weak value amplification in all possible scenarios, both in the low and high signal regimes. Notice that the usual use of WVA is in the low-signal regime where the signal measured is severely depleted.

Chapter 5 present an innovative experimental scheme that makes use of the interference effect present in a WVA scheme to build a highly-sensitive tunable beam displacer that does not use beam deflection to displace the beam. In this way we can overcome certain limitations inherent to the use of optical elements to deflect the beam. The experimental results demonstrate that we are able to shift a Gaussian beam with beam waist $600\,\mu$m over an interval of $240\,\mu$m in steps of $1\,\mu$m.

Chapter 6 presents a proof-of-principle experiment aimed at increasing the sensitivity of Fiber Bragg Grating (FBG) temperature sensors. The sensors behave as frequency filters whose center is determined by its surrounding temperature. By means of a WVA scheme we were able to measure a

temperature-dependent frequency shift that is small compared to the width of each FBG spectrum. The technique requires only linear optics elements for its implementation and provides a fourfold increase in sensitivity over the same FBG system interrogated using standard methods.

Finally, in Chapter 7, we aim at clarifying the puzzle of what the concept of WVA can offer and what cannot when the goal is to increase the sensitivity of measurements. By using a specific example and some basic concepts from quantum estimation theory, we find that while WVA cannot be used to go beyond some fundamental sensitivity limits that arise from considering the full nature of the quantum states, WVA can notwithstanding enhance the sensitivity of *real and specific* detection schemes that are limited by many other things apart from the quantum nature of the states involved, i.e. *technical noise*.

So let us begin by introducing and explaining in detail the concept of weak value amplification, the key concept at the core of this research work.

CHAPTER

# TWO

# WHAT IS WEAK VALUE AMPLIFICATION?

> *The difficulty lies not so much in developing new ideas as in escaping from old ones.*

John Maynard Keynes, *1936*

Weak Value Amplification (WVA) is a technique used in metrology that offers the possibility to measure tiny changes of a variable of interest when *specific* technical considerations pose a limit to the sensitivity that can be achieved otherwise. Moreover, most of the times is straightforward to implement experimentally. It makes use of the weak coupling existing between a property of a system (the system) and a separate degree of freedom (the meter). After appropriate pre- and post-selection of the state of the system, one can measure an anomalously large mean value of the state of the meter (weak value).

At first glance, a measurement based on the weak coupling between two systems or two degrees of freedom can be thought as seemingly disadvantageous, since it is expected to produce an uncertainty in the measurement larger than the values that should be differentiated. However, when appropriate initial and final states of the system to be measured are selected, for instance by choosing them to be nearly orthogonal, the mean value of the reading of the measuring system can yield an unexpectedly large value. This phenomena is generally termed as *weak value amplification* and has proven to be the very useful to measure extremely small quantities under a great variety of experimental conditions.

In this chapter, we introduce the reader to the concept of weak value amplification measurement using the general context of a quantum measurement. For the sake of clarity, we make use of a specific case: an optical analog of the widely known Stern-Gerlach experiment. In Section 2.1, we present the concepts of strong and weak measurements and in Section 2.2 we introduce the main ideas of weak value amplification (WVA) by reviewing the first experimental demonstration of this effect, carried out in 1991 [5]. Moreover, we introduce a more general scheme that goes beyond the weak regime, even though is still based on the main concepts that define weak value amplification. This high signal regime allows to overcome some of the limitations inherent to working in the weak regime., i.e., high losses. Notwithstanding, the weak values obtained might not be so *anomalously large* as in the weak scenario. Finally, in Section 2.3 we discuss briefly some relevant experiments that makes use of real and imaginary weak values.

Since the idea of WVA is the core concept of this thesis, we refer the interested reader to Appendix A for a more detailed presentation of the mathematical formalism behind the concepts of weak measurements and weak values.

## 2.1 Introduction to the concepts of weak measurements and weak values

In general terms, a measurement is a process that makes use of a measuring apparatus that assign a number to a property of an object. The measuring device has a needle or pointer that moves over a scale composed of a discrete set of equally spaced marks by an amount that is directly related to the magnitude of the object's property. The measurement requires that the property of the object is coupled to a certain property of the measuring apparatus. As an example consider a galvanometer, a device used to measure the electric current flowing in a circuit. It is composed of a compass that responds to the strength of a nearby magnetic field. When the galvanometer is connected to the circuit, the deflection of the needle (measuring apparatus) is proportional to the magnitude of the electric current flowing through it (object's property).

In the context of Quantum Mechanics, a measurement turns out to be a more subtle process. On the one hand, it still involves the interaction of two physical objects: "the meter" and "the system" to be measured. When the two subsystems interact, a correlation between the meter and the system

is generated so that a property of the meter changes by an amount related to some observable of the system. On the other hand, the act of measuring disturbs the quantum state of "the system", hence there is no information gain without disturbing its state.

In a measurement, the state of the object is represented mathematically by a quantum state $|\Psi\rangle$, and the observable, what we want to know, is described by an operator $\hat{A}$ with corresponding eigenvalues $a_n$ and eigenvectors $|a_n\rangle$. According to Quantum Mechanics [6], from an ideal measurement we expect that: (i) the possible outcomes of the measurement of the observable $\mathcal{A}$ can be only the eigenvalues of the operator $\hat{A}$; (ii) if the system to be measured is in the state $|\Psi\rangle$, the probability of obtaining the particular eigenvalue $a_i$ is given by $|\langle a_i|\Psi\rangle|^2$, where the quantity $\langle a_i|\Psi\rangle$ is in general complex and is known as the probability amplitude; (iii) after a measurement with result $a_i$, the system is left in the state $|a_i\rangle$.

Let us consider the situation where we want to determine the state of polarization of a Gaussian beam. The beam can be in any of the two orthogonal linear polarizations, that we refer as horizontal or vertical. To perform the measurement, we make use of an uniaxial birefringent crystal that couples the position of the beam in the transverse plane (the meter) with its polarization (the system). In an uniaxial crystal, the optics axis corresponds to a direction of propagation inside the crystal where the two orthogonal polarizations *see* the same index of refraction. For all other angles, if the beam's polarization vector is in the plane formed by the direction of propagation of the beam and the optics axis (principal plane), the crystal behaves as a material with (extraordinary) index of refraction $n_e$, whereas if the polarization vector is perpendicular to the principal plane, the light sees a material with index of refraction $n_o$.

The crystal is prepared in a configuration where a horizontally polarized input beam propagates along the crystal without any change in its direction while a vertically polarized beam is transformed in an output beam that is, due to refraction, displaced spatially with respect to the input beam by a distance that depends on the crystal's length. Figures 2.1(a) and 2.1(b) show the output beam position for an input beam horizontally and vertically polarized, respectively. Fig. 2.1(c) shows the output beam that would be observed for an input beam with a different polarization from 0° and 90°. In this latter case, the input beam is split inside the crystal into two linearly polarized components that propagate in different directions. After a second refraction in the crystal-air interface, the two output beams are spatially separated and propagate in the same direction as the input beam, but one

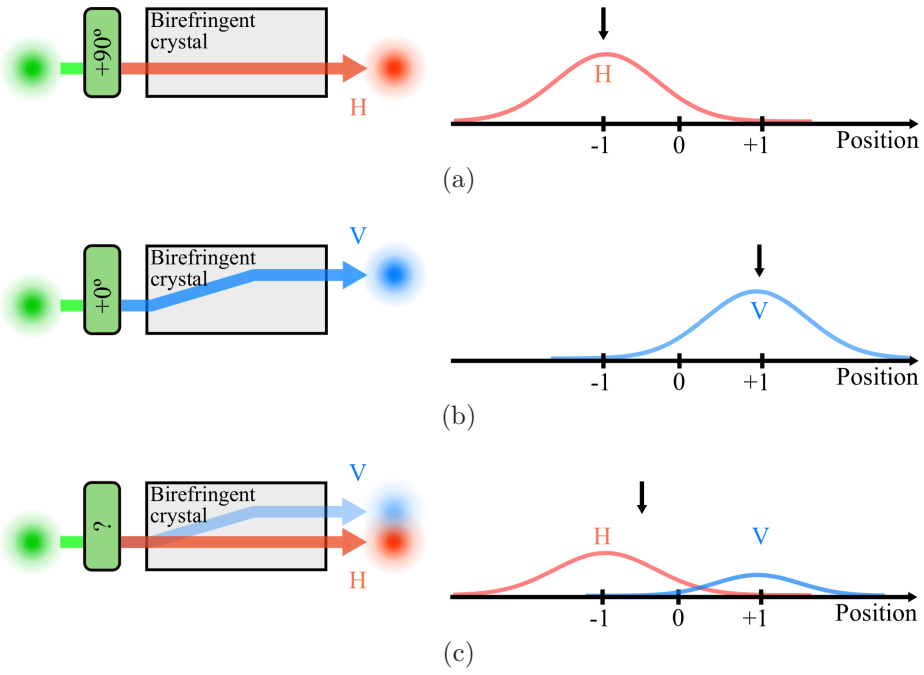


Figure 2.1: (a) Position of the output beam for an input beam with horizontal polarization (90°). For this polarization state, the output beam is centered in the mark $-1$. (b) Output position for an input beam vertically polarized (0°). In this case, the output beam is centered in the $+1$ mark. (c) Expected output beam for an input beam with polarization between 0° and 90°. The mean value of the intensity distribution lies within the interval $[-1, +1]$. In all cases the meter's reading is indicated by a vertical arrow.

spatially displaced respect to the other.

To determine the state of polarization of the input beam, the centroid of the intensity distribution at the output face of the crystal is measured. The centroid (average value) of the intensity distribution lies in a position within the interval $[-1, +1]$ that is directly related to the angle of the input beam plane of polarization. When the input beam is polarized horizontally, the centroid lies in the $-1$ mark; for a vertically polarized beam it lies in the $+1$ mark. For a diagonally polarized beam (45°) the meter points to the central position marked with 0.

Regarding the quantum-mechanics mathematical description of the measurement, the birefringent crystal performs the operation $\hat{P}\,|\Psi\rangle$, where the polarization operator $\hat{P}$ is characterized by the set of eigenvalues $\{-1, +1\}$, the set of eigenvectors $\{|H\rangle\,, |V\rangle\}$, and is defined by $\hat{P} = |V\rangle\langle V| - |H\rangle\langle H|$.

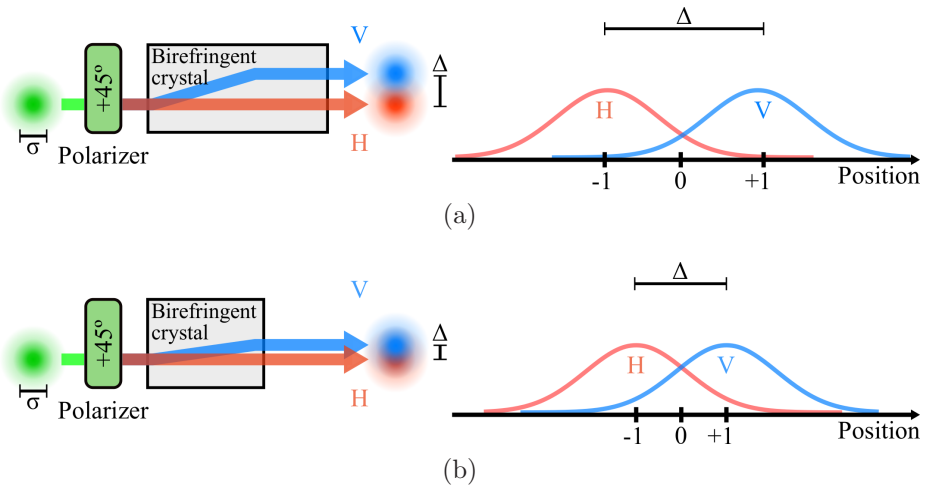


Figure 2.2: (a) Strong measurement. (b) Weak measurement. In general, the strength of the coupling between the input beam polarization and the transverse position of the beam after leaving the crystal is quantified by the separation $\Delta$, and it depends on the amount of birefringence of the crystal and the crystal's length.

Since the input beam state of polarization can be decomposed as $|\Psi\rangle = \cos\theta\,|V\rangle + \sin\theta\,|H\rangle$, the system is left in the state $\hat{P}\,|\Psi\rangle = \cos\theta\,|V\rangle - \sin\theta\,|H\rangle$ after the measurement. To determine the input beam state of polarization, we measure the mean value of $\hat{P}$, $\langle\hat{P}\rangle = \cos 2\theta$, that relates the centroid (mean value) of the intensity distribution after leaving the crystal with the angle $\theta$ that defines the input plane of polarization. Hence, for a beam initially horizontally polarized, $\langle\hat{P}\rangle = -1$ and $\theta = 90°$. Similarly, for a beam vertically polarized $\langle\hat{P}\rangle = +1$ and $\theta = 0°$. Furthermore, if the beam is diagonally polarized, $\langle\hat{P}\rangle = 0$ which corresponds to $\theta = 45°$.

When considering single photons, the measurement described above is consistent with the definition of an ideal measurement according to Quantum Mechanics [6, 7] only when the meter's uncertainty, characterized by the input beam waist $\sigma$ is smaller than the spatial separation between the possible outcomes $\Delta$ (i.e. the distance between $-1$ and $+1$ marks). In this regime, known as *strong measurement*, the result is that: (i) the spatial probability distribution observed after the crystal is composed of sharp peaks centered only on the possible outcomes of the experiment, in this case $\{-1, +1\}$; (ii) the intensity of the peaks observed provide information about the amount of each polarization component present in the input beam; (iii) immediately after the measurement, the beam state of polarization collapses

to the state corresponding to the measured value of the observable.

In the opposite regime, termed *weak measurement*, the short crystal produces a weak coupling that spatially separates very slightly input photons into two parallel streams with orthogonal polarizations, hence, at the output we observe a single spatial distribution of photons centered approximately in the 0 position. Since $\Delta$ is very small compared to the meter spread $\sigma$, the meter's position provides no information about the input state of polarization on a single shot measurement. For this reason, the weak regime was considered as a non-measurement and for decades there was no active research on the topic [8].

Figure 2.2 shows a schematic representation of strong and weak measurements of the state of polarization of an input Gaussian beam (or photons in a spatial Gaussian distribution) using a birefringent crystal. In the case shown in Fig. 2.2(a), a strong coupling between the input beam polarization and its transverse position is generated using a long crystal that produces at the output two well defined peaks centered in the positions $-1$ and $+1$, when the input beam is diagonally polarized ($45°$). On the contrary, the use of a short crystal in Fig. 2.2(b) performs a weak measurement that provides a short separation between orthogonal input polarizations. Notice that in both cases the centroid (mean value) of the intensity distribution at the output lies in between the marks $-1$ and $+1$. However, since the length of the interval $\Delta$ is determined by the crystal's length, a long crystal implements a strong measurement, characterized by $\sigma \ll \Delta$, whereas a short crystal implements a weak measurement where the condition $\sigma \gg \Delta$ holds.

## 2.2 Weak Value Amplification (WVA)

In principle, in the case described in the previous section, the use of a weak measurement scenario for obtaining information about the input state of polarization may seem disadvantageous with respect to choosing a strong measurement, since for a given energy (or number of photons) the uncertainty of the measurement is larger in the weak measurement case. However, in 1988 Yakir Aharonov, Lev Vaidman and David Albert [2, 4] came up with a novel idea that allows to make use of weak measurements to resolve tiny meter shifts. The key element was the inclusion of a post-selection stage where the final state of the system is deliberately chosen to be as different as possible to the initial state. As a result, the post-selection introduces an interference effect that produces an enhancement of the lateral displacement even with a weak interaction. A clear and useful explanation of how and

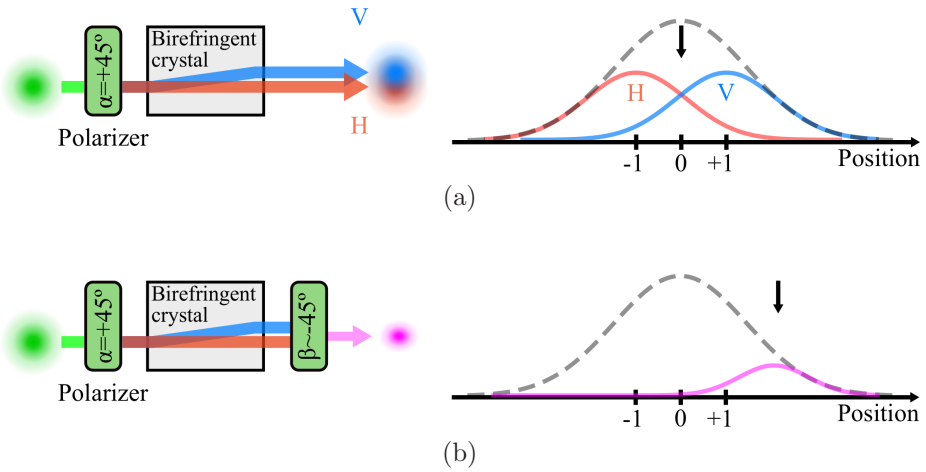


Figure 2.3: (a) Weak measurement. The meter's centroid position is indicated by an arrow. (b) Weak Value Amplification scheme. The pre- and post-selection polarizers are set to $\alpha = +45°$ and $\beta \approx -45°$, respectively. Notice that due to the use of the WVA effect, the meter's centroid position lies outside the interval $[-1, +1]$. In both plots the dotted line corresponds to the input beam spatial profile and the vertical arrow indicates the meter's reading.

why WVA works can be found in [4].

The new scheme, named *weak value amplification* (WVA), receives its name from the fact that the meter's centroid position is shifted by a quantity defined as the *weak value* of the observable to be measured that can be so large that it may lie outside the range of the possible outcomes of the measurement in the strong measurement scenario. Fig. 2.3 depicts two weak measurements. In Fig. 2.3(a) the output state of the system is not post-selected, while in Fig. 2.3(b) the output state is post-selected using a polarizer. Retaking the polarization measurement example used above, this means that after performing a suitable polarization post-selection, the output beam centroid may lie outside the interval $[-1, +1]$ as shown in Fig. 2.3(b). This surprising effect occurs when the post-selection state is set to be as different as possible to the initial state of the system. However, the price to pay for this *enhancement effect* is a reduction in the signal intensity at the output since both states are chosen to be almost orthogonal.

Mathematically, the weak value of an observable $\hat{A}$ is defined by

$$A_w = \frac{\langle \Psi_f | \hat{A} | \Psi_i \rangle}{\langle \Psi_f | \Psi_i \rangle}, \tag{2.1}$$

where $|\Psi_i\rangle$ and $|\Psi_f\rangle$ correspond to the pre-selected and post-selected states, respectively. Surprisingly, when the post-selection state is set to be almost orthogonal to the initial state of the system, that is when $\langle\Psi_f|\Psi_i\rangle \approx 0$, the weak value $A_w$ can be very large while the intensity of the output signal is severely depleted. In general, the weak value of $\hat{A}$ is a complex number. Depending on the selection of the initial and final states of the system, the weak value may become either real or imaginary. In fact, the nature of this value determines in which domain appears the weak value amplification effect. For a real value, the effect is observed in the same domain as the polarization dependent shift. Conversely, for an imaginary weak value, the amplification appears in the conjugate domain.

To illustrate in further detail this, consider a situation where we want to measure a temporal delay between two light pulses that is small compared to the pulse duration of each pulse. To determine the delay magnitude we can perform a measurement either in the time or the frequency domain. As it will be shown in Chapter 4, in order to generate an imaginary weak value the system is initially prepared in a state of left-handed circular polarization given by $|L\rangle = (|H\rangle - i\,|V\rangle)/\sqrt{2}$. After the weak measurement, the system is post-selected in a state of the form $(|H\rangle + \exp i\Gamma\,|V\rangle)/\sqrt{2}$, that can become close to orthogonal to the pre-selection state by choosing an appropriate value of the parameter $\Gamma$.

Another example is the use of a real weak value to determine the magnitude of a very small frequency shift between two overlapping spectra by measuring the weak value amplification effect that is observed as a shift in the central frequency of the output spectrum. This scenario is further discussed in Chapter 6, where we make use of a real weak value to enhance the sensitivity of temperature measurements performed by Fiber Bragg Gratings (FBG). The gratings, behave as frequency filters whose center is determined by its surrounding temperature. In this case, we aim to measure a polarization dependent frequency shift that is small compared to each FBG spectrum. Since the weak measurement and the detection are both performed in the frequency domain, we make use of a real weak value, generated using linear polarization states, that produces a weak value amplification effect that is observed in the same domain as the weak measurement.

Even from its origin, the concept of WVA has been very controversial [9, 10]. However, two years after Aharonov's et al. WVA paper, a first experimental demonstration of the measurement of a weak value was carried out by Ritchie and collaborators [5] that confirmed its validity. In their implementation, a birefringent crystal was used to perform the weak

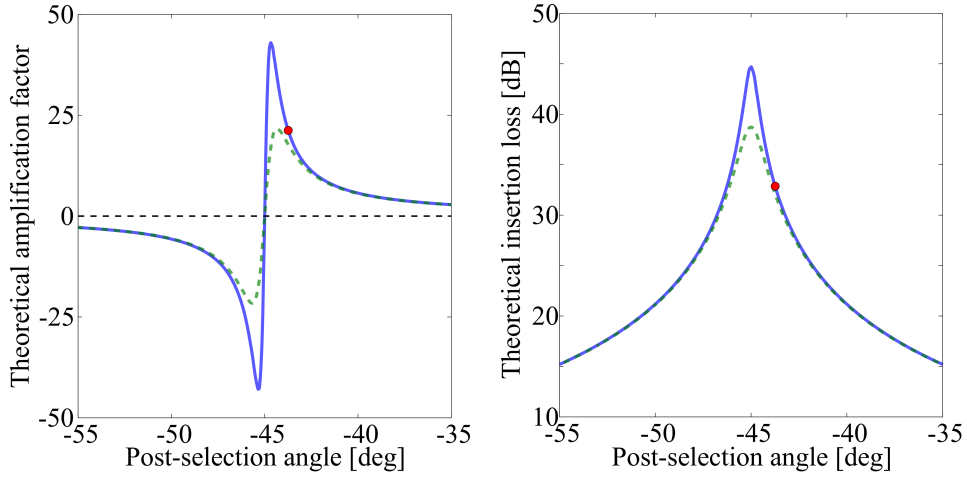


(a) (b)

Figure 2.4: (a) Amplification factor as a function of the post-selection angle $\beta$. (b) Insertion loss as a function of the post-selection angle $\beta$. $\phi = 0°$: blue solid line; $\phi = 1.15°$ green dashed line. The dot in both plots indicate the amplification factor $\mathcal{A} \approx 21$ and the insertion $L \approx 32\,\mathrm{dB}$ reported by Ritchie and collaborators.

measurement shown in Fig. 2.3(a) and two polarizers were located before and after the weak measurement to pre-select and post-select the input and output states of polarization.

In the experiment, schematically represented in Fig. 2.3(b), a X-cut $331\,\mu$m thick crystalline quartz plate was used to generate the polarization dependent beam displacement. The crystal was configured to generate a beam displacement of $\Delta = 0.64\,\mu$m while the input beam waist was set to $\sigma = 55\,\mu$m in order to fulfill the weak measurement condition $\sigma \gg \Delta$.

To generate the desired weak value amplification effect, the pre-selection and post-selection polarizers were set to be nearly orthogonal so that the first polarizer was set to $\alpha = \pi/4$ and the second polarizer to $\beta = \alpha + \pi/2 + \epsilon$, where $\epsilon = 2.2 \times 10^{-2}$ corresponds to a difference of only 1.26°. For this particular selection of pre- and post-selection polarization states, the weak value turns out to be real. Taking into account that the weak measurement couples polarization and position, the meter shift is observed in the position domain. From the experimental results is obtained that the output beam centroid is shifted by $A_w = 11.9\,\mu$m, a displacement approximately 20 times larger than the initial displacement $\Delta$ at the expense of a significant reduction in the output beam intensity of three orders of magnitude.

Since the weak value amplification process is always accompanied by losses of the detected signal, there is a trade-off between the amplification factor and the amount of losses that can be tolerated to keep a good signal-to-noise ratio. Fig. 2.4(a) shows the theoretical amplification factor, defined as the ratio between the meter's centroid shift and the polarization dependent displacement $\Delta$, and Fig. 2.4(b) the corresponding insertion loss $L$, according to Ritchie's experimental values, as a function of the post-selection angle $\beta$ for a pre-selection angle $\alpha = \pi/4$. The insertion loss defined as $-10\log[P_{\text{out}}/P_{\text{in}}]$, where $P_{\text{in}}$ ($P_{\text{out}}$) corresponds to the input beam (output) power.

It is important to notice that the amplification factor strongly depends on the relative phase ($\phi$) that may appear between the two components orthogonally polarized and on the strength of the weak interaction proportional to the ratio $\Delta/\sigma$. As a reference, the solid and dotted lines in Fig. 2.4 illustrate the cases $\phi = 0°$ (solid line) and $\phi = 1.15°$ (dashed line), respectively. From the plot is clear the need to match the phase between the two different polarizations; in Rithchie's experiment this phase is set to $\phi = 5 \times 2\pi$ by rotating the crystal 30° along its optical axis. Notice that Fig. 2.4(a) predicts a maximum amplification factor of $\approx 45$ that could not be reached in the experiment due to technical limitations. However, the enhancement given by the weak value amplification scheme made the initial displacement $\Delta = 0.64\,\mu$m measurable despite the limited resolution on the detection stage given by the separation between detector steps of $1.4\,\mu$m.

## Measurements in the high-signal regime

While the WVA scheme has proven to be successful in the low-signal regime, where the retrieval of information comes with a severe loss penalty, there are still situations where is not possible to enhance the signal to-noise ratio of the measurement for example by increasing the intensity of the input signal. Moreover, since the measured value of the weak value is the result of an interference phenomenon, the weak interference might be noticeable even in a regime of small losses, where the specific value of weak mean value might not convey any relevant information about the system or the measuring device.

Hence, it is possible to obtain relevant information about the weak interaction in a high-signal regime where the signal is not depleted, and the specific result of the weak value does not convey any relevant information. In this scenario the information about the weak interaction is not present

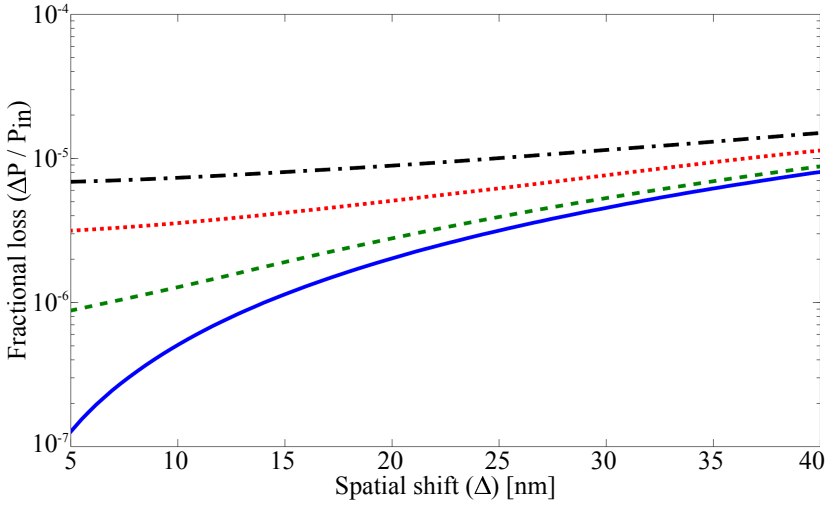


Figure 2.5: Fractional loss $\Delta P/P_{\text{in}}$ as a function of the spatial shift $\Delta$. $\alpha = \beta = 45°$ and $\sigma = 10\,\mu$m. Blue solid line: $\phi = 0°$; Green dashed line: $\phi = 0.1°$; Red dotted line: $\phi = 0.2°$; Black dot-dashed line: $\phi = 0.3°$.

in the meter's centroid position but in its intensity. In order to retrieve the information about the value of $\Delta$ we can measure the fractional loss defined as $\Delta P/P_{\text{in}}$, where $\Delta P = P_{\text{out}} - P_{\text{in}}$ [11].

As an example, Fig. 2.5 shows the value of the fractional loss, $\Delta P/P_{\text{in}}$, as a function of the spatial shift $\Delta$ for $\alpha = \beta = 45°$ and $\phi = 0°$, $0.1°$, $0.2°$, $0.3°$. In all cases, since the pre-selection and post-selection states are chosen to be equal, the total losses of the system are below 3 dB, which is significantly less than the loss found in the usual regime of weak amplification, where losses can easily reach tens of dB for large values of the weak value amplification. Moreover, in all cases shown in Fig. 2.5, the meter's centroid lie in the 0 mark and the usual WVA scheme does not provide any relevant information.

The maximum sensitivity of the scheme proposed is obtained for parallel pre-selection and post-selection states and $\phi = 0°$. By choosing other values for these angles, one can decrease the fractional loss, making its detection easier. However, this would decrease the sensitivity, making the distinction between different spatial shifts $\Delta$ more difficult. Note that here we are assuming that there are not other sources of polarization-dependent losses.

## 2.3 Applications

After Ritchie's demonstration, it was soon suggested that the concept of WVA may find application in metrology. In fact, the experiment not only validated the concept but it also demonstrated that a large weak value can be used to enable the sensitive estimation of extremely small quantities characterized by small polarization dependent shifts. Afterwards, these ideas were extended to measure other physical quantities by making a suitable selection of the physical nature of the meter and the system, and its coupling. Table 2.1 provides a brief summary of different physical quantities where tiny changes have been measured by making use of a WVA scheme. The table shows the physical observable measured and its magnitude.

Even though the concept of weak measurements originates from research on quantum theory, the phenomenon of weak value amplification can be readily understood in terms of constructive and destructive interference between probability amplitudes in a quantum mechanics context [4], or in terms of interference of classical waves [11, 19]. Indeed, most of the experimental implementations of the concept belong to the last type. The usefulness of weak value amplification for measuring extremely small quantities has been demonstrated under a great variety of experimental conditions to measure very small transverse displacements of optical beams [5, 3], beam deflection [12, 13, 14, 19, 20, 21, 22, 23, 24, 25, 26], angular shifts [27], temporal shifts [28, 29, 30], phase shifts [15, 31, 32], frequency shifts [16], velocity measurements [17] and temperature differences [18, 33].

## What is next?

Weak Value Amplification (WVA) is a concept that has been used under a great variety of experimental conditions to measure tiny changes of a variable of interest. We have presented in this Chapter what it is and have shown a list of experiments that use the concept. In the following chapters we will present the result of various experiments performed during this PhD Thesis aimed at applying the concept of WVA discussed here. The goal is to offer new ways that can improve current technologies when measuring tiny changes of physical quantities of interest. We will apply this concept to measuring small time delays, we will build a new type of beam displacer with no moving parts, and enhance the sensitivity of temperature sensors based on Fiber Bragg Gratings.

In addition to all these particular experiments carried out during the

| Observable | Results |
|---|---|
| Beam displacement | Measure the Spin Hall Effect of Light (SHEL) in an air-glass interface. An enhancement of the original displacement by four orders of magnitude, corresponding to a sensitivity of $\approx 1$Å is reported [3]. |
| Beam displacement | Report a method for determining the the number of graphene layers on a sample by measuring beam displacements due to SHEL.[12]. |
| Mirror angular deflection | By using a WVA scheme in conjunction with a lock-in amplifier an angular deflection of a mirror of $400 \pm 200$ frad was measured. The angular deflection is generated using a piezo actuator with a linear travel of $14 \pm 7$ fm [13]. |
| Optical activity | Reported the measurement of circular birefringence of $\Delta n \approx 1 \times 10^{-9}$ with a relative error of less than 1% by measuring beam deflections of $\Delta\theta \approx 1 \times 10^{-9}$ rad [14]. |
| Phase shifts | Reported measurements of phase shifts of the order of $\approx 10^{-3}$ with a precision of $\approx 10^{-4}$. The experimental results compares favorably with respect to other techniques that make use of N00N and squeezed states of light [15]. |
| Frequency shifts | Using an optical deflection experiment based on a Sagnac interferometer they were able to measure a change in optical frequency of $129 \pm 7\,\mathrm{kHz}/\sqrt{\mathrm{Hz}}$ [16]. |
| Speed | By using non-Fourier limited pulses and a WVA scheme, velocity as small as 400 fm/s where reported by measuring the induced time shift of the non-Fourier limited pulses [17]. |
| Temperature | Temperature measurements with 0.2 mK sensitivity over a range of 20 mK by sensing nanoradian deviations of a laser beam [18]. |

Table 2.1: Examples of experiments that make use of the concept of WVA scheme to measure extremely small changes of variables of interest.

PhD Thesis, we are also interested in analyzing and evaluating the true usefulness of WVA. Therefore we will join the on-going debate about its nature in order to determine its true usefulness for achieving high sensitivity measurements with respect to other experimental techniques.

More specifically, Chapter 2 presents the connection of WVA to the observation of spectral interference in a Michelson interferometer, regardless of the relationship between the temporal path difference introduced between the arms of the interferometer and the spectral width of the light source.

Chapter 3 shows the results of an experimental scheme to measure small temporal delays between pulses much smaller than the pulse width. Chapter 4 presents an experimental scheme that allows to generate a highly-sensitive tunable beam displacer that can outperform the limitations imposed by the use of movable optical elements. Chapter 5 presents an experiment aimed at increasing the sensitivity of Fiber Bragg Grating (FBG) sensors. Chapter 6 addresses the question of whether or not the use of the WVA improves the sensitivity of certain detection schemes. By making use of some basic concepts from quantum estimation theory, it is shown that WVA might be useful for detection schemes that are limited by technical noise.

## Main publication by the author related to the contents of this

J. P. Torres, G. Puentes, N. Hermosa, and **L. J. Salazar-Serrano**, "Weak interference in the high-signal regime", Optics Express **20**, 18869 (2012).

CHAPTER

# THREE

# OBSERVING SPECTRAL INTERFERENCE IN A MICHELSON INTERFEROMETER FOR ALL DELAYS

> *The important thing is not to stop questioning. Curiosity has its own reason for existing. One cannot help but be in awe when he contemplates the mysteries of eternity, of life, of the marvelous structure of reality.*
>
> Albert Einstein, *1955*

Interference is a fundamental concept in any theory based on waves, such as classical electromagnetism or quantum theory. The specific experimental arrangement required for the observation of interference depends on the characteristics of the light source, i.e., its spatio-temporal profile and its degree of coherence. For example, for first-order coherent light in a Michelson interferometer and temporal delays shorter than the pulse width, interference manifests as a delay-dependent change of the intensity at the output port of the interferometer. For longer temporal delays, interference manifest as spectral interference for a given temporal delay. The observation of spectral interference was denoted by Mandel [34, 35] as the Alford-Gold effect [36] and it is well-known in optics [37].

In this chapter we demonstrate experimentally that it is possible to observe spectral interference in a Michelson interferometer, regardless of the relationship between the temporal path difference introduced between the

arms of the interferometer and the spectral width of the input pulse. The interference is revealed as a reshaping of the input spectrum that is accomplished by introducing the polarization degree of freedom into a Michelson interferometer. This scenario corresponds precisely to the conditions of a typical weak value amplification configuration [2, 4, 38, 39] that although was originally conceived in the framework of a quantum formalism, it is essentially based on the phenomena of interference and can thus be applied to any scenario with waves [15, 19, 28, 30, 32].

This chapter is organized as follows. Section 3.1 provides the theoretical background that allows to study the phenomena of interference in a Michelson-Morley interferometer for different regimes of operation where the optical path difference is made shorter or longer than the duration of an input pulse. Section 3.2 describes the experimental setup implemented. In Section 3.3 the results obtained are presented and discussed.

## 3.1 Theoretical description

For the sake of clarity, let us start by describing temporal and spectral interference in a typical Michelson interferometer, without considering polarization. Later on, we will describe the effects that the introduction of the polarization degree of freedom has on the observation of spectral interference.

Consider the situation depicted in Fig. 3.1(a). A first-order coherent input pulse with amplitude $E_0$, central frequency $\nu_0$, input polarization $\hat{\mathbf{e}}_{\text{in}}$, and temporal duration $\tau$ (full width at half maximum) described by

$$\mathbf{E}_{\text{in}}(t) = E_0 \, \exp\left[-2\ln 2\, t^2/\tau^2 + i\, 2\pi\nu_0 t\right] \, \hat{\mathbf{e}}_{\text{in}} \,, \tag{3.1}$$

enters a Michelson interferometer where is divided in two beams by a beam splitter (BS). Each of the new pulses follows a different path and after reflection in a mirror the two pulses recombine at the BS. By changing the position of one of the mirrors, a temporal delay $T$ is generated between the two pulses. The intensity measured by a slow detector at the output port of the interferometer as a function of $T$ can be written as

$$I(T) = \frac{I_0}{2} \, \left[1 + \exp\left(-\ln 2\, T^2/\tau^2\right) \, \cos\left(2\pi\nu_0 T\right)\right] \,, \tag{3.2}$$

where $I_0 = |E_0|^2$. Two interesting cases can be distinguished from Eq. (3.2): i) when $T \ll \tau$, so that the two pulses traveling the different paths overlap

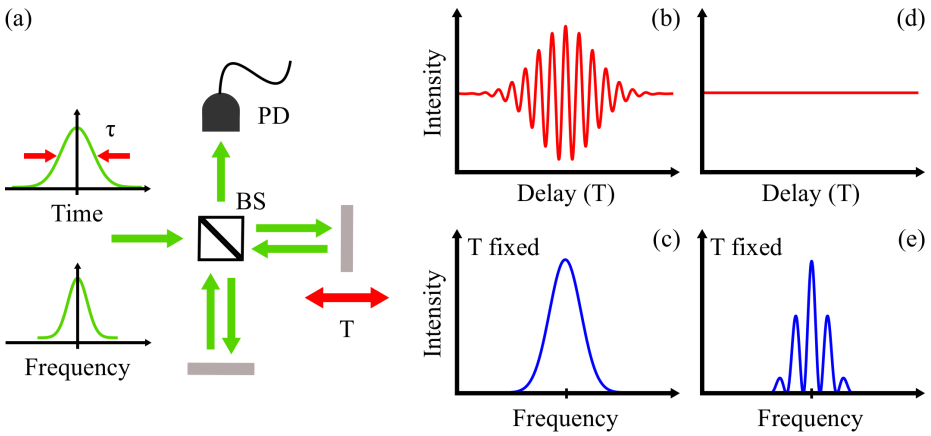


Figure 3.1: Typical interference patterns that can be observed in a Michelson interferometer, in the time and frequency domains. In (a) we depict the interferometric configuration considered. (b) and (d) show the intensity measured as a function of a temporal delay $T$. (c) and (e) show the intensity as a function of frequency for a given value of $T$. (b) and (c) correspond to the case $T \ll \tau$, while (d) and (e) correspond to the case, $T \gg \tau$. BS: beam splitter, PD: Photodetector.

in time, and ii) when $T \gg \tau$, the two pulses do not overlap. In the first case, the output intensity as a function of $T$ reduces to

$$I_{T\ll\tau}(T) = \frac{I_0}{2}\left[1 + \cos(2\pi\nu_0 T)\right], \tag{3.3}$$

while in the case $T \gg \tau$, Eq. (3.2) becomes

$$I_{T\gg\tau}(T) = \frac{I_0}{2}. \tag{3.4}$$

These results are very well known in optics. They indicate the observation of interference in the temporal domain for the case $T \ll \tau$ and its absence for $T \gg \tau$. The two situations are illustrated in Fig. 3.1(b) and Fig. 3.1(d).

An analogous analysis can be done when the detector in Fig. 3.1(a) is changed by a spectrometer and the power spectrum $S(\nu)$ is considered as a function of the frequency $\nu$. In this case,

$$S(\nu) = \frac{S_{\text{in}}(\nu)}{2}\left[1 + \cos\left(2\pi\nu\, T\right)\right], \tag{3.5}$$

where

$$S_{\text{in}}(\nu) = S_0 \exp\left[-(\pi^2\tau^2/\ln 2)(\nu - \nu_0)^2\right], \tag{3.6}$$

is the input power spectrum with $S_0$ being a constant.

Equation (3.5) indicates that $S(\nu)$ corresponds to a reshaping of the input spectrum. This reshaping can be understood if $h(\nu) = \frac{1}{2}[1+\cos(2\pi\nu T)]$ is considered as a transfer function that describes the effect of the interferometer. The observation of spectral interference depends on the relationship between the oscillation frequency of the transfer function, given by $1/T$, and the pulse bandwidth, given by $1/\tau$. Figures 3.1(c) and 3.1(e) depict the output power spectrum for the regimes $T \ll \tau$ and $T \gg \tau$, respectively. The two cases are clearly different. As expected from standard interferometry, when $T \ll \tau$, the output power spectrum is almost identical to the input one, while for $T \gg \tau$, a clear reshaping of the input spectrum appears. This last case corresponds to the Alford-Gold effect and indicates that a Michelson interferometer can be seen as a periodic filter that produces a modulation of the initial spectrum with a peak separation proportional to $\sim 1/T$.

Now let us describe the possible observation of interference effects when adding the polarization degree of freedom to the Michelson interferometer. For this, consider the Michelson interferometer depicted in Fig. 3.2 in which four main differences with the standard Michelson interferometer of Fig. 3.1(a) can be observed:

1. the presence of polarization control elements in the input port of the interferometer

2. the substitution of the beam splitter (BS) by a polarizing beam splitter (PBS)

3. the introduction of a quarter wave plate (QWP) in each arm of the interferometer

4. the presence, in the output port, of a variable polarization analyzer, composed by a liquid crystal variable retarder (LCVR) and a polarizer at 45°

The polarizer, half-wave plate and quarter wave plate in the interferometer's input port are used to set up the polarization of the input beam. The PBS divides spatially the two orthogonal polarization components of the input beam and the QWP rotates the corresponding polarization component by 90° after reflection in each mirror. The movable mirror generates the temporal delay $T$.

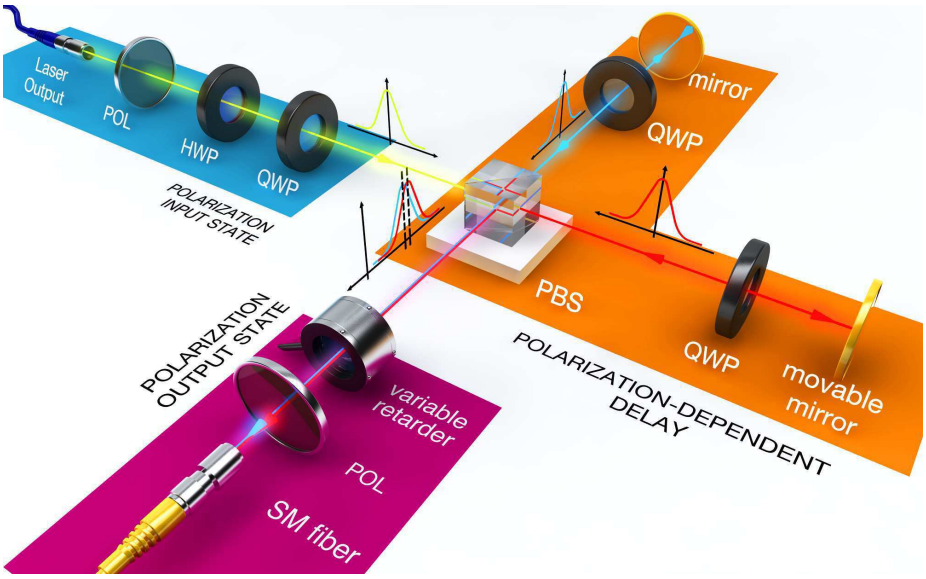


Figure 3.2: Experimental scheme. The input pulse polarization state is selected to be left-circular by using a polarizer, a quarter wave plate (QWP) and a half wave plate (HWP). A Polarizing beam splitter (PBS) splits the input into two orthogonal linear polarizations that propagate along different arms of the interferometer. An additional QWP is introduced in each arm to rotate the beam polarization by 90° to allow the recombination of both beams in a single beam by the same PBS. The output beam spectrum is measured by an optical spectrum analyzer (OSA) connected to a single mode fiber (SM).

Two beams with orthogonal polarizations do not interfere. However, in the scheme described here an interference effect can be generated by the polarization control elements at the output port that generate an additional phase difference, $\Gamma$, between the pulses coming from the two paths of the interferometer. In particular, for a left-handed circularly polarized input beam ($\hat{\mathbf{e}}_{\text{in}} = \hat{\mathbf{x}} - i\hat{\mathbf{y}}$), where $\hat{\mathbf{x}}$ denotes horizontal polarization and $\hat{\mathbf{y}}$ vertical polarization, the output electric field reads

$$\begin{aligned}\mathbf{E}_{\text{out}}(\nu) = E_0 \sqrt{\frac{\pi\tau^2}{4\ln 2}} \exp\left\{-[\pi^2\tau^2/(2\ln 2)]\,(\nu-\nu_0)^2\right\} \\ \times \left\{\exp\left(-i\,2\pi\nu T\right)\hat{\mathbf{x}} + \exp\left[-i\,(\Gamma+\pi/2)\right]\hat{\mathbf{y}}\right\}\,. \qquad (3.7)\end{aligned}$$

The power spectrum of the light at the interferometer's output port is then

given by

$$S_{\text{out}}(\nu) = \frac{S_{\text{in}}(\nu)}{2}\left[1 + \cos\left(2\pi\nu\, T - \Gamma - \pi/2\right)\right] . \tag{3.8}$$

In the same way as in Eq. (3.5), we can identify Eq. (3.8) as a transfer function, $H(\nu) = \frac{1}{2}[1 + \cos(2\pi\nu\, T - \Gamma - \pi/2)]$, and distinguish again two cases depending on the relationship between the frequency of oscillation of $H(\nu)$ and the width of the input power spectrum.

## 3.2 Experimental implementation

Figure 3.3 presents the experimental setup used to check that spectral interference can be observed independently of the value of $T$. The figure shows the components used and highlights the different stages used to select the input's beam initial state of polarization, to perform a polarization-dependent delay and to select the output's beam state of polarization. Notice that the setup is based only on linear optical elements.

In the first stage, highlighted in cyan in Fig. 3.3(d), the output of a passively mode-locked fiber laser (Calmar Laser - Mendocino), that generates pulses with a temporal duration $\tau = 320\,\text{fs}$, repetition rate of 20 MHz and central frequency $\nu_0 = 193.5\,\text{THz}$ (1550 nm), is collimated to a beam with a Gaussian profile of diameter 1.1 mm $(1/e^2)$ using a fixed focus collimation package. Its state of polarization is prepared to be left-handed circular polarization, i.e., $\hat{\mathbf{e}}_{\text{in}} = (\hat{\mathbf{x}} - i\,\hat{\mathbf{y}})/\sqrt{2}$, by using the combination of polarizer $\text{POL}_1$, half-wave plate $\text{HWP}_1$ and quarter-wave plate $\text{QWP}_1$ (Fig. 3.3(c)).

Afterwards, in the stage highlighted in orange in Fig. 3.3(d), a polarization-dependent delay is implemented. A polarizing beam splitter $\text{PBS}_1$ splits the input beam into two beams with orthogonal linear polarizations that propagate along different arms of the interferometer. Two quarter-wave plates, $\text{QWP}_2$ and $\text{QWP}_3$, are introduced in each arm of the interferometer to rotate the beam polarization by 90° and allow the recombination of both beams in a single beam by the same PBS after reflection in mirrors $\text{M}_2$ and $\text{M}_3$, respectively. Mirror $\text{M}_3$ is mounted on a translation stage (TSTG) that allows to change its position, and thus the difference in path between the two arms of the interferometer, namely the distance between $\text{PBS}_1$ and mirror $\text{M}_2$ and $\text{PBS}_1$ and mirror $\text{M}_3$. Notice that the output beam is composed of two pulses with orthogonal polarizations that are delayed in time by $T$. We used an OWIS DIGI-MIC translation stage that provides a 25 mm travel with a minimal step of 1 $\mu$m. With this characteristics, a minimum delay of 6.6 fs and a maximum delay of 166 ps can be generated.

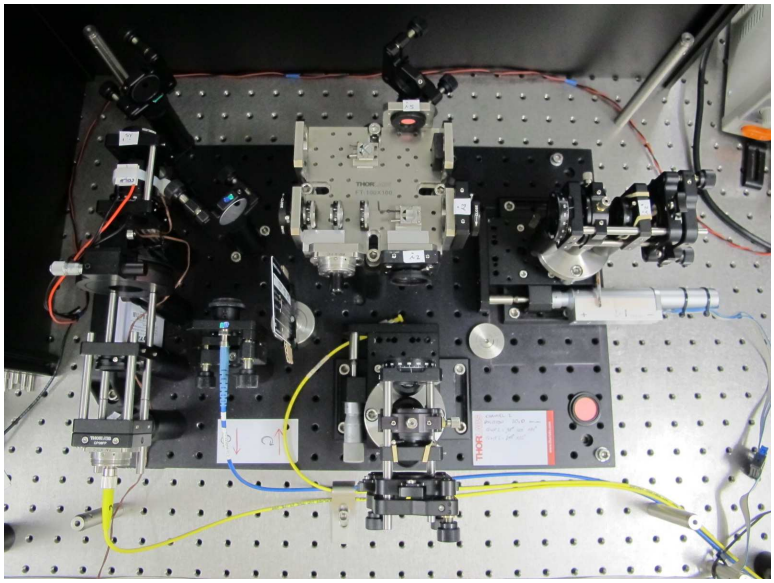

(a)

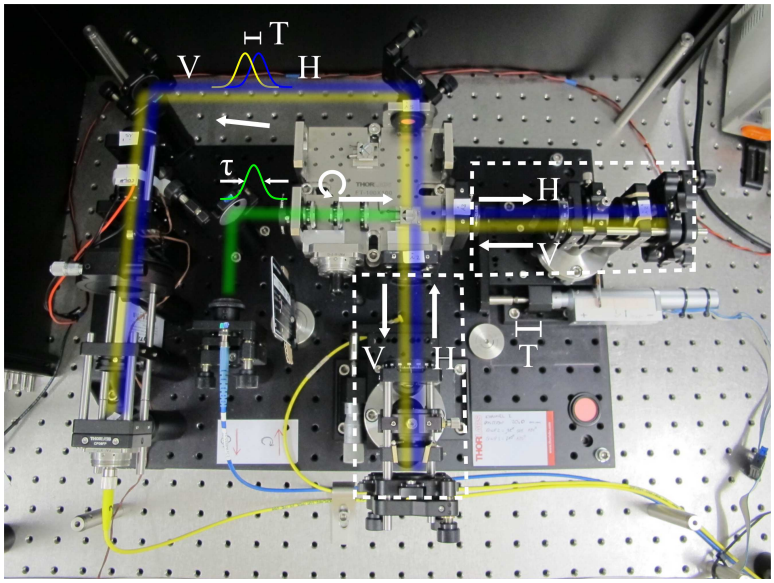


(b)

Figure 3.3: (a) Experimental setup (top view). (b) Optical beam layout. The input pulse of duration $\tau$ (FWHM) and the output beam, composed of two pulses delayed by $T$ with orthogonal polarizations are indicated. The delay between pulses is introduced by moving a mirror in one of the arms of the interferometer (indicated by the dashed regions) using a translation stage. In the experiment, the delay $T$ is scanned over the interval $[-12\tau, +12\tau]$.

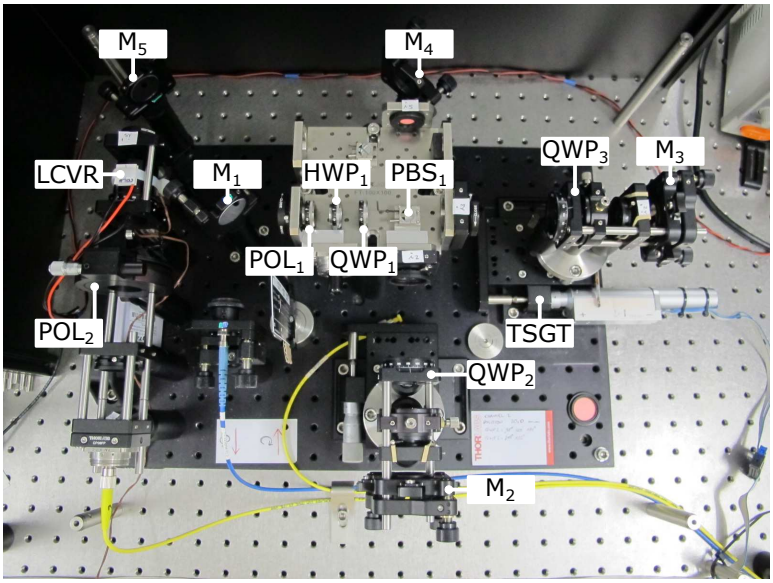


(c)

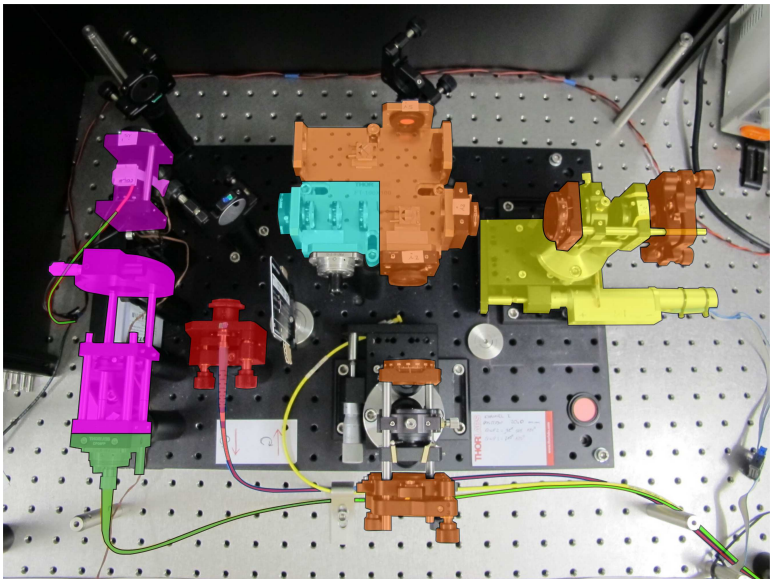

(d)

Figure 3.3: (c) Detail of the components used. M: Mirror, HWP: Half-Wave Plate, QWP: Quarter-Wave Plate, PBS: Polarizing Beam Splitter, POL: Polarizer, TSTG: Translation Stage, LCVR: Liquid Crystal Variable Retarder. (d) Stages used to: i) select the initial state of polarization (cyan), ii) perform a polarization-dependent delay (orange), iii) select the final state of polarization (magenta). The input port, translation stage and output port, are colored in red, yellow and green respectively.

In the last stage, highlighted in magenta in Fig. 3.3(d), the state of polarization of the output beam is selected. Once the output beam is reflected in mirrors $M_4$ and $M_5$, its state of polarization is selected using the liquid crystal variable retarder LCVR (Thorlabs LCC1223-C) followed by polarizer $POL_2$ that is rotated at $+45°$. The LCVR is thermally stabilized using a Peltier cell connected to a temperature controller. After polarizer $POL_2$, the output beam is focused into a single mode fiber (SM) and its spectrum is measured with an optical spectrum analyzer (OSA) (Yokogawa - AQ6370).

## 3.3 Experimental results

We present in the first column of Figs. 3.4 and 3.5 various transfer functions (dotted lines) generated by using different values of $\Gamma$ and $T$ in Eq. (3.8), and the measured power spectrum of the pulsed laser (solid line). We observe that for the case $T \gg \tau$ (Fig. 3.4) various oscillations of the transfer function fit inside the initial spectrum bandwidth. For $T \ll \tau$ (Fig. 3.5) this is not the case, and $H(\nu)$ is now a very broad cosine function.

Notwithstanding, in both regimes the delay $\Gamma$ modifies the transfer function. In the regime $T \gg \tau$ the effect of $\Gamma$ is to reshape the input spectrum so that a periodic intensity pattern appears, while in the regime $T \ll \tau$, the effect is to shift the positions of the peaks of the output spectrum.

It is important to notice that for all regimes the reshaping of the spectrum is the result of an interference effect and therefore indicates that spectral interference can be observed in a Michelson interferometer, independently of the temporal path difference under consideration, when the polarization degree of freedom is considered in the interferometer.

The second column of Figs. 3.4 and 3.5 shows the experimental results for $T \gg \tau$ and $T \ll \tau$, respectively. A reshaping of the spectrum is clearly observed in both cases. For the case of $T \gg \tau$, a clear modulation of the spectrum with spacing between peaks equal to $1/T$ is observed, which corresponds to the Alford-Gold effect. For the regime $T \ll \tau$, $H(\nu)$ is a broad cosine function. In this regime two situations can be distinguished, both accompanied by different amount of losses. In one case the reshaping corresponds to a modulation of the initial spectrum Fig. 3.5(f), while in the other the transfer function can present a positive slope, as in Fig. 3.5(c) or negative, as in Fig. 3.5(g). When $H(\nu)$ multiplies the input spectrum, the result is a non-symmetric output spectrum, as observed in Figs. 3.5(d) and 3.5(h) respectively.

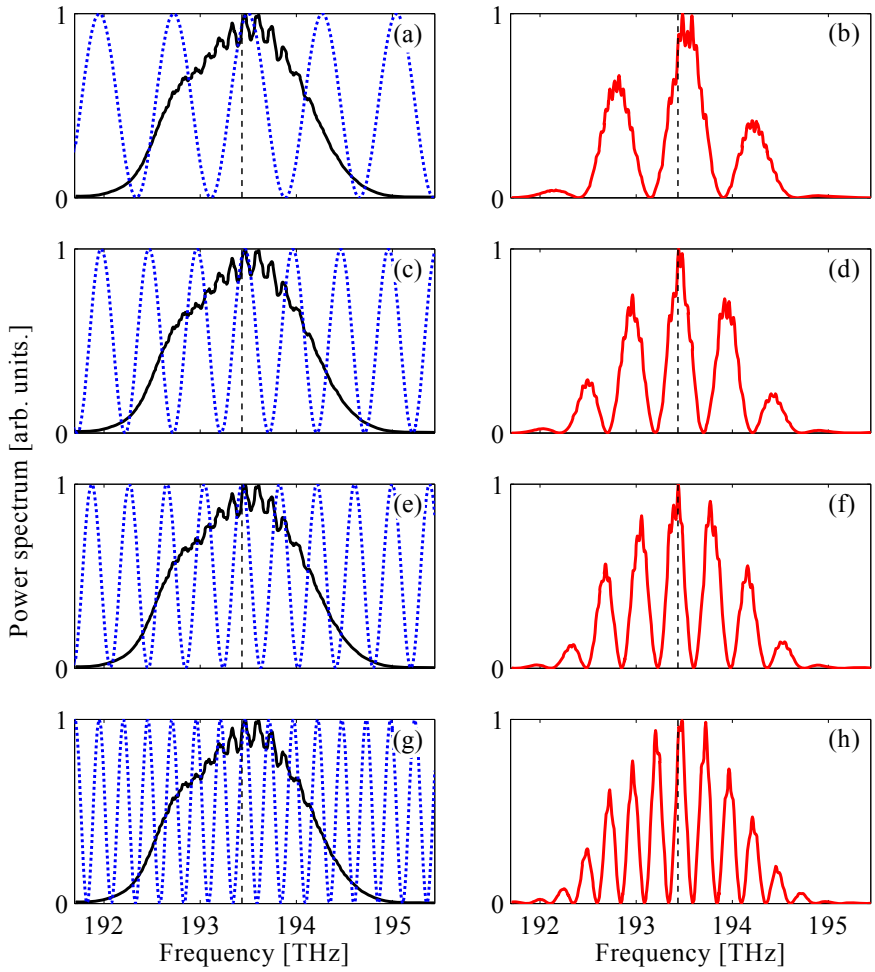


Figure 3.4: Spectral interference in the regime $T \gg \tau$. First column depicts the experimental input spectrum, $S_{\text{in}}(\nu)$, of a pulsed laser with a temporal duration $\tau = 320\,\text{fs}$ centered in $\nu_0 = 193.5\,\text{THz}$ (solid line) and the theoretical transfer function, $H(\nu)$, (dotted line) for $\Gamma = 26.55°$ and different time delays: $T = 1453\,\text{fs}$ in (a), $T = 2120\,\text{fs}$ in (c), $T = 2786\,\text{fs}$ in (e) and $T = 4120\,\text{fs}$ in (g). Second column shows the experimental output spectrum that can be obtained by evaluating $S_{\text{out}}(\nu) = H(\nu)\, S_{\text{in}}(\nu)$. As a reference, the vertical dashed line indicates the central frequency, $\nu_0$, of the input spectrum.

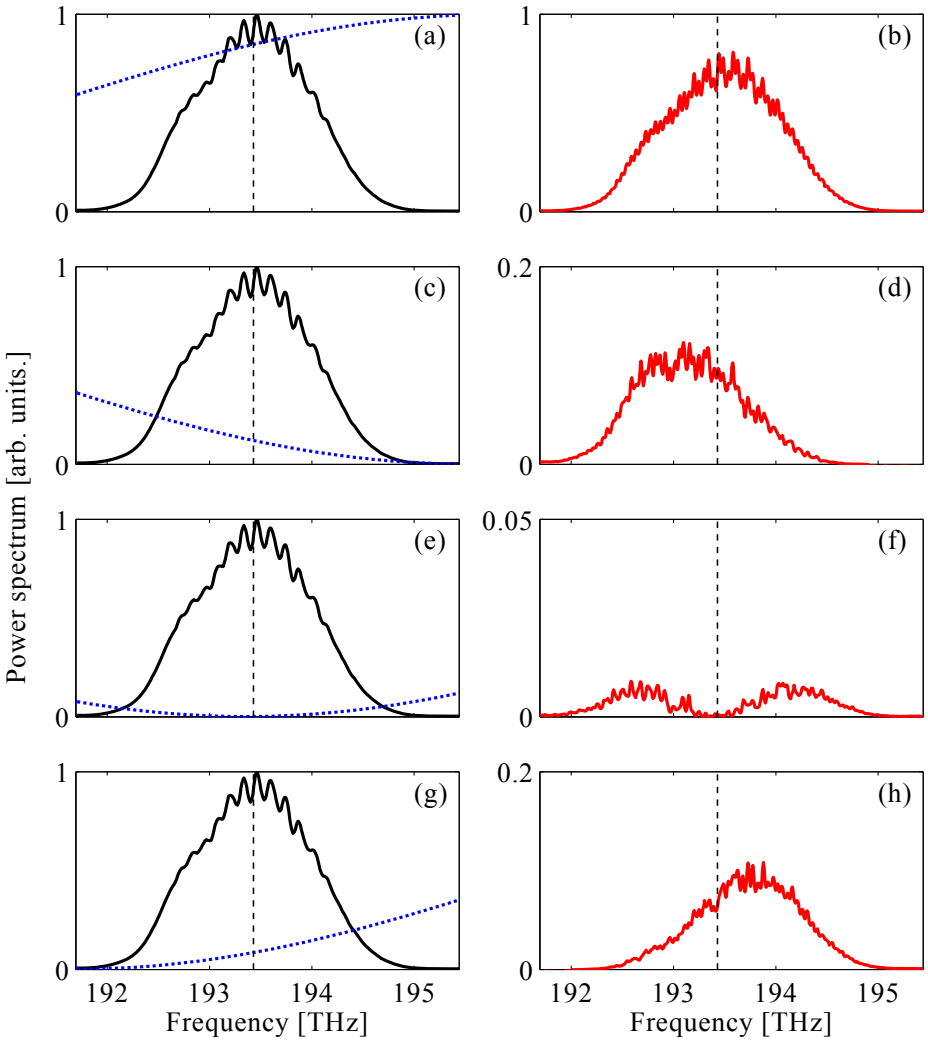


Figure 3.5: Spectral interference in the regime $T \ll \tau$. First column depicts the experimental input spectrum, $S_{\text{in}}(\nu)$ , of a pulsed laser with a temporal duration $\tau = 320\,\text{fs}$ centered in $\nu_0 = 193.5\,\text{THz}$ (solid line) and the theoretical transfer function, $H(\nu)$, (dotted line) for a fixed delay of $T = 53.7\,\text{fs}$ and $\Gamma = 98.5°$ in (a), $\Gamma = 273.1°$ in (c), $\Gamma = 231.2°$ in (e), and $\Gamma = 198.9°$ in (g). Second column shows the experimental output spectrum that can be obtained by evaluating $S_{\text{out}}(\nu) = H(\nu)\, S_{\text{in}}(\nu)$. The vertical dashed line indicates the central frequency of the input spectrum. Notice that the vertical axis in the right column has been rescaled since the output intensity changes dramatically with different values of $\Gamma$.

In general, the reshaping of the spectrum translates into a measurable shift of the mean frequency of the output power spectrum when compared with the central frequency of the input pulse (Figs. 3.5(d) and 3.5(h)). Furthermore, although this behavior is well explained in terms of classical optics, it can also be presented under the formalism of a weak value amplification scheme, where the frequency serves as the meter and the polarization as the system [15, 17, 28, 30, 32]. This result shows that spectral interference can also be observed in the regime of small optical path differences ($T \ll \tau$) and complements the observation of the Alford-Gold effect, which reveals interference in the frequency domain in the opposite regime, $T \gg \tau$.

The observation of spectral interference, regardless the temporal path difference, was made possible by introducing the polarization variable in a Michelson interferometer in an experimental scheme similar to the ones used in a weak measurement scenario. In the case $T \gg \tau$, a clear modulation of the frequency spectrum with frequency $1/T$ (see Figs. 3.4(b), (d), (f) and (h)) appears, whereas in the regime $T \ll \tau$, interference manifests as either a modulation of the input spectrum (Fig. 3.5(f)) or as a shift of the central frequency (Figs. 3.5(b), (d) and (h)). Similar effects, as considered here, can be observed when short or long temporal delays in the Michelson interferometer are substituted by weakly or strongly misaligned beams in a Sagnac interferometer [40].

# Conclusions

In this chapter, we have shown the experimental observation of spectral interference in a Michelson interferometer, regardless of the relationship between the temporal path difference introduced between the arms of the interferometer and the spectral width of the input pulse. This observation is possible by introducing the polarization degree of freedom into a Michelson interferometer using a typical weak value amplification scenario.

The results obtained show that a concept originally born in the realm of quantum optics (weak value amplification) can be applied indeed to any system that shows interference, such as the case of classical optics. In a sense, the work presented here can thus be included in a broader research effort that shows that certain features of quantum systems can also be used to characterize beams containing many photons, i.e., intense beams that can be coherent or not. For example in [41, 42] the authors make use of a Bell's like inequality to characterize the coherence properties of a beam. Non-quantum entanglement, or inseparability between degrees of freedom

has also been considered [43, 44] as a fundamental tool to address and shed new light into certain characteristics of classical fields, by applying analysis and techniques usually restricted to entanglement in a quantum scenario.

## Main publication by the author related to the contents of this chapter

**L. J. Salazar-Serrano**, A. Valencia, and J. P. Torres, "Observation of spectral interference for any path difference in an interferometer", Optics Letters **39**, 4478 (2014).

CHAPTER

# FOUR

# MEASUREMENT OF EXTREMELY SMALL TEMPORAL DELAYS

> *When I am working on a problem I never think about beauty. I only think about how to solve the problem. But when I have finished, if the solution is not beautiful, I know it is wrong.*

Buckminster Fuller , *1983*

The measurement of the temporal delay that exists between two optical pulses is essential in many applications in metrology. For instance, it is the basis of some protocols aimed at accurate distance measurements and timing synchronization [45, 46], where the capability of discriminating between small temporal delays with a *reference* pulse is needed. Diverse optical schemes for measuring subpicosecond temporal delays have been demonstrated. This is the case, for instance, of systems based on the use of ultrafast nonlinear processes such as second harmonic generation [47, 48] or two-photon absorption [49].

In another context, the well-known Hong-Ou-Mandel effect makes use of quantum interference to measure subpicosecond temporal delays between photons [50], which was used by Steinberg et al. [51] for measuring very small single-photon tunneling times. Since this technique is based on measuring two-photon coincidences, it generally restrict the number of photons of the signal. However, quantum-inspired interferometers [52] might broaden the applicability of quantum concepts to other scenarios.

In this chapter, we demonstrate experimentally a scheme to measure extremely small temporal delays between pulses, delays much smaller than the width of the pulses, based on an interference effect generated with weak value amplification. A sub-pulse-width temporal delay between two femtosecond pulses induces a measurable shift of the central frequency of a certain combination of the two pulses. The amount of frequency shift, and the accompanying losses of the measurement, can be tailored by post-selecting different states of polarization. Our scheme requires only spectrum measurements and linear optics elements, hence greatly facilitating its implementation. Thus it appears as a promising technique for measuring small and rapidly varying temporal delays.

This chapter is organized as follows. Section 4.1 presents the scheme used to measure small delays based on weak value amplification and provides the main theoretical background. Section 4.2 presents the experimental setup implemented and in Section 4.3 we discuss the results obtained.

## 4.1 Optical scheme aim at measuring small temporal delays based on the concept of weak value amplification

When two similar optical pulses with temporal width $\tau$, and time delay $T \gg \tau$ between them, recombine, a modulation of the spectral density appears [34, 35, 36], which allows measuring the time difference $T$. This is true even if the optical path difference is larger than the coherence length of the pulses [37]. However, for small values of T ($T \ll \tau$), inspection of the spectral density reveals no interference effects, even though interference manifest now in the temporal domain as a periodic change of the output intensity as function of the delay.

Here we demonstrate experimentally a scheme to measure small temporal delays $T$ between optical pulses, delays much smaller than the pulse width $\tau$, based on an interference effect in the frequency domain which produces a measurable shift of the central frequency of a combination of the pulses [28]. The scheme makes use of linear optics elements only and works in both the high and low signal regimes. It allows the measurement of temporal delays between optical pulses up to the attosecond timescale [29]. This phenomenon, which is inspired by the concepts of quantum weak mea-

surement and weak value amplification [2, 4, 38, 53], produces interference effects in the regime $T \ll \tau$, which allows to unveil the value of $T$. Techniques for measuring small phase shifts using weak value amplification have also been proposed [28, 29, 32].

Brunner and Simon [28] showed that the introduction of a small temporal delay between the two components (horizontal and vertical) of a circularly-polarized pulse, can yield a large central frequency shift after recombining the pulses and projecting them into a polarization state nearly orthogonal to the input state. However, the near orthogonality of the input and output polarization states introduces heavy losses. Nevertheless, the weak value amplification can also be used when the input and output polarization states have a relatively large overlap, hence away from the usual weak value amplification regime [11], allowing for the observation of significant frequency shifts without heavy losses.

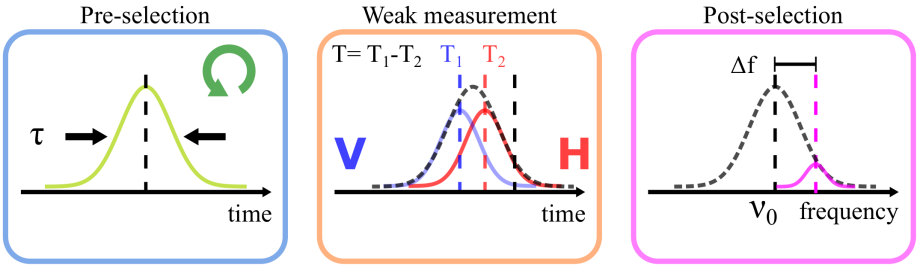


Figure 4.1: Weak value amplification scheme. In this case we make use of an imaginary weak value to retrieve information of the time difference $T = T_1 - T_2$.

The weak value amplification scheme proposed is composed of the three stages shown in Fig. 4.1. In the first stage (pre-selection), a light source that generates pulses of duration $\tau$, centered in $\nu_0$, is polarized with circular polarization by using a linear polarizer and a quarter-wave plate. In the second stage (weak measurement), a weak measurement is implemented by using a Michelson-Morley interferometer that performs a polarization -dependent delay that fulfills the weak measurement condition since $T \ll \tau$. In the third and last stage (post-selection), the output beam's polarization stage is again selected using a variable retarder followed by a polarizer. From the post-selection, the beams with horizontal and vertical polarizations interfere and a reshaping of the spectrum is observed. By measuring $\Delta f$, the difference between the centroid of the output spectrum and the input beam central frequency $\nu_0$, information about the temporal delay $T$

generated with the interferometer is retrieved.

### 4.1.1 Theoretical description

Consider the weak value amplification scheme shown in Fig. (4.1) composed of pre-selection, weak measurement and post-selection. A pulsed laser generate pulses with spectral density given by $S_{\text{in}}(\nu) = 2\,\epsilon_0 c|E_{\text{in}}(\nu)|^2$, where $E_{\text{in}}(\nu)$ is the electric field, $\nu$ designates the frequency, $\epsilon_0$ is the vacuum permittivity and $c$ is the velocity of light.

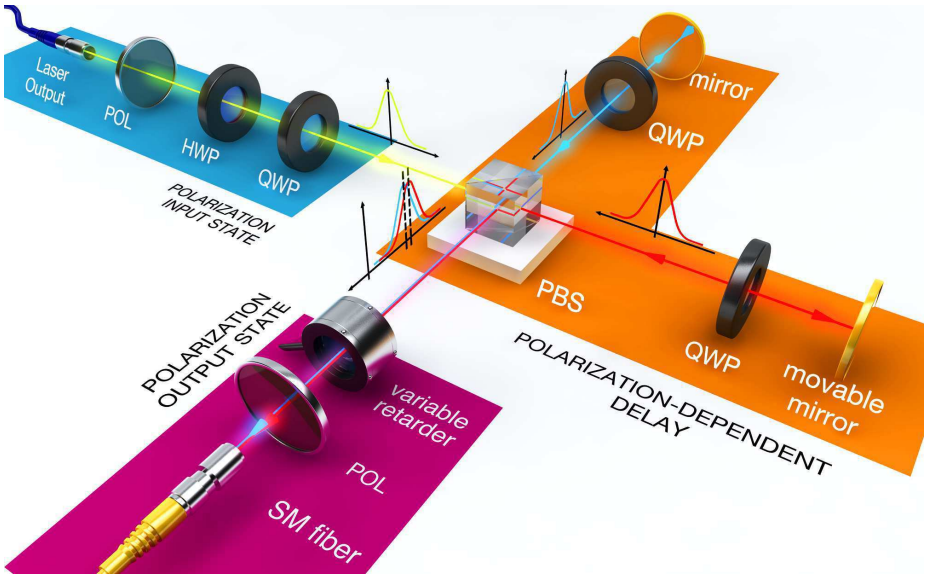


Figure 4.2: Experimental scheme. State pre-selection: The polarization of the input optical pulse is selected by using a polarizer, half-wave plate and quarter-wave plate. Weak coupling: A Michelson-Morley interferometer, composed of a Polarizing Beam Splitter (PBS), two quarter-wave and two mirrors, divides the input pulse into two pulses, with equal power and with orthogonal polarizations, that travel through different paths of the interferometer. A movable mirror mounted on a translation stage in one of the paths allows changing the temporal delay. State post-selection: The two pulses recombine in the PBS, and they are projected into a particular state of polarization with a liquid crystal variable retarder (LCVR) and a polarizer. The output beam is finally focused in a single mode fiber (SM) and its spectrum is measured with an Optical Spectrum Analyzer (OSA).

The input optical pulse state of polarization is pre-selected to be left-handed circularly polarized, with polarization vector $\hat{\mathbf{e}}_{\text{in}} = (\hat{\mathbf{x}} - i\hat{\mathbf{y}})/\sqrt{2}$,

by using a polarizer, a half-wave plate and a quarter-wave plate. For an input optical pulse with a Gaussian spectrum, i.e., $S_{\rm in}(\nu) \propto \exp[-\pi^2\tau^2(\nu-\nu_0)^2/\ln 2]$, where $\tau$ is the pulse temporal width (FWHM), the input electric field reads (in the time domain) after pre-selection as

$$\mathbf{E}_{\rm in}(t) = E_0 \exp\left[-2\ln 2\, t^2/2\,\tau^2 + i2\pi\nu_0 t\right] \hat{\mathbf{e}}_{\rm in}\,. \tag{4.1}$$

A weak measurement is realized by means of a polarization-dependent temporal delay implemented using a Michelson interferometer configuration. A polarizing beam splitter (PBS) divides the input pulse into two orthogonally linearly polarized components with horizontal ($\hat{\mathbf{x}}$) and vertical ($\hat{\mathbf{y}}$) polarizations, which propagate along the two arms of a Michelson interferometer. By changing the length of each arm, $d_1$ and $d_2$, we introduce different time delays $T_1 = 2\,d_1/c$ and $T_2 = 2\,d_2/c$ for each polarization component. The two delayed pulses recombine at the same PBS.

In the post-selection stage, the outgoing pulse is projected into a state of polarization given by the polarization vector $\hat{\mathbf{e}}_{\rm out} = (\hat{\mathbf{x}} + \exp(i\Gamma)\hat{\mathbf{y}})/\sqrt{2}$, where $\Gamma$ determines the final state of polarization of the output pulse. For $\Gamma = -\pi/2$, the input and output polarization states coincide, while for $\Gamma = \pi/2$, they are orthogonal. After post-selection, the electric field of the output signal writes

$$\mathbf{E}_{\rm weak}(\nu) = \frac{E_{\rm in}(\nu)}{\sqrt{2}}\left[\exp\left(i2\pi\nu T_1\right)\hat{\mathbf{x}} - i\exp\left(i2\pi\nu T_2\right)\hat{\mathbf{y}}\right]\,. \tag{4.2}$$

$$\mathbf{E}_{\rm out}(\nu) = \frac{E_{\rm in}(\nu)}{2}\left[\exp\left(i2\pi\nu T_1\right) - i\exp\left(i2\pi\nu T_2 - i\Gamma\right)\right]\hat{\mathbf{e}}_{\rm out}\,. \tag{4.3}$$

Equation (4.3) shows that the post-selection polarization angle ($\Gamma$) determines for which frequencies the interference between signals coming from the horizontally and vertically polarized pulses, delayed by $T = T_1 - T_2$, is constructive or destructive. The output spectral density is given by

$$S_{\rm out}(\nu) = \frac{S_{\rm in}(\nu)}{2}\left[1 + \cos\left(2\pi\nu T - \Gamma - \pi/2\right)\right]\,, \tag{4.4}$$

where $S_{\rm in}(\nu)$ is the input laser spectrum.

In order to characterize the output spectrum, we measure as a function of the post-selection angle $\Gamma$, the central frequency shift $\Delta f = \int {\rm d}\nu\, \nu\,[S_{\rm out}(\nu) - S_{\rm in}(\nu)]$ and the insertion loss $L = -10\log P_{\rm out}/P_{\rm in}$, with $P_{\rm in,out}$ being the input (output) power $P_{\rm in,out} = \int {\rm d}\nu\, S_{\rm in,out}(\nu)$ of the pulse. From Eq. (4.4), the

central frequency shift $\Delta f$ of the output pulse can be easily calculated and yields

$$\Delta f = -\frac{\ln 2}{\pi}\left(\frac{T}{\tau^2}\right)\frac{\gamma \sin\left(2\pi\nu_0 T - \Gamma - \pi/2\right)}{1+\gamma\cos\left(2\pi\nu_0 T - \Gamma - \pi/2\right)}\,, \tag{4.5}$$

where $\gamma = \exp[-\ln 2\ T^2/\tau^2]$ quantifies the degree of overlap between the pulses $T$ with respect to the input pulse duration $\tau$. Note that for a weak coupling regime of operation, $\gamma \approx 1$. The frequency shift given by Eq. (4.5) is accompanied by insertion losses which write

$$L = -10\log\left[\frac{1}{2}\left(1+\gamma\cos\left(2\pi\nu_0 T - \Gamma - \pi/2\right)\right)\right]\,. \tag{4.6}$$

In general, to keep a good signal-to-noise ratio in the detection stage there is a trade-off between the frequency shift observable for a specific value of the time delay and the amount of losses that can be tolerated, given by Eq. (4.5) and Eq. (4.6), respectively.

## 4.2 Experimental implementation

The experimental implementation of the scheme used to measure small temporal delays between optical pulses is shown in Fig. 4.3. The scheme is implemented using only linear optics elements and requires only spectral measurements, hence making its implementation practical.

A femtosecond fiber laser (Calmar Laser - Mendocino) centered at 1549 nm, generates pulses of temporal width 320 fs (bandwidth 11 nm), average power 3 mW and repetition rate 20 MHz. The spectral density measured shows characteristic high-frequency small wrinkles due to cavity effects in the laser system.

The state of polarization of the pulses is selected to be circular by using a polarizer followed by a half-wave plate and quarter-wave plate. The light pulses enter the Michelson-Morley interferometer, composed of a Polarizing Beam Splitter (PBS), two quarter-wave plates (QWP) and two mirrors, that generate a polarization-dependent delay. The PBS divides the input pulse into two pulses, with equal power and with orthogonal polarizations, that travel through different paths of the interferometer, and also recombines the two pulses after reflection.

One of the mirrors is mounted on a translation stage (TSTG) that moves the mirror along the beam's trajectory and generates the difference in optical path. The TSTG used is an OWIS DIGI-MIC that provides a minimal

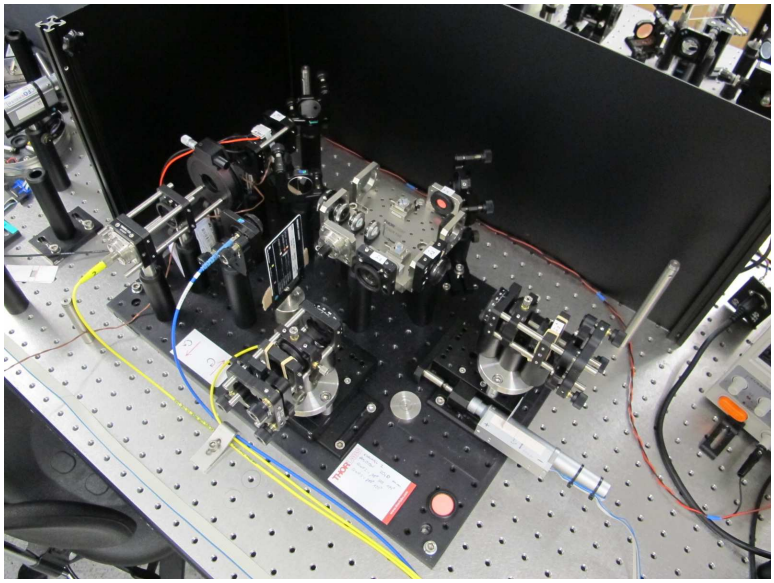

(a)

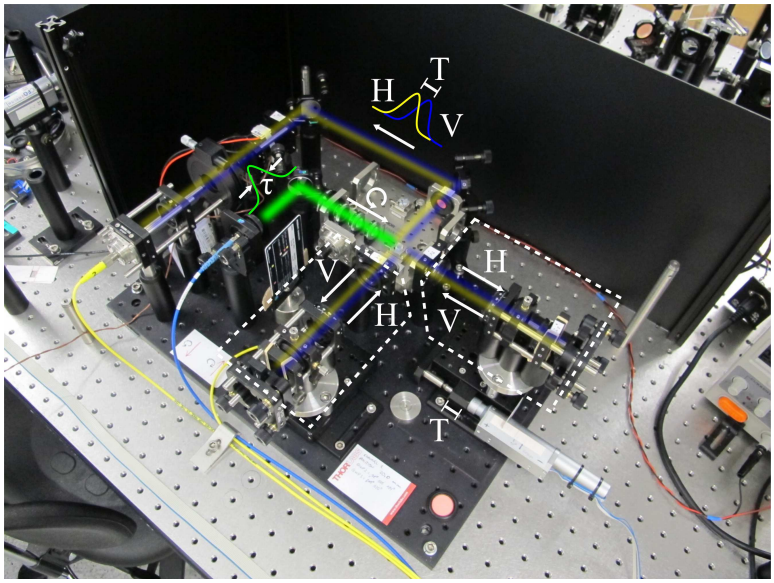


(b)

Figure 4.3: (a) Experimental setup. (b) Optical beam layout. The input pulse of duration $\tau$ (FWHM) and the output beam, composed of two pulses delayed by $T$ with orthogonal polarizations are indicated. The delay between pulses is introduced by moving a mirror in one of the arms of the interferometer using a translation stage as in the experiment described in Chapter 3. However, in this case, the delay $T$ is scanned over the interval $[-15\,\mu\text{m}, +15\,\mu\text{m}]$, which guarantees the weak interaction condition.

step of $1\,\mu$m, which corresponds in time to a delay of $\approx 7$ fs. Notice that even though the TSTG could only provide micrometer size steps, the weak value condition is easily satisfied since the laser pulse duration 320 fs is significantly higher than the polarization-dependent delay that is given in multiples of $\approx 7$ fs.

After the weak measurement, the output beam state of polarization is projected into a particular state of polarization with a liquid crystal variable retarder (LCVR) (Thorlabs - LCC1113-C) followed by a polarizer. Since the relation between post-selection angle and the LCVR voltage is non-linear and highly temperature dependent, an additional temperature controller based on a Peltier cell was used. The output beam is finally focused in a single mode fiber (SM) and its spectrum is measured with an Optical Spectrum Analyzer (Yokogawa - AQ6370) that provides a resolution of 0.02 nm. Each spectrum is obtained after averaging five data sets in the interval [191.5 THz, 195.5 THz].

## 4.3 Experimental results

Recently, it has been demonstrated that high precision phase estimation based on weak measurements can be achieved even using commercial light-emitting diodes [15]. Indeed, Li et al. [32] showed that the scheme proposed by Brunner and Simon also works with large-bandwidth incoherent light. On the one hand, the use of white light allows to obtain in a straightforward manner a light source with an enormous bandwidth, which allows to measure very small phase differences. On the other hand, many applications make use of high-repetition femtosecond sources that allows to perform multiple measurements in millisecond or microsecond time intervals [46], allowing the measurement of time-varying phase differences in this time scale. This is the scenario that we consider here.

Figures 4.4 and 4.5 show measurements of the spectral changes in the regime $T \ll \tau$, when one makes use of the idea of weak value amplification. The plots show the shift of the central frequency of the spectrum for two different temporal delays: $T = 53$ fs and $T = 22$ fs. Panel (a) in Fig. 4.4 shows the measured frequency shift and panel (b) plots the measured insertion loss for $T = 53$ fs (similarly panels (a) and (b) in Fig. 4.5 for $T = 22$ fs). The dotted lines are best theoretical fits using the measured input spectrum in Eq. (4.3). All other plots in Figs.4 4.4 and 4.5 show measured spectral densities of the output signal for some selected cases and the corresponding theoretical predictions when the measured input spectral density is used in

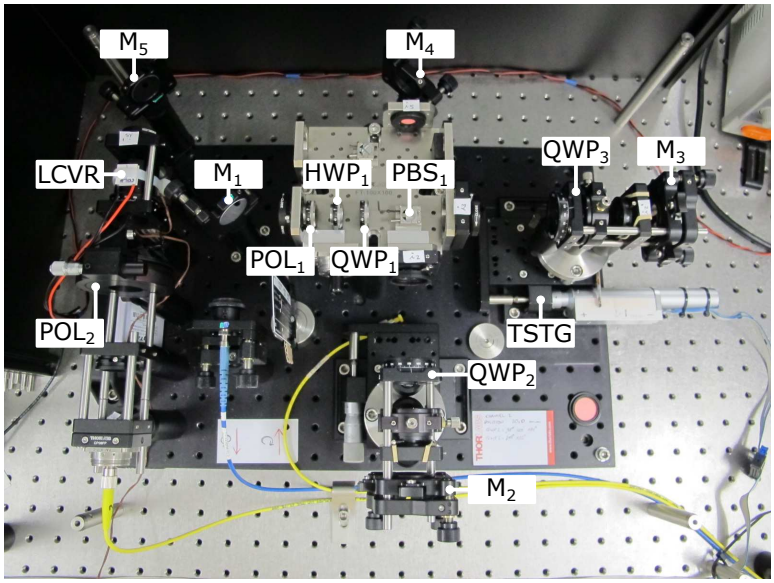


(c)

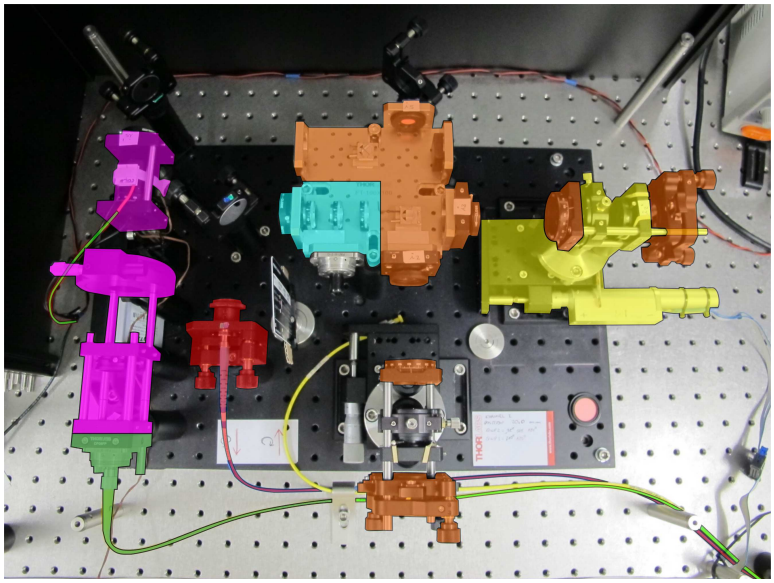

(d)

Figure 4.3: (c) Detail of the components used. M: mirror, HWP: Half-Wave Plate, QWP: Quarter-Wave Plate, PBS: Polarizing Beam Splitter, POL: Polarizer, TSTG: Translation Stage, LCVR: Liquid Crystal Variable Retarder. (d) Stages used to: i) select the initial state of polarization (cyan), ii) perform a polarization-dependent delay (orange), iii) select the final state of polarization (magenta). The input port, translation stage and output port, are colored in red, yellow and green respectively.

Eq. (4.3).

Inspection of Figs. 4.4 and 4.5 allow to highlight two working regimes, corresponding to the presence of high or low losses. For $\Gamma = -3\pi/2 + 2\pi\nu_0 T$, there is no central frequency shift and losses are maximum. The output spectral density features a double-peak spectral density. For small angle deviations around this value, central frequency shifts of the spectral density up to hundreds of gigahertz are clearly observable. However, insertion losses are also the highest in this regime, measuring values over 60 dB. This regime corresponds to the case usually studied in weak value amplification where the input and output polarization states are nearly orthogonal [28]. The applicability of the weak value amplification in this high-amplification regime is limited to cases where the energy of the input signal can be increased, since the intensity of the detected signal is severely decreased [3].

Nevertheless, we demonstrate here that even in the regime where the input and output polarization states have a significant overlap, hence featuring smaller insertion losses, weak value amplification remains useful. Even though the frequency shifts measured in this regime are generally smaller, reaching only few tens of GHz instead of hundreds of GHz, losses do not exceed a few dB. For $\Gamma = -\pi/2 + 2\pi\nu_0 T$, there is no shift of the central frequency again. The pre- and post-selected polarizations are almost equal, hence introducing almost no losses. The spectral density of the output pulse is almost equal to the input spectral density. For small angle deviations around this value, the temporal delay produce small shifts of the central frequency, which vary almost linearly with respect to the post-selection angle. Importantly, these frequency shifts are accompanied by small insertion losses.

### 4.3.1 What can we measure with this scheme?

The results presented here naturally raise the question of what are the ultimate limits of the scheme, in terms of central frequency shifts and losses. Brunner et al. [28] and Strubi et al. [29] have estimated theoretically that weak value amplification of temporally delayed optical pulses could allow the measurement of attosecond temporal delays. Indeed, Xu. et al. [15] have demonstrated the measurement of phase differences as small as $\Delta\varphi \sim 10^{-3}$, which corresponds to an optical path delay difference of $d = \lambda/(2\pi)\ \Delta\varphi \sim 130$ pm, by using a large bandwidth LED source. In principle, one can always make use of white light sources with bandwidths in excess of 100 nm, as the ones use in Optical Coherence Tomography for

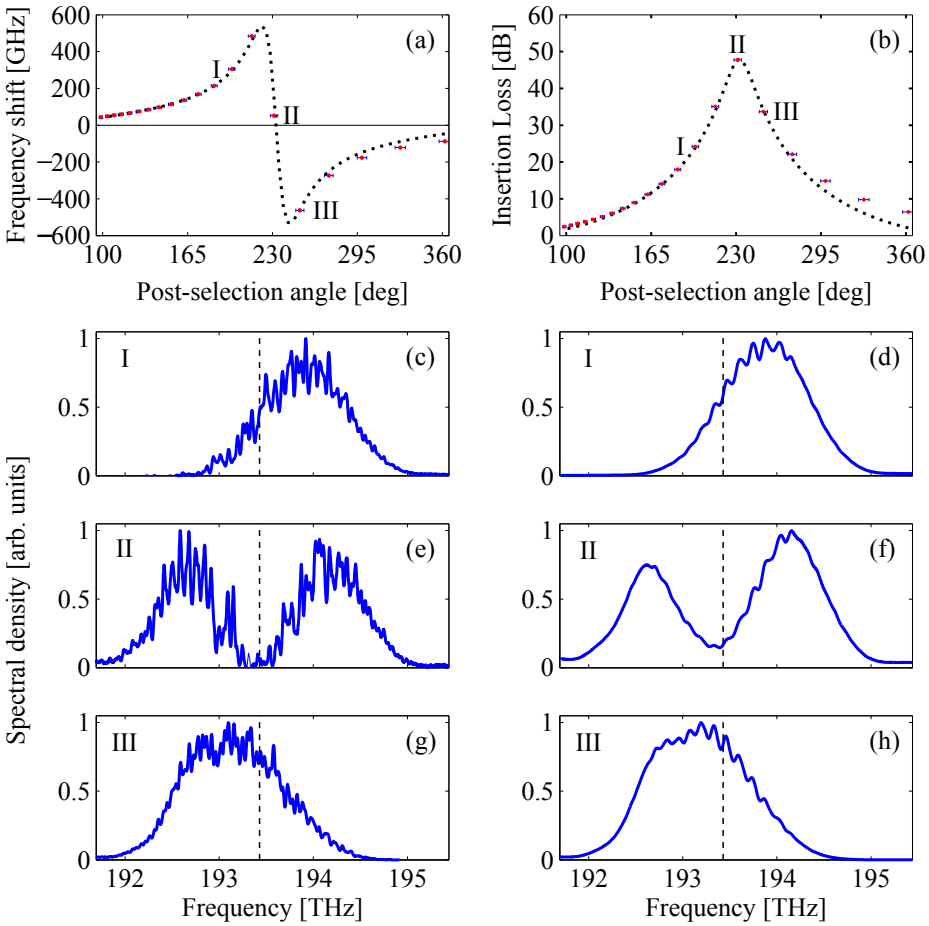


Figure 4.4: Measurement of the central frequency shift induced by weak value amplification for a delay of $T = 53\,\mathrm{fs}$ between pulses with orthogonal polarizations. Measured frequency shift (a) and insertion loss (b) as a function of the post-selection angle $\Gamma$. Dots (with error bars) are experimental results, and the dotted lines are best theoretical fits using the measured input spectrum in Eq. (4.3). The best fits are obtained for $T = 53\,\mathrm{fs}$ in (a) and (b). Panels (c), (e) and (g) (measured) and (d), (f) and (h) (theory) shows the spectral density for some selected cases, as indicated by the corresponding labels in (a) and (b). To help the eye, the central frequency of the input pulse ($\nu_0 = 193.44\,\mathrm{THz}$) is represented by a dashed line in all plots. The experiment is performed at a temperature of 34.1°C. Error bars in all plots assume that temperature variations during the experiment are in the range of $\pm 1°C$, which translates in random changes of the angle of post-selection $\Gamma$.

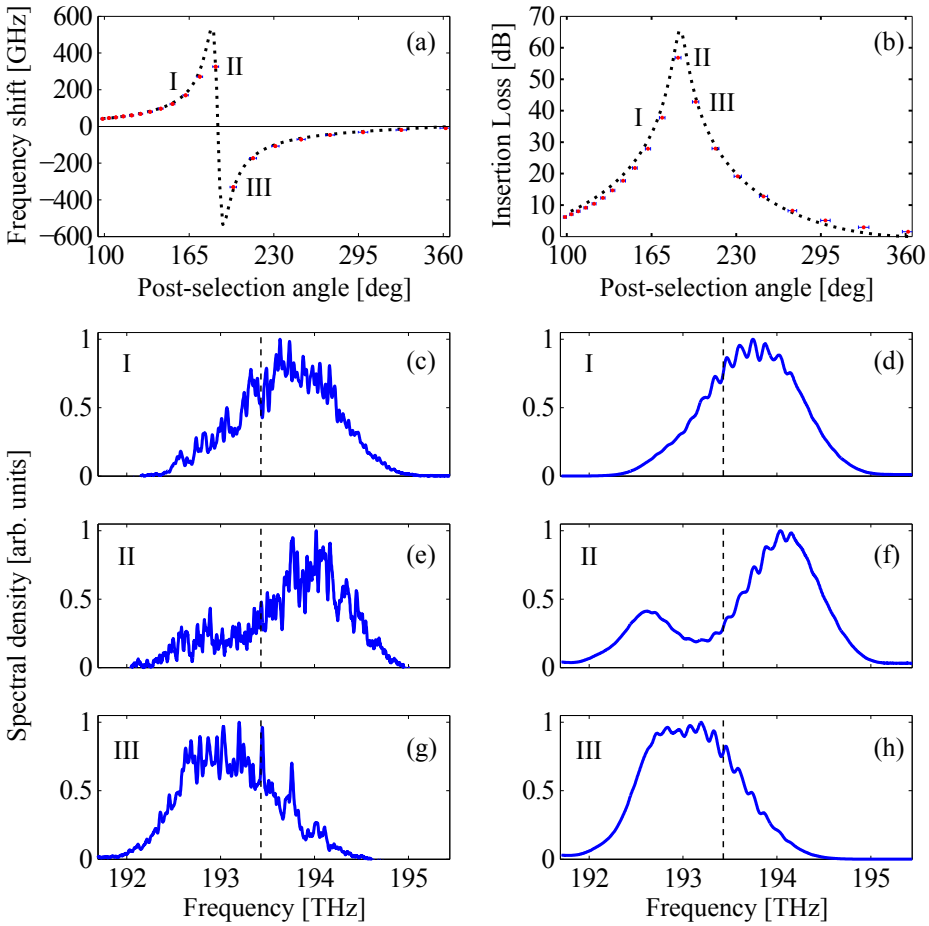


Figure 4.5: Measurement of the central frequency shift induced by weak value amplification for a delay of $T = 22\,\text{fs}$ between pulses with orthogonal polarizations. Measured frequency shift (a) and insertion loss (b) as a function of the post-selection angle $\Gamma$. Dots (with error bars) are experimental results, and the dotted lines are best theoretical fits using the measured input spectrum in Eq. (4.3). The best fits are obtained for $T = 22\,\text{fs}$ in (a) and (b). Panels (c), (e) and (g) (measured) and (d), (f) and (h) (theory) shows the spectral density for some selected cases, as indicated by the corresponding labels in (a) and (b). To help the eye, the central frequency of the input pulse ($\nu_0 = 193.44\,\text{THz}$) is represented by a dashed line in all plots. The experiment is performed at a temperature of 34.1°C. Error bars in all plots assume that temperature variations during the experiment are in the range of $\pm 1°C$, which translates in random changes of the angle of post-selection $\Gamma$.

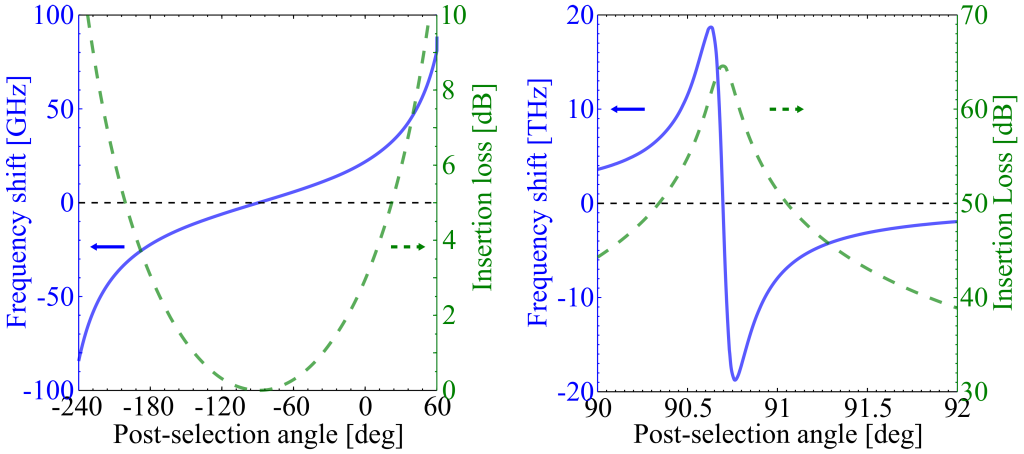


Figure 4.6: Feasibility of the measurement of attosecond temporal delays with femtosecond pulses. Polarization dependent frequency shift induced by a $T = 10$ as time delay of pulses of duration $\tau = 10$ fs. Panel (a). Low-loss regime. Panel (b). High-loss regime. The solid blue line corresponds to the frequency shift and the green dashed line to the insertion losses. Notice the different scales in the $x$ and $y$ axis in (a) and (b).

submicron resolution [54], to enhance the frequency shift detected.

Figure 4.4 shows the frequency shift and the insertion loss expected, as a function of the post-selection state of polarization, when a temporal delay of $T = 10$ as is introduced between two optical pulses with Gaussian shape and duration $\tau = 10$ fs (FWHM). Fig. 4.6(a) depicts the low-loss regime, where smaller frequency shifts can be observed in exchange for much lower losses. In the case shown, frequency shifts up to 100 GHz, corresponding to 0.8 nm, are generated with losses below 12 dB. Most spectrometers, as the one used in our experiments, can reach resolutions of up to 0.02 nm, rendering measurable these frequency shifts. In the high-loss regime, shown in Fig. 4.6(b), one can observe greater frequency shifts, as high as $\sim 20$ THz ($\sim 160$ nm). Unfortunately, its measurement is also accompanied by higher losses, over 60 dB. The existence of the low-loss working regime, somehow not so extensively considered as the high-loss regime, can thus enhance the applicability of the weak value amplification idea, as demonstrated here.

# Conclusion

In this chapter we have demonstrated a spectral interference effect between two optical pulses with a temporal delay much smaller than the pulse duration, inspired from the concepts of weak measurements and weak value amplification. In particular, we have demonstrated a shift of the central frequency of two slightly delayed femtosecond pulses which can be used to reveal the value of the temporal delay itself. Importantly, the central frequency shifts can be observed even in a regime, not so-often considered, where insertion losses are small, which broadens the applicability of the method demonstrated.

Our scheme is implemented by using only linear optics elements and requires spectral measurements, hence making its implementation practical. The ultimate sensitivity of our scheme can provide observable frequency shifts for temporal delays of the order of attoseconds using femtosecond laser sources. Our scheme thus appears as a promising method for measuring small and rapidly varying temporal delays.

## Main publication by the author related to the contents of this chapter

**L. J. Salazar-Serrano**, D. Janner, N. Brunner, V. Pruneri, and J. P. Torres, "Measurement of sub-pulse-width temporal delays via spectral interference induced by weak value amplification", Physical Review A **89**, 012126 (2014).

CHAPTER

# FIVE

# DESIGN AND DEMONSTRATION OF A NEW TYPE OF HIGHLY-SENSITIVE TUNABLE BEAM DISPLACER

*“ To invent, you need a good imagination and a pile of junk. ”*

Thomas A. Edison, *1955*

A polarization beam displacer (BD) is a device that splits an input polarized beam into two spatially separated beams that propagate parallel with orthogonal polarizations. Most commercially available BDs are made of birefringent crystals, where the propagation direction of an ordinary (horizontal) polarized beam is unchanged, whereas the extraordinary (vertical) component deviates inside the crystal. A BD can also be used to displace spatially the position of a single optical beam, for example by using an input beam with vertical polarization at the input [55].

The resulting beam separation is specific for each material and its maximum value depends on the amount of birefringence of the material and on the crystal length, which is typically on the order of centimeters, limiting the maximum separation achievable to a few millimeters.

Most of the times there are other requirements that a *good* BD should fulfill, even though these conditions heavily depends on the particular application under consideration. For instance, adding tunability to the spatial displacement is desired in some applications where a small lateral displacement is required to be used as a reference to perform high resolution mea-

surements [56]. In other applications, achromaticity of the displacement should be preserved [57]. Many applications require that a previous displacement should be reversed [58, 59]. Nowadays, new techniques are being explored to generate beam displacements as required for any specific scenario [60, 61].

To the best of our knowledge, a scan of the position of a single beam can be implemented either by using an arrange of moving mirrors [60, 62], a plane-parallel plate or a tunable beam displacer (TBD) [63]. For all the devices mentioned, the beam shift results from the mechanical rotation of an optical element. This condition imposes a technical limitation on the sensitivity of the beam displacer since it directly relates to which sensitivity we can achieve when performing the rotation. For the sake of example, in a plane-parallel plate displacer one can obtain a typical beam shift of $\approx 12.5\,\mu$m/deg, where the proportionality factor depends on the thickness of the plate and its index of refraction. For a TBD, the proportionality factor is $\approx 5\,$mm/deg which is determined mainly by the distance from the mirrors to the PBS.

In this chapter we introduce and demonstrate a new type of highly-sensitive tunable beam displacer that can outperform the limitations imposed by the use of movable optical elements that use deflection to displace the beam. The scheme, based on the concept of weak value amplification [2, 4], allows to convert two beams with orthogonal polarizations that slightly overlap in space into a single beam whose center can be tuned by only modifying the linear polarization of the output beam. The scheme presented turns to be advantageous with respect to other alternatives based on reflections or/and refractions induced by the rotation of a specific optical elements because the ultimate sensitivity is determined by the step size of the rotation stage used to rotate the post-selection polarizer which can be very small.

The chapter is organized as follows. In Section 5.1 we present the main idea behind the scheme to implement a highly sensitive tunable beam displacer based on weak value amplification. This first section is divided in two parts: in the first part, the heart of the device, the tunable beam displacer (TBD), is described and in the second part the theoretical background is introduced, and where some results are discussed. In Section 5.2, the experimental implementation is described and in Section 5.3, the experimental results are presented and discussed.

## 5.1 Description of a highly sensitive tunable beam displacer based on WVA

In chapter 4, we presented a scheme that can be used to measure a delay $T$ between two overlapping pulses of duration $\tau$. When the weak measurement condition is satisfied (i.e. when $T \ll \tau$) interference effects appear that give rise to a reshaping of the spectral density. Information about the time delay can be retrieved by measuring the shift of the frequency centroid of the output beam with respect to the central frequency of the optical source.

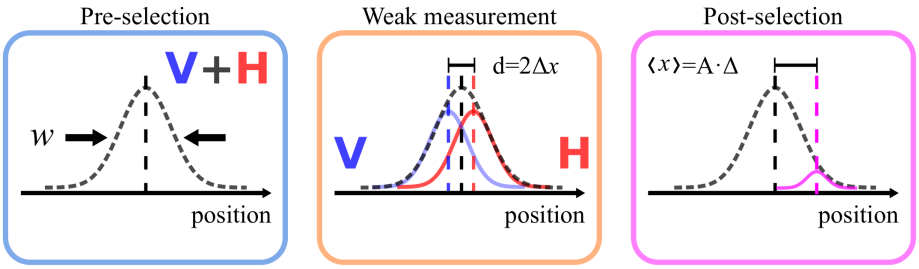


Figure 5.1: Weak value amplification scheme. In this case we make use of a real weak value to reshape the output's beam cross section.

The same principle can be applied in the spatial domain if the Gaussian pulses in time are now replaced by beams with a Gaussian spatial profile. As a consequence, the weak measurement condition is now reformulated as $\Delta x \ll w$, where $\Delta x$ is a displacement in the x-direction between two beams with orthogonal polarizations and $w$ is the input's beam width. Similarly, in the weak value amplification scheme the polarization-dependent delay is now replaced by a polarization-dependent displacement.

Figure 5.1 presents a weak value amplification scheme where two polarizers are used to select the initial and final states of polarization before and after the weak interaction, respectively, and the weak interaction is generated by a device that couples the spatial and the polarization degrees of freedom of the input beam.

Up to now, most of the weak value based applications have been proposed to enhance a tiny polarization dependent effect [13, 14, 30]. All of them work in the regime where the pre-selection and post-selection states are chosen to be nearly orthogonal and therefore the novelty of the application is the large amplification factor. In sharp contrast we make use of the de-amplification effect that is also present in the weak value amplification scheme when the pre-selection and post-selection are chosen to be nearly

parallel [11]. The new scheme gives rise to a tunable beam displacement with sub-micrometric resolution that achieve such displacement without using any mechanical element.

In practice, the weak interaction is implemented by a tunable beam displacer which is a device that divides an initially polarized beam into two parallel beams whose separation can be tuned continuously. The two output beams are linearly polarized with either vertical or horizontal polarization and no optical path difference is introduced between them.

### 5.1.1 Tunable Beam Displacer (TBD)

A polarization beam displacer is a device that splits an input polarized beam into two spatially separated beams that propagate parallel with orthogonal polarizations [55]. Commercially available beam displacers are made of birefringent materials like Calcite crystal, Barium Borate ($\alpha - \mathrm{BBO}$) crystal, Rutile crystal or Yttrium Vanadate ($YVO_4$) among others.

In these devices, due to the intrinsic birefringence of the material, the propagation direction of the ordinary polarized beam is unchanged whereas the extraordinary component deviates inside the crystal [64]. The resulting beam separation is specific for each material and its maximum value depends on the crystal length, which is typically on the order of centimeters, limiting the maximum separation achievable to a few millimeters. To get an idea of the capabilities of current technologies, the model BD40 of Thorlabs, provides a 4 mm displacement for $\lambda = 1550\,\mathrm{nm}$. Similarly, Altechna offers a broad variety of beam displacements made of Calcite or $YVO_4$, that generate beam displacements over a range of 1 mm to 3 mm.

Apart from a spatial separation, standard beam displacers also introduce a temporal delay between the beams with orthogonal polarization, which may be detrimental in some applications. Notwithstanding, a tunable beam displacer divides an initially polarized beam into two parallel beams whose separation can be continuously tuned. The two output beams are linearly polarized with either vertical or horizontal polarization and no optical path difference is introduced between them.

We have developed a device that is based on the "adjustable Wollaston like prism" described by Feldman et al. [65] with the difference that our device does not use quarter wave-plates that limit the spatial quality of the beam output and the wavelength range of operation. The geometry of our implementation of a TBD is shown in Fig. 5.2 (a).

Two mirrors are fixed to a L-shaped platform that is free to rotate an

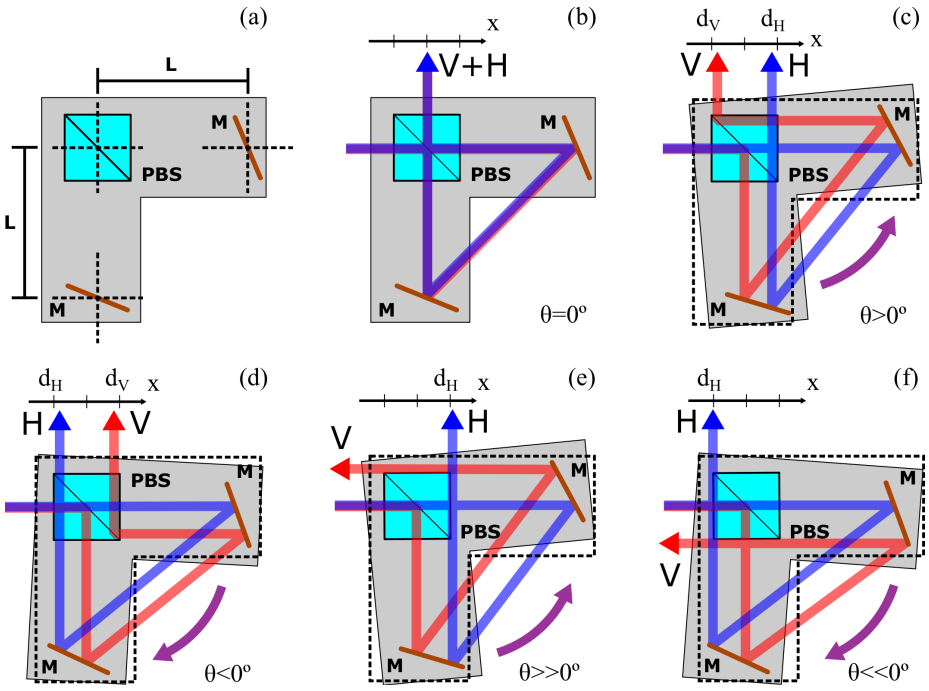


Figure 5.2: (a) Basic scheme of our TBD. Two mirrors (M) are positioned at a distance $L$ from a PBS and fixed to a L-shaped platform that is free to rotate an angle $\theta$ with respect to the PBS center. (b) The orthogonally polarized output beams spatially overlap ($\theta = 0°$). In (c) we consider the case $\theta > 0°$, $d_H > 0$ and $d_V < 0$, whereas (d) corresponds to a case with $\theta < 0°$, $d_H < 0$ and $d_V > 0$. (e) and (f) present two limiting cases: $\theta \gg 0°$ and $\theta \ll 0°$, respectively, where the beam with vertical polarization is no longer reflected on the PBS and thus $d_V$ is no longer defined.

angle $\theta$ with respect to the polarizing beam splitter (PBS) center. The mirrors are positioned equidistant at a distance $L$ with respect to the PBS. When the angle $\theta$ is different from zero, the input beam splits into two parallel propagating beams with orthogonal polarizations separated by a distance proportional to the rotation angle. If the input beam polarization is horizontal or vertical, a single beam is obtained at the output. The wavelength dependence of the device as well as the maximum separation between the beams achievable are mainly limited by the PBS characteristics.

When $\theta = 0°$, as shown in Fig. 5.2 (b), the two output beams with orthogonal polarizations propagate collinearly superimposed on each other. On the other hand, when the platform is rotated, the beams with orthogonal polarizations no longer overlap in space and emerge at the output separated

by a distance that depends on the angle $\theta$, $L$, the size of the PBS and the beam diameter. In Fig. 5.2 (c), $d_H$ and $d_V$ correspond to the beam separations for the horizontal and vertical output components, measured with respect to the central position of the beams, when the platform is not rotated. When $\theta > 0°$, anti-clockwise rotation as shown in Fig. 5.2 (c), the beam with horizontal polarization is separated by a distance $d_H > 0$ with respect to the reference position, whereas for the beam with vertical position $d_V < 0$. In contrast, when the platform is rotated in the opposite direction, $\theta < 0°$, clockwise rotation as shown in Fig. 5.2 (d), the polarization of the output beams are reversed and thus the sign of $d_H$ and $d_V$. Figs. 5.2 (e) and 5.2 (f) illustrate the limiting cases where the angle $\theta$ is such that the beam with vertical polarization is no longer reflected by the PBS and thus it is not collinear to its output pair with horizontal polarization.

It would be desirable to obtain an analytical expression that would relate the beam displacement with $\theta$, $L$, the size of the PBS and the input beam diameter. Even though, the geometry of the TBD is simple, such an analytical expression for the displacement is not straightforward because the relationship between the angle $\theta$ and the orientation of the mirrors is not easily manageable. Fortunately, since the device can be modeled only by consecutive reflections on the mirrors and the PBS (refractions on the PBS can be neglected due to the fact that all the beams impinging and emerging from the PBS are perpendicular to its surface), a numerical model is at hand. We developed a ray tracing model in which reflections are calculated according to the law of reflection considering the position where a beam hits the mirror. In addition, the PBS is modeled as a two sided mirror in which the vertical polarization reflects two times and the horizontal component is only transmitted.

The solid and dashed lines in Fig. 5.3 show the beam displacements for the output beams with horizontal $d_H$ (solid) and vertical $d_V$ (dashed) polarizations obtained with our ray tracing model as a function of $\theta$ for two different values of $L$: Fig. 5.3 (a) corresponds to $L = 6.5\,\text{cm}$ and Fig. 5.3 (b) to $L = 10\,\text{cm}$. For completeness, experimental results for $d_H$ and $d_V$ in the interval $-1.5° \leq \theta \leq +1.5°$ are also shown as circles and triangles, respectively. The experimental results and the predictions from the ray tracing model are in excellent agreement in the region where two parallel beams with orthogonal polarizations are obtained at the output.

In all cases, it is observed a central region where the separation between the beams varies linearly with the angle $\theta$. Beyond this region, our model is not valid: $d_V$ presents a discontinuity that corresponds to values of $\theta$ in

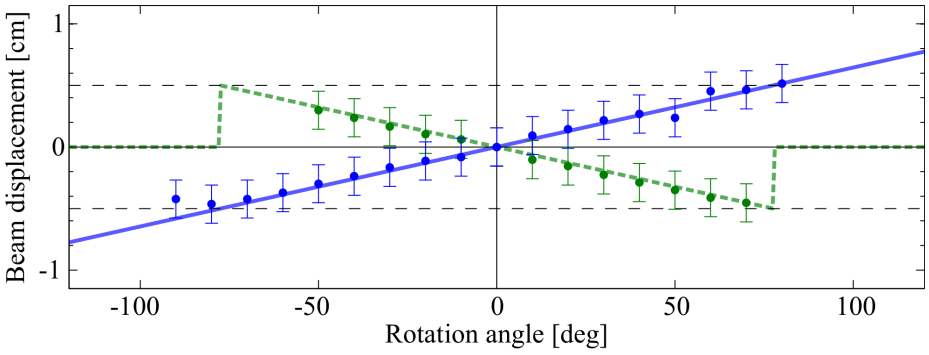


(a)

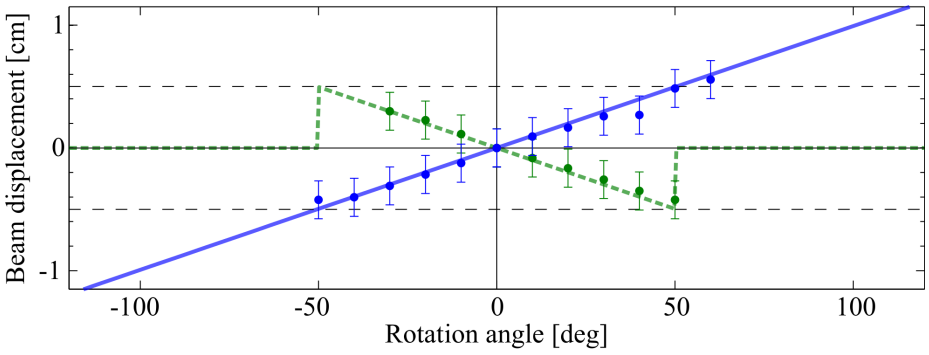


(b)

Figure 5.3: Comparison between theoretical and experimental results. The expected displacements from the ray tracing model for $d_H$ (blue solid line) and $d_V$ (dashed green line) are shown as a function of the rotation angle $\theta$. Experimental results are presented as circles for $d_H$ and as triangles for $d_V$. (a) and (b) correspond to configurations with $L = 6.5\,\text{cm}$ and $L = 10\,\text{cm}$, respectively. The PBS is 1 cm wide. Horizontal dashed line: maximum separation, as determined by the PBS size. Error bars indicate an input beam diameter of 3 mm.

which the vertical component is no longer reflected on the PBS and thus the output beams with vertical and horizontal polarizations do not propagate collinearly (see Figs. 5.2 (e) and 5.2 (f)). The maximum separation, shown as horizontal dashed lines in Figs. 5.3 (a) and 5.3 (b), is limited by the PBS size. As $L$ increases, the sensitivity of the tunability of the device improves, which is revealed by noticing that for both polarizations, the slope of the beam displacement in Fig. 5.3 (b) is steeper than the corresponding slope in Fig. 5.3 (a).

Our ray tracing model also reveals a useful feature of the TBD: The temporal delay between the orthogonally polarized beams, arising from the optical path difference, is zero. At first sight, since the beams impinge on different regions of the mirrors and PBS, one expects that they travel a different optical path; however, our ray tracing model reveals that this is not the case. Interestingly, this feature is valid for any value of $\theta$, and adds a unique feature to our TBD with respect to other beam displacers.

### 5.1.2 A highly-sensitive tunable beam displacer based on WVA

A beam displacement can be generated using either a set of mirrors that are arranged in a configuration that allows to change the position of the output beam when one or various mirrors are rotated, a transparent plane-parallel plate of certain thickness such as a tweaker plate, a thin film polarizer, or a plate beam splitter or a tunable beam displacer.

To get an idea of the displacements that can be achieved using commercial devices, Thorlabs offers a tweaker plate, model XYT-A, which is a 2.5 mm thick plane-parallel plate. Similarly, II-VI UK LTD offers thin film polarizers made of either ZnSe or Ge that can be used to split or combine an input beam into two components with orthogonal polarizations. The polarizer is oriented at Brewster's angle with respect to the input beam so that the vertical polarization is highly reflected whereas the horizontal is transmitted. In addition, Edmund optics offers a plate beam splitter, model #49-684, that is a 3 mm thick N-BK7 splitter that transmits 70% of the input power and operates in the visible regime. All the devices mentioned allow to generate sub-mm level precision beam displacements.

Regarding transparent plane-parallel plates, the beam displacement is proportional to the plate thickness, index of refraction and the rotation angle. This is because the plate of certain thickness is rotated with respect to an axis parallel to the surfaces that offsets the position of the input beam after consecutive refractions in the air-plate and plate-air interfaces.

In contrast, for the TBD presented in Section 5.1.1, two mirrors fixed to a platform are rotated with respect to a polarizing beam splitter (PBS). When the angle is different from zero, the input beam splits into two parallel propagating beams with orthogonal polarizations separated by a distance proportional to the rotation angle. If the input beam polarization is horizontal or vertical, a single beam is obtained at the output.

For all the cases mentioned above the beam shift results from the me-

chanical rotation of an optical element. This condition imposes a technical limitation on the sensitivity of the beam displacer since it directly relates to which sensitivity we can achieve when performing the rotation. In a plane-parallel plate displacer one can obtain a typical beam shift of $\approx 12.5\,\mu$m/deg, where the proportionality factor depends on the thickness of the plate and its index of refraction. For a TBD, the proportionality factor is $\approx 5\,$mm/deg which depends mainly on the distance from the mirrors to the PBS.

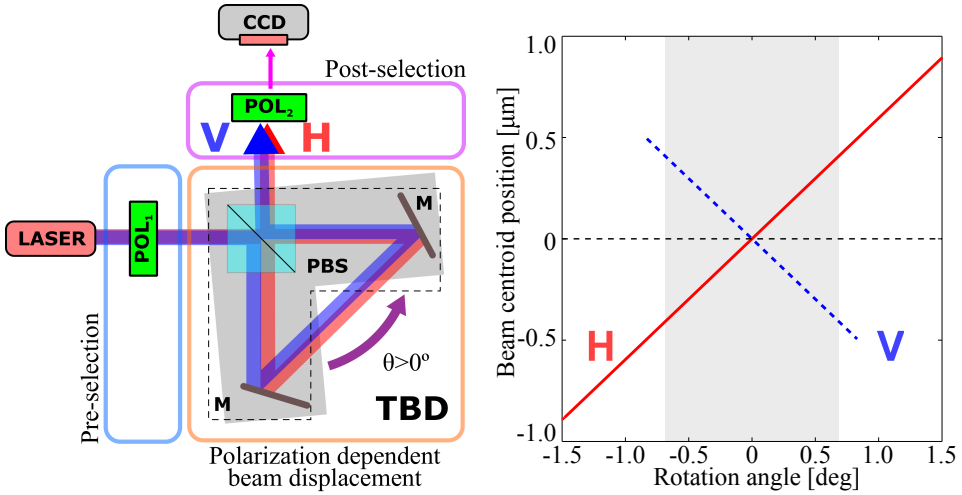


Figure 5.4: (a) Experimental scheme. Input and output polarizers, $POL_1$ and $POL_2$, control the corresponding polarizations. A polarization-dependent beam displacement is introduced by the tunable beam displacer. $POL_1$ and $POL_2$: polarizers, PBS: polarizing beam splitters; M: Mirrors. (b) Beam displacement before traversing the second polarizer for the horizontal (solid line) and vertical (dashed line) components of the optical beam a function of the rotation angle $\theta$. The shaded region indicates the region where the beams with orthogonal polarizations still overlap.

The experimental scheme presented in Fig. 5.4(a) introduces a new type of highly-sensitive tunable beam displacer that can outperform the limitations imposed by the use of deflection to displace the beam. In our scheme, we do not make use of the tunable reflections or/and refractions induced by the rotation of a specific optical element. Instead, we make use of the concept of weak value amplification [2, 4], that allows to convert two beams with orthogonal polarizations that slightly overlap in space into a single

beam whose center can be tuned by only modifying the linear polarization of the output beam.

Consider an input beam that propagates in the $\hat{\mathbf{z}}$ direction with a Gaussian-like beam shape of width $w$ (at $1/e^2$). By using a polarizer rotated at an angle $\alpha = +45°$, the initial polarization is set to $\hat{\mathbf{e}}_{\rm in} = (\hat{\mathbf{x}}+\hat{\mathbf{y}})/\sqrt{2}$, by $\mathrm{POL}_1$, where $\hat{\mathbf{x}}$ and $\hat{\mathbf{y}}$ denote the horizontal and vertical transverse directions, respectively. After the pre-selection stage, the shape in the transverse plane $(x, y)$ of the input electric field is given by

$$\mathbf{E}_{\rm in}(x, y) = E_0 \exp\left[-(x^2 + y^2)/2w^2\right] \hat{\mathbf{e}}_{\rm in}\,, \tag{5.1}$$

where $E_0$ is the peak amplitude and $w$ is the $1/e$ beam width.

In a second stage, the TBD is set to an angle $\theta$. The TBD splits the input beam into two parallel beams with orthogonal polarizations. The output beams are shifted a distance $+\Delta x$ for the component with horizontal polarization and $-\Delta x$ for the component with vertical polarization with respect to the direction of the output beam when $\theta = 0°$.

The TBD is set to operate in the shaded region shown in Fig. 5.4(b), where the two output beams with orthogonal polarizations still overlap. i.e., the distance between the two beam centroids $2\Delta x$ is small compared with the input's beam diameter $w$. Since the spatial shape of the beam in the $x$ and $y$ coordinates are independent, and the displacement is only considered along the $x$ direction, for the sake of simplicity we will be looking only at the beam shape along the $x$ direction. After this stage, the field reads

$$\begin{aligned}\mathbf{E}_{\rm weak}(x) &= \frac{E_0}{\sqrt{2}}\Big\{ \cos\beta \exp\left[-(x-\Delta x)^2/2w^2 + i\,\phi\right] \hat{\mathbf{x}} \\ &+ \sin\beta \exp\left[-(x+\Delta x)^2/2w^2\right] \hat{\mathbf{y}} \Big\}\,,\end{aligned} \tag{5.2}$$

where $\phi$ takes into account any optical path difference that can be introduced mainly due to misalignment.

In the last stage, the output beam state of polarization is projected in the state $\hat{\mathbf{e}}_{\rm out} = \cos\beta\,\hat{\mathbf{x}} + \sin\beta\,\hat{\mathbf{y}}$ by using the polarizer $\mathrm{POL}_2$ that is rotated at an angle $\beta$ with respect to the horizontal axis. The amplitude of the output beam writes

$$\begin{aligned}\mathbf{E}_{\rm out}(x) &= \frac{E_0}{\sqrt{2}}\Big\{ \cos\beta \exp\left[-(x-\Delta x)^2/2w^2 + i\,\phi\right] \\ &+ \sin\beta \exp\left[-(x+\Delta x)^2/2w^2\right] \Big\}\hat{\mathbf{e}}_{\rm out}\,.\end{aligned} \tag{5.3}$$

The intensity of the output beam, given by $I_{\text{out}}(x) = 2\,\epsilon_0 c|E_{\text{out}}(x)|^2$, writes

$$\begin{aligned} I_{\text{out}}(x) &= \frac{I_0}{2}\Big\{ \cos^2\beta \exp\left[-(x-\Delta x)^2/w^2\right] \\ &+ \sin^2\beta \exp\left[-(x+\Delta x)^2/w^2\right] \\ &+ \exp\left[-\Delta x^2/w^2\right] \sin 2\beta \exp\left[-x^2/w^2\right] \cos\phi \Big\}, \end{aligned} \tag{5.4}$$

after using the Product Theorem for Gaussian Functions presented in Appendix B. Note that the factor $\exp\left[-\Delta x^2/w^2\right]$ in the last line of Eq. (5.4) carries information about the degree of spatial overlap between the output pulses, or in other words, the strength of the weak coupling between polarization and beam position.

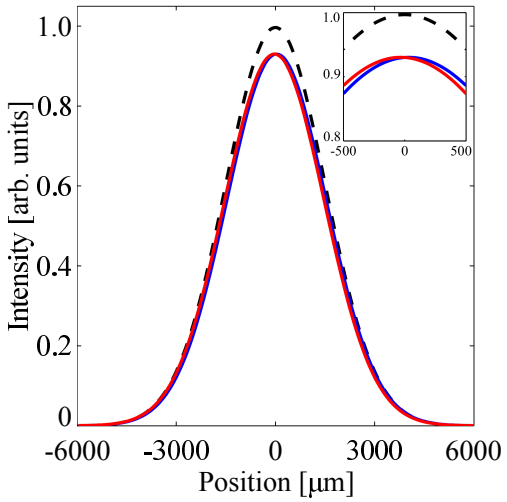


Figure 5.5: Beam profile after traversing the second polarizer for three different output polarizations ($\beta = 30°$, $\beta = 45°$ and $\beta = 60°$). The insets shows more clearly the small beam displacements for different post-selections of the output state of polarization.

Figure 5.5 plots the beam intensity given by Eq. (5.4) for three different angles: $\beta = 30°$, $\beta = 45°$ and $\beta = 60°$. An angle $\beta = 45°$ corresponds to choosing the polarization of the output beam equal to the polarization of the input beam. Inspection of Fig. 5.5 shows that $I_{\text{out}}(x)$ corresponds to a single peaked Gaussian-like distribution whose center is slightly shifted with respect to the input beam centroid by an amount smaller than $\Delta x$, far less than the beam width. We also observe that this small shift is polarization-dependent, i.e., it depends on the value of the angle $\beta$.

This effect can be easily visualized by calculating the beam's centroid by replacing Eq. (5.4) in the expression $\langle x \rangle = \int x\, I_{\text{out}}(x)\, \mathrm{d}x / \int I_{\text{out}}(x)\, \mathrm{d}x$. We also calculate the insertion loss (expressed in decibels) $L = -10 \log_{10}[P_{\text{out}}/P_{\text{in}}]$ where $P_{\text{in}}$ and $P_{\text{out}}$ designate the input and output power of the beams, respectively. By making use of Eq. (5.4), we obtain that the centroid of the output beam reads

$$\langle x \rangle = \frac{\cos 2\beta}{1 + \gamma \sin 2\beta \cos \phi}\, \Delta x\,, \tag{5.5}$$

where $\gamma = \exp\left(-\Delta x^2 / w^2\right)$ is close to unity since $\Delta x \ll w$. Similarly, the insertion loss is given by

$$L = -10 \log_{10} \left[ \frac{1}{2} \left(1 + \gamma \sin 2\beta \cos \phi\right) \right]. \tag{5.6}$$

Figures 5.6(a) and 5.6(b) show the position of the beam centroid and the insertion loss as a function of the post-selection angle $\beta$ of $\text{POL}_2$. The displacements $\pm\Delta x$ for each polarization are indicated by horizontal dashed lines. Eq. (5.5) shows that the beam centroid $\langle x \rangle$ is related to the polarization-dependent displacement $\Delta x$ by a relationship of the form $\langle x \rangle = A \cdot \Delta x$, where $A$ is the amplification factor given in Eq. (5.5). Most applications of the weak value amplification concept (see, for instance, [38] and [39] for two recent reviews about this topic) are interested in a regime where $A \gg 1$. However this is not the only regime where weak value amplification can be of interest [11]. Here, on the contrary, we are interested in the regime $A \ll 1$, where beam displacements much smaller than the beam width of the input beam are observed.

In this regime, close to $\beta = 45°$ (input and output polarizations are similar) the position of the centroid of the output beam varies almost linearly with respect to the post-selection angle over the range $-\Delta x \leq \langle x \rangle \leq +\Delta x$ (see Fig. 5.6(a)), and the insertion loss is small for the same interval (see Fig. 5.6 (b)), making the weak value amplification scheme described in Fig. 5.4(a) suitable for implementing a low-loss highly sensitive tunable beam displacer where the spatial shift is controlled by projection into a given polarization state, with no optical elements that deflect the beam.

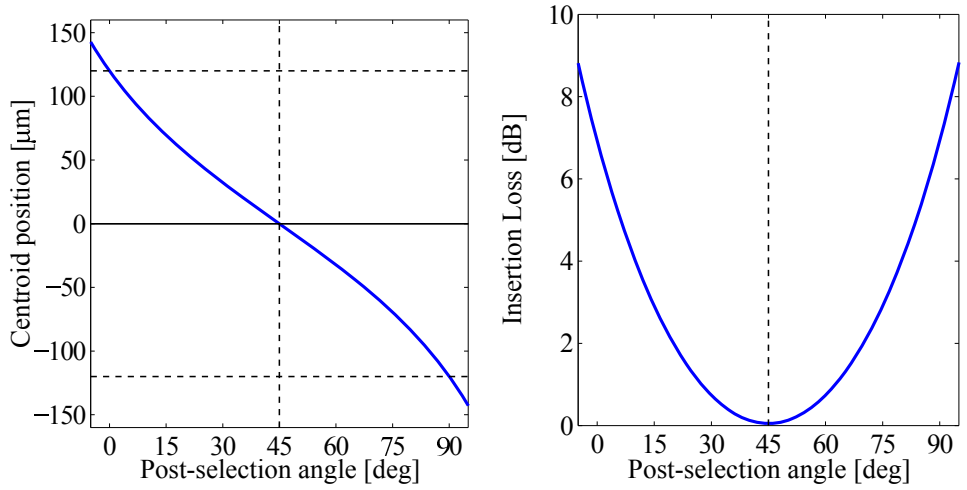


Figure 5.6: (a) Lateral displacement of the centroid of the output beam as a function of the polarization of selected, given by the post-selection angle $\beta$. As a reference, the displacements $\pm\Delta x$ for the polarization dependent shift are indicated by horizontal dashed lines. (b) Insertion loss as a function of the post-selection angle $\beta$. Data: $\Delta x = 120\,\mu$m, $\gamma = 0.9$ and $\phi = 0°$.

## 5.2 Experimental implementation

### 5.2.1 The tunable beam displacer

To corroborate the TBD theoretical model described in section 5.1.1, we implemented the experimental setup shown in Fig. 5.2(a). A He-Ne (Thorlabs HNL020R-EC) laser was used to generate the input beam with a Gaussian spatial profile (beam diameter: 3 mm). The beam is subsequently polarized at 45° by using a polarizer (Melles Griot 03PT0101/C). The beam impinges on a 1.0 cm PBS, antireflection coated for 633 nm, and the two orthogonal polarization components separated by the PBS are then reflected by aluminium mirrors (diameter 2.54 cm) placed on the L-shaped platform that is allowed to rotate at specific values of $\theta$ by using a manual rotational stage. At the output, the beam position is recorded by a camera and the centroid of the different images, $d_H$ and $d_V$, is measured.

For initial alignment, $\theta$ is set to zero and the angle for each mirror is set such that each beam reflected onto the mirrors propagates towards the PBS center and only one beam is seen in the camera. The centroid of this image sets the reference to measure afterwards $d_H$ and $d_V$.

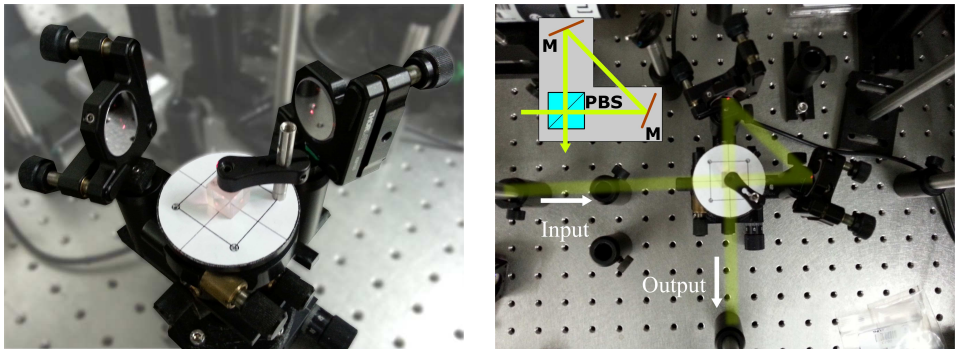


(a) (b)

Figure 5.7: (a) Image corresponding to the implementation of the tunable beam displacer. (b) Optical beam layout.

### 5.2.2 A highly-sensitive tunable beam displacer based on WVA

In order to demonstrate the feasibility of the scheme for a highly-sensitive tunable beam displacer presented in Section 5.1.2, we have implemented the set-up shown in Fig. 5.4(a). The input beam with Gaussian spatial profile is generated using a He-Ne laser (Thorlabs HRP005S) and the input beam is Gaussian with a beam waist of $\sim 600\,\mu$m ($1/e^2$). Two Glan-Thomson polarizers (Melles Griot 03PT0101/C) are used to select the initial and final states of polarization before and after the TBD. The initial state of polarization is selected by rotating the first polarizer at $+45°$, and the output polarization is selected by rotating the second polarizer an angle $\beta$ with respect to the horizontal direction. The experimental implementation is shown in Fig. 5.8.

The TBD, implemented with the components $M_3$, $M_4$, $PBS_1$ and $RSTG$ in Fig. 5.8(c), and highlighted in orange in Fig. 5.8(d), is composed of two aluminum mirrors, positioned equidistantly from a 1.0 cm polarizing beam splitter (PBS), and fixed to a L-shaped platform that is free to rotate an angle $\theta$ with respect to the PBS center. For a given angle, the separation between the two output beams depends on $\theta$, the distance from the mirrors to the PBS, and the sizes of the input beam and the PBS. In the setup, the distance from each mirror to the PBS is set to 7 cm and the platform is rotated with a custom made motorized rotation stage.

The output beam shape is detected by a CCD camera (Santa Barbara Instruments ST-1603ME) with $1530 \times 1020$ pixels ($9\,\mu$m pixel size). With


(a)

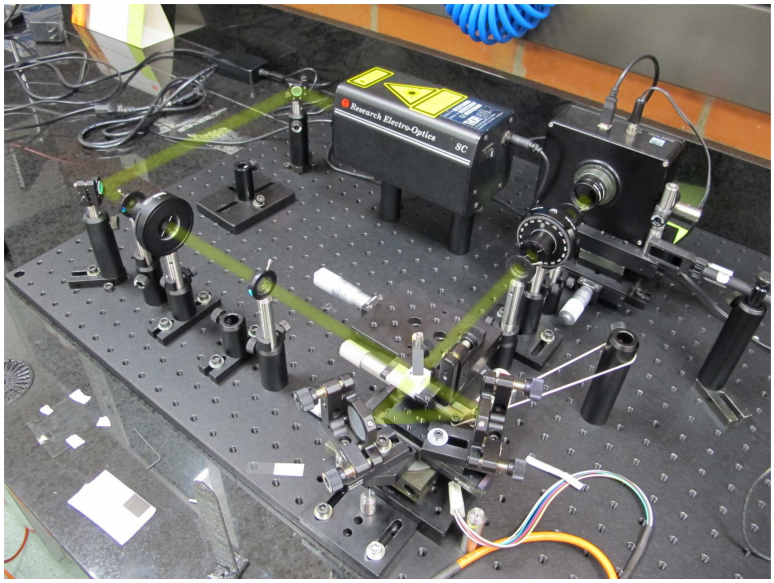


(b)

Figure 5.8: (a) Experimental setup. (b) Optical beam layout.

the data measured, the corresponding centroid position is calculated using a simple MATLAB routine. To avoid CCD saturation, neutral density absorptive filters (Thorlabs - Serie NE-A) are used.

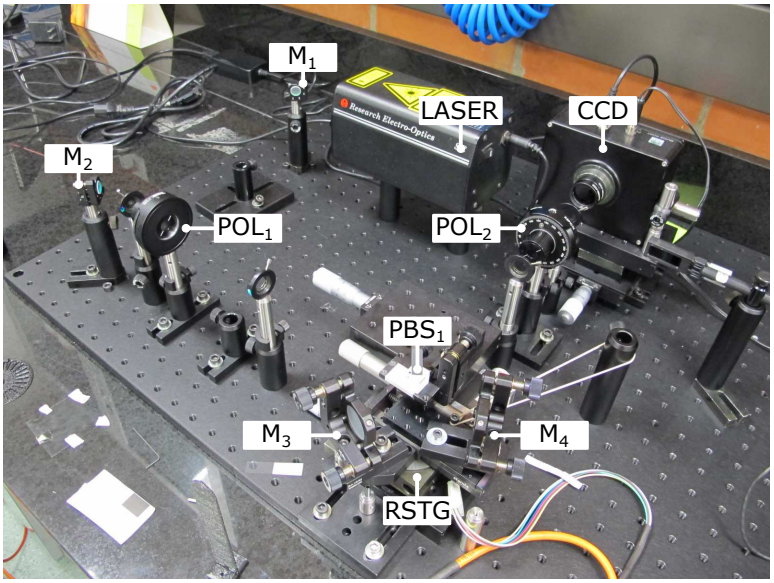


(c)

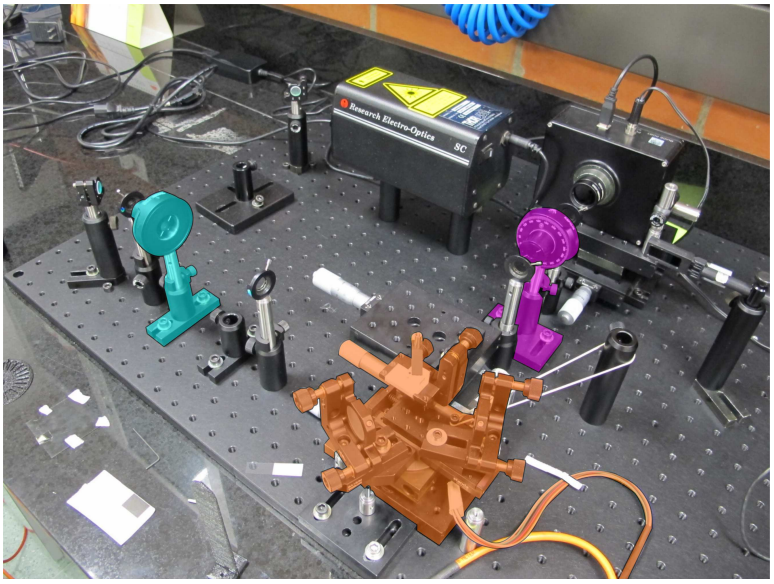

(d)

Figure 5.8: (c) Detail of the components used. PBS: Polarizing Beam Splitter, POL: Polarizer, RSTG: Rotating Stage, M: Mirror. (d) Stages used to: i) select the initial state of polarization (cyan), ii) perform the weak measurement (orange), iii) select the final state of polarization (magenta).

Before running the experiment an initial alignment is carried out without using the output polarizer. This preparation consists of two steps. Firstly, the input beam enters the TBD, $\theta$ is set to zero and the angle for each mirror is set such that each beam reflected on the mirrors propagates towards the PBS center and only one beam is seen in the camera. The centroid of this image sets the reference point from which the new beam's centroid position, $\langle x \rangle$, will be measured. Secondly, the L-shaped plaque is rotated by an angle $\theta$ to define the small initial displacement, $\Delta x$, between the components with orthogonal polarization. For our experiment, $\Delta x = 120\,\mu$m, which yields $\gamma = \exp[-(\Delta x)^2/w^2]$ equal to 0.96. Once the reference centroid is defined, the output polarizer $POL_2$ is introduced. A set of images are recorded for different values of $\beta$, and their corresponding centroids are calculated.

## 5.3 Experimental results

The experimental results are presented as dots in Fig. 5.9. Fig. 5.9(a) depicts the measured beam displacement $\langle x \rangle$ as a function of the output polarizer angle ($\beta$). The error bars take into account the uncertainty introduced by the CCD camera pixel size of $9\,\mu$m. The solid line in Fig. 5.9(a) corresponds to the best data fit using Eq.(5.3) where $\phi$ is the fitting parameter. From the best fit we obtain $\phi = 54°$, which corresponds to a difference in optical path of $\sim 0.094\,\mu m$, mainly due to misalignment.

In the region $0° \leq \beta \leq 90°$ we observe that the beam's centroid varies almost linearly with respect to the output polarizer angle. In this interval, the best fit gives $\langle x \rangle = -2.32\,\beta + 114.24\ \mu m$, which demonstrates a region of operation that goes approximately between $-120\,\mu$m to $+120\,\mu$m, in agreement with the initial displacement of $\Delta x = 120\,\mu$m.

The sensitivity of the shift is limited by the angular resolution achievable when selecting the output polarization. As an example, if a manual rotation mount with resolution of 10 arcmin is used to select the output polarization, a minimum beam displacement step of $380\,nm$ can be obtained without using opto-mechanical components.

In Fig. 5.9(b) we show the measured (dots) and theoretical (solid line) insertion loss, given by Eq. (5.4) for $\phi = 54°$ and $\gamma = 0.96$. The maximum insertion loss in this region is $\sim 3\,$dB.

Interestingly, the relationship between the beam's centroid shift and the output polarization is almost linear, and the sensitivity of the beam displacement is limited by the sensitivity available for selecting the output polarization. From the measurements, we were able to shift the centroid

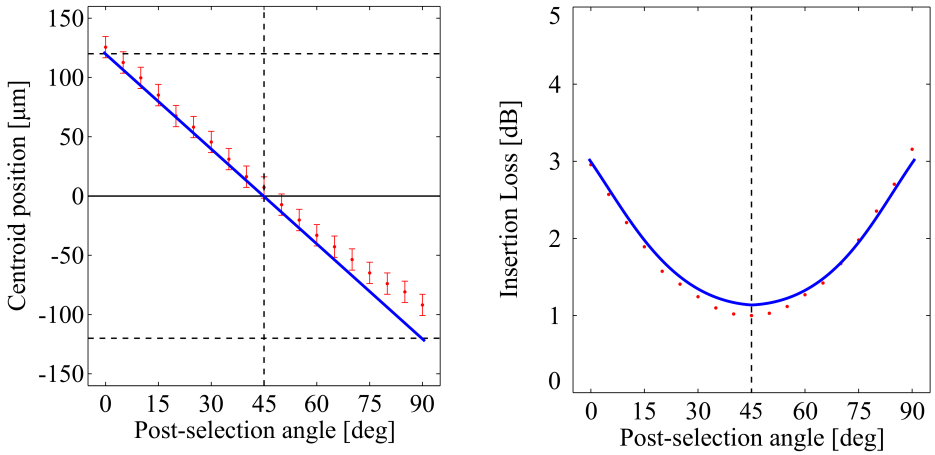


(a) (b)

Figure 5.9: (a) Measurement (dots) of the beam's centroid position (left axis), amplification factor $A$ (right axis), and fit (solid line) following Eq. (5.3), as a function of the post-selection angle $\beta$. (b) Measured insertion loss (dots) and fit (solid line) obtained from Eq. (5.4) as a function of $\beta$.

of a Gaussian beam with a beam waist of $\sim 600\,\mu$m, over an approximate interval that goes from $-120\,\mu$m to $+120\,\mu$m in steps of less than $\sim 1\,\mu$m.

## Conclusions

In this chapter we have introduced and demonstrated a new kind of tunable beam displacer (TBD) that allows to transform an input polarized beam into two parallel beams spatially separated by a tunable distance. The device is very attractive for applications where temporal compensation is not available since it does not introduce a temporal delay between the output beams. In addition, the maximum beam separation and the spectral characteristics are determined mainly by the polarizing beam splitter used in its implementation.

Thereafter, we use the TBD to implement a polarization-dependent beam displacer that, in conjunction with pre-selection and post-selection polarization stages which constitute a weak value amplification scheme, allows to design a highly sensitive beam displacer. The centroid of a Gaussian beam can be shifted a distance much smaller than its beam width without the need to use the deflection of optical elements. The beam's centroid position can be displaced by controlling the polarization in the post-selection

stage. The dependence between the centroid's position and the angle of polarization is almost linear. From the experimental results we were able to shift the centroid of a Gaussian beam with a beam waist of $\sim 600\,\mu$m, over the interval $-120\,\mu$m to $+120\,\mu$m in steps of less than $\sim 1\,\mu$m by rotating the post-selection polarizer between 0° and 90°.

## Main publications by the author related to the contents of this chapter

**L. J. Salazar-Serrano**, D. A. Guzmán, A. Valencia, and J. P. Torres, "Demonstration of a highly-sensitive tunable beam displacer with no use of beam deflection based on the concept of weak value amplification", Optics Express **23**, 10097 (2015).

**L. J. Salazar-Serrano**, A. Valencia, and J. P. Torres, "Tunable beam displacer", Review of Scientific Instruments **86**, 033109 (2015).

CHAPTER

# SIX

# ENHANCING THE SENSITIVITY OF FIBER BRAGG GRATING TEMPERATURE SENSORS

> *Science is, on the whole, an informal activity, a life of shirt sleeves and coffee served in beakers.*
>
> Sir George Porter, *1968*

A Fiber Bragg Grating (FBG) used as a sensor can be readily understood as an optical bandpass filter whose central frequency depends on the value of a certain variable, maybe temperature or strain. FBG sensors have attracted great interest in the past three decades due to its intrinsic characteristics such as immunity to electromagnetic interference, small size, lightweight and its multiplexing capability.

There is a large variety of interrogation schemes available to retrieve the value of the variable of interest, such as those based on interferometric methods, tunable-filters, tunable-light-sources or using other FBGs such as tilted fiber gratings, to name a few [66]. Current technologies can offer a sensitivity of $\sim 0.01$ nm/°C for temperature measurements. From the detection point of view achieving such resolution translates into increasing the complexity of the interrogation scheme, becoming at the same time more expensive.

This explain the interest in looking for new methods and techniques to enhance the sensitivity of FBG-based systems. For instance, one option could be to develop new methods that could increase the shift of the central frequency of the filter for a given change of temperature or strain. In

an alternative scenario, this could also be used for measuring even tinier temperature or strain changes that would produce in this way measurable frequency changes using present-day detection schemes.

In this chapter we present a *proof-of-concept* experiment aimed at increasing the sensitivity of FBG sensors by making use of a *weak value amplification* scheme. The system developed makes use of a broad-band light source, two FBGs at slightly different temperatures, and an optical spectrum analyzer (OSA), all of them interconnected by optical circulators and optical fibers. The technique requires only linear optics elements for its implementation, and appears as a promising method for increasing the sensitivity than state-of the-art sensors can currently provide. From the experimental results, the scheme implemented is able to generate a shift of the centroid of the spectrum of a pulse of $\sim 0.035$ nm/°C, a nearly four-fold increase in sensitivity over the same FBG system interrogated using standard methods.

This chapter is organized as follows. Section 6.1 provides a brief introduction to FBGs, where the working principle is discussed and the standard interrogation scheme used to measure temperatures is presented. In Section 6.2 the scheme based on weak value amplification that allows to enhance the sensitivity of temperature sensors based on FBGs is described. In Section 6.3 the experimental implementation is presented and in Section 6.4 experimental results are discussed.

## 6.1 A brief summary on fiber Bragg gratings (FBG)

Fiber Bragg Gratings (FBG) constitute nowadays a key ingredient of many devices used in communication and sensing applications [67]. They can easily be integrated in all-fiber systems, their dielectric nature make them non-conducting, immune to electromagnetic interference, chemically inert and current technology allows to tailor the properties of FBGs to adapt to the specific requirements of each application [68, 69, 70].

An FBG, shown in Fig. 6.1(a), is an optical component fabricated from a single mode fiber whose core has been modified by introducing a periodic modulation of the effective refractive index of refraction by exposing the core of the fiber to a periodic pattern of intense ultraviolet light. This modulation is referred as grating. Each plane with a change in index of refraction acts as a partially reflective mirror that generates a region that

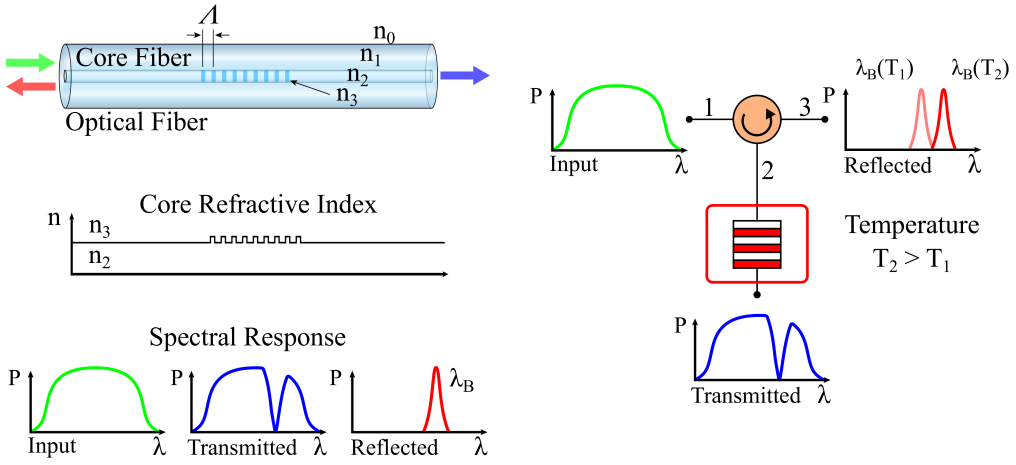


Figure 6.1: (a) Fiber Bragg Grating structure and spectral response when light with a broad spectrum is coupled into the fiber. (b) An standard scheme used to interrogate a FBG using a circulator. The central wavelength of the reflected signal varies with respect to temperature.

scatters the light that is guided along the core of the fiber. At each plane, light is reflected and transmitted. All the reflected components may interfere constructively or destructively depending on the relation between the light's wavelength and the grating period. For the case of constructive interference the relation is termed as Bragg condition and the wavelength at which the reflected components combine to yield one large reflection is called the Bragg wavelength, $\lambda_B$.

In general, when considering a given wavelength, the Bragg condition is satisfied by setting the grating period ($\Lambda$) to approximately half the light's wavelength. As a result the FBG is transparent to components with wavelengths other than the Bragg wavelength. Interestingly the grating period can be changed physically by expanding or contracting the fiber's material by subjecting it to some strain or by changing its surrounding temperature. This feature is what allows the measurement of temperature or strain using FBGs by monitoring the central wavelength of the reflected signal.

Figure 6.1(b) shows a standard procedure used to measure temperatures using a FBG. It makes use of a circulator, a three-port optical component that allows light to travel in only one direction by interconnecting port 1 with port 2 and port 2 with port 3, with considerably low losses. When light

enters port 1, it goes to port 2 where the FBG filters the signal spectrally and reflects back a portion that exits at port 3. The output can be monitored using an optical spectrum analyzer.

For current commercial configurations aimed at measuring temperatures where the FBG is isolated from any source of strain, the position of the centroid of the spectrum of the reflected light varies linearly with respect to the temperature with a sensitivity ranging from 0.008 nm/°C to 0.014 nm/°C determined by the material of the fiber. As a result spectrum analyzers with high resolution are required to measure temperatures changes below one degree centigrade.

## 6.2 A scheme for measuring temperature based on FBGs via weak value amplification

As presented in Chapter 2 and in Appendix A, *weak value amplification* (WVA) is a signal enhancement technique that is used in metrology applications to measure tiny changes of a variable that cannot be detected otherwise because of technical limitations, i.e., the insufficient sensitivity of the detection system. Here we are interested in measuring the difference in central frequency, and thus the difference in temperature, between the spectra coming from two FBGs that are almost overlapping.

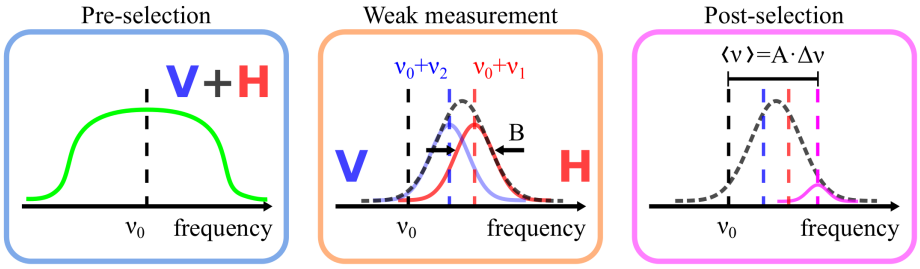


Figure 6.2: Weak value amplification scheme. In this case we make use of a real weak value to measure a temperature dependent frequency shift $\Delta\nu = \nu_1 - \nu_2$.

The weak value amplification scheme is composed of three steps: preselection of polarization, weak coupling and post-selection of polarization (Fig. 6.2). In the first stage a light source that generates a beam with a broad spectrum, centered in $\nu_0$, is polarized at +45° by using a linear polarizer. In the second stage, a weak interaction is implemented by a

device that generates a polarization dependent frequency shift by filtering the input's beam spectrum. The component with vertical polarization is filtered spectrally using a FBG of bandwidth $B$ that is centered in $+\nu_2$, whereas the component with horizontal polarization is centered in $+\nu_1$. Since the difference $\Delta\nu = \nu_1 - \nu_2$ is smaller than the FBG bandwidth $B$, the interaction is termed as "weak interaction". In the last stage, the output polarization is again selected using a linear polarizer rotated at an angle $\beta$, that is chosen to be near $-45°$.

Due to the post-selection, the beams with horizontal and vertical polarizations interfere. The centroid of the output spectrum ($\langle\nu\rangle$) is displaced with respect to $\nu_0$ by an amount $\mathcal{A}\cdot\Delta\nu$, where $\mathcal{A}$ is an amplification factor that depends on $\beta$, the overlap ratio $\Delta\nu/B$ and the optical path difference that may be introduced between components with orthogonal polarizations in the weak interaction stage. Even though $\mathcal{A}$ can be very large, its value is limited because the intensity of the signal at the output is severely reduced since the pre-selection and post-selection polarizers are set to be nearly orthogonal.

### 6.2.1 Theoretical background

Consider the experimental scheme depicted in Fig. 6.3 that performs the three steps of a weak value amplification scheme described above.

In the first step, the initial state of polarization of a broad-band light source, centered in $\nu_0$, is pre-selected to be linear using polarizer $\mathrm{POL}_1$ rotated at $+45°$ with respect to the vertical. To perform a weak interaction, the beam is first divided into two orthogonal components with the polarizing beam splitter $\mathrm{PBS}_1$. The vertical and horizontal polarizations are filtered using the FBGs connected to circulators $\mathrm{CIRC}_1$ and $\mathrm{CIRC}_2$, respectively. As a result, the spectrum of each component is filtered according to the scheme presented in Fig. 6.1(b).

Since the two FBGs have identical period, the spectrum of each component has approximately the same bandwidth, $B$, whereas its central frequency is slightly different according to the surrounding temperature of each FBG. Finally, the output of each circulator is combined in a single beam using $\mathrm{PBS}_2$. After $\mathrm{PBS}_2$ the electric field in the frequency domain reads

$$\mathbf{E}_{\mathrm{weak}}(\nu) = \frac{E_0}{\sqrt{2}}\left\{\exp\left[-\frac{(\nu-\nu_0-\nu_1)^2}{2B^2}\right]\hat{\mathbf{x}} + \exp\left[-\frac{(\nu-\nu_0-\nu_2)^2}{2B^2} + i(2\pi\nu\tau+\delta)\right]\hat{\mathbf{y}}\right\}, \tag{6.1}$$

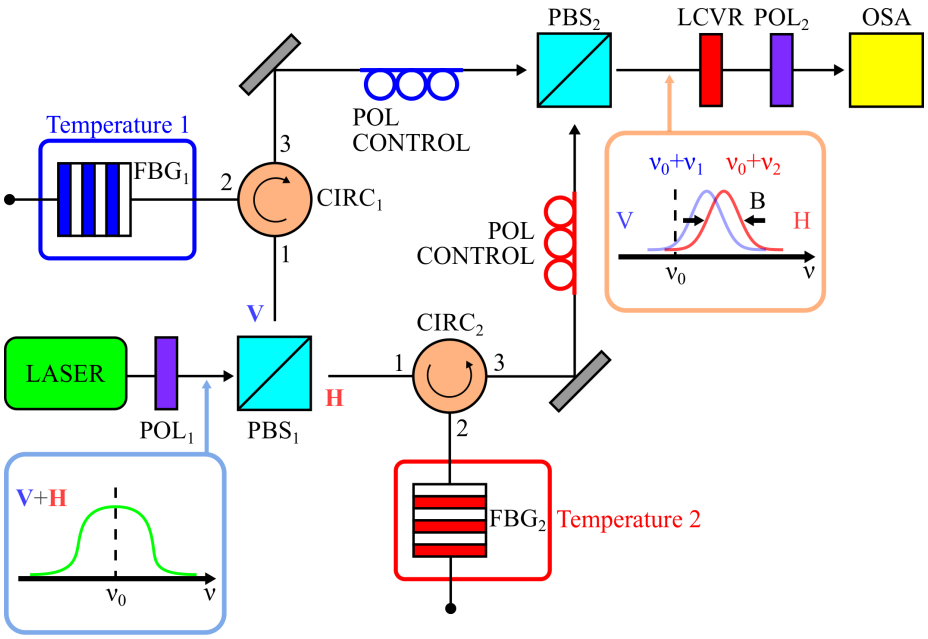


Figure 6.3: Experimental scheme. $FBG_1$ and $FBG_2$: Fiber Bragg Gratings; $POL_1$ and $POL_2$: polarizers; $PBS_1$ and $PBS_2$: polarizing beam splitters; LCVR: Liquid-crystal variable retarder; OSA: Optical Spectrum Analyzer; $CIRC_1$x and $CIRC_2$: optical circulators.

where $\hat{\mathbf{x}}$ and $\hat{\mathbf{y}}$, designate horizontal and vertical polarizations respectively, $\tau$ takes into account the optical path difference present in the experimental setup, $FBG_1$ is centered in $\nu_1$ and $FBG_2$ in $\nu_2$, and $B$ is the bandwidth of the output signal of each FBG, and $\delta = \phi - \Gamma$, where $\phi$ denotes a phase due to the birefringence induced from bends and twists in circulators and single-mode fibers and $\Gamma$ is a phase introduced with a Liquid Crystal Variable Retarder (LCVR) to compensate the unwanted phase $\phi$ [71]. In both cases the shift with respect to the central frequency $\nu_0$ is small compared to the pulse bandwidth (i.e. $B \gg \nu_1 - \nu_0$ or $B \gg \nu_2 - \nu_0$). Inspection of Eq. (6.1) shows clearly the coupling between the shift of the centroid of the spectrum of each pulse, $\nu_1$ and $\nu_2$, and its polarization, a key element of the WVA scheme.

After the weak interaction, the weak value amplification effect is introduced by projecting the recombined signal into a polarization state $\hat{\mathbf{e}}_{\text{out}} = \cos\beta\hat{\mathbf{x}} + \sin\beta\hat{\mathbf{y}}$ with the help of the second polarizer $POL_2$. By making use of the Product Theorem for Gaussian Functions presented in Appendix B to

calculate the power spectrum after post-selection from Eq. (6.1), we obtain

$$\begin{aligned} S_{\text{out}}(\nu) = \frac{S_0}{2}\Bigg\{ & \cos^2\beta \exp\left[-\frac{(\nu-\nu_0-\nu_1)^2}{B^2}\right] \\ & + \sin^2\beta \exp\left[-\frac{(\nu-\nu_0-\nu_2)^2}{B^2}\right] \\ & + \gamma_\nu \sin 2\beta \exp\left[-\frac{(\nu-\nu_0-\nu_+)^2}{B^2}\right] \cos(2\pi\nu\tau+\delta)\Bigg\}, \end{aligned} \tag{6.2}$$

where $\nu_+ = (\nu_1+\nu_2)/2$, and $\gamma_\nu = \exp(-\Delta\nu^2/4B^2)$. After post-selection, the beams reflected from each FBG interfere [72]. As a result, there is a reshaping of the output spectrum. Both FBG can show slightly different spectral responses due to errors in the fabrication process.

We keep one of the FBGs at a constant temperature $T_2$, and measure its reflectivity spectrum to be centered at $\nu_2^0$. The other FBG is used to measure a variable temperature $T_1$, and the centroid of the spectrum of the reflected signal is assumed to change linearly with temperature as

$$\nu_1(T_1) = \nu_1^0 + \kappa(T_1 - T_2)\,. \tag{6.3}$$

The centroid of the spectrum at the output port of the interferometer is obtained after replacing Eq. (6.3) in the expression $\langle\nu\rangle = \int \mathrm{d}\nu\, \nu S(\nu)/\int \mathrm{d}\nu\, S(\nu)$. In the weak coupling regime, the temporal delay $\tau$ in the interferometer is much smaller than the pulse duration $T$, and the frequency shifts $\nu_1(T_1)$ and $\nu_2^0$ are small compared to the bandwidth $B$. In this scenario, the centroid of the spectrum writes

$$\langle\nu\rangle = \nu_0 + \nu_+ + \mathcal{A}\,\nu_- - \mathcal{B}\,, \tag{6.4}$$

where

$$\mathcal{A} = \frac{\cos 2\beta}{1+\gamma_\nu\gamma_\tau \sin 2\beta\, \cos\delta}\,, \tag{6.5}$$

is the amplification factor, $\gamma_\tau = \exp(-\pi\tau^2 B^2)$, $\nu_- = (\nu_1-\nu_2)/2$, and the last term in Eq. (6.4) is given by

$$\mathcal{B} = \frac{\pi\gamma_\nu\gamma_\tau\tau B^2 \sin 2\beta \sin\delta}{1+\gamma_\nu\gamma_\tau \sin 2\beta\, \cos\delta}\,. \tag{6.6}$$

We take as reference for the measurements $\nu_2^0$, which is measured for an angle $\beta = -90°$. One can easily find from Eqs. (6.3) and (6.4) that the shift of the centroid $\langle\Delta\nu\rangle = \langle\nu\rangle - \nu_0 - \nu_2^0$ is

$$\langle\Delta\nu\rangle = \frac{\kappa}{2}(\mathcal{A}+1)(T_1-T_2) + (\mathcal{A}+1)\left(\frac{\nu_1^0-\nu_2^0}{2}\right). \tag{6.7}$$

The shift of the centroid of the spectrum is proportional to the difference in temperature between the FBGs. If we project into a polarization state that selects only the signal coming from the FBG with a variable temperature ($\beta = 0°$), then $\mathcal{A} = 1$ and the constant of proportionality turns out to be $\kappa$, which is determined by the response of the FBG to changing temperatures. However, when we project into different polarization states, $\kappa$ is multiplied by the amplification factor $\mathcal{A}$ that can be much larger than one.

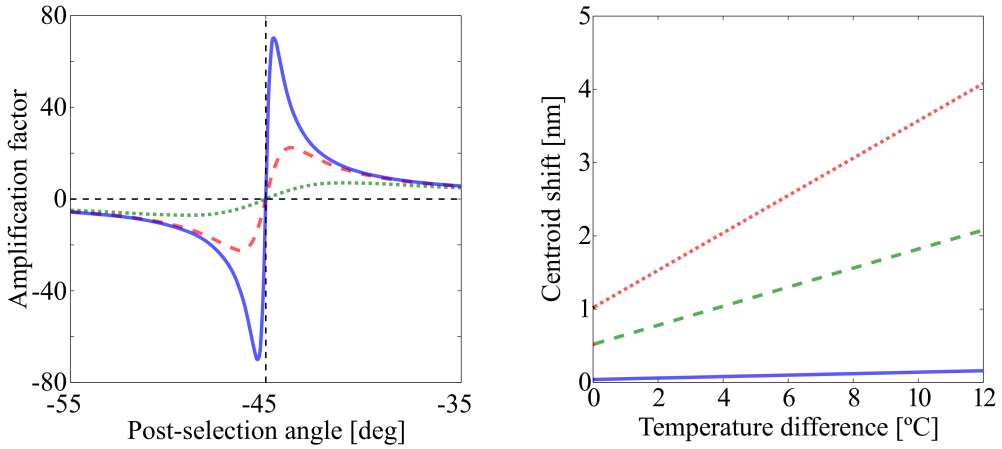


(a) (b)

Figure 6.4: (a) Theoretical amplification factor as a function of the post-selection angle $\beta$ for different values of $\gamma_\nu\gamma_\tau \cos\delta$: 0.9999 (blue continuous line), 0.999 (green dashed-line) and 0.99 (red dotted-line). (b) Theoretical shift of the centroid of the output spectrum as a function of the temperature difference $T_1 - T_2$ for three different post-selection polarizations, and thus amplification factors. $\beta = 0°$ and $\mathcal{A} = 1$ (blue continuous line), $\beta = -42.8°$ and $\mathcal{A} = 25$ (green dashed line), and $\beta = -44.02°$ and $\mathcal{A} = 50$ (red dotted line).

As it can be seen in Eq. (6.5), the closer is the value of the factor $\gamma_\nu\gamma_\tau \cos\delta$ to 1, the larger is the value of the amplification factor. Inspection of Fig. 6.4(a) shows that an amplification factor of up to nearly 80 can be achieved for $\gamma_\nu\gamma_\tau \cos\delta = 0.9999$. Larger values of the amplification factor can indeed be obtained. However, in practice, its maximum value is limited by different experimental factors. On the one hand, it strongly depends on the overlap factor $\Delta/B$ implicit in $\gamma_\nu$, the optical path difference between components of orthogonal polarizations in the weak coupling stage and how

well the phase introduced by the single-mode fibers $\phi$ is compensated by the variable retarder (LCVR).

From Eq. (6.5), we obtain that the maximum amplification factor that can be achieved for an uncompensated phase is

$$\mathcal{A}_{\max} = (1 - \cos^2 \delta)^{-1/2}, \tag{6.8}$$

which is obtained for the post-selection angle $-\pi/4° \pm \beta_{\max} + \frac{1}{2} \arcsin(\cos \delta)$. The largest enhancement is obtained when $\phi = \Gamma$.

On the other hand, in any weak value amplification scenario there is attenuation of the amplitude of the output signal. For low amplification factors, this attenuation can be similarly small. However, a large amplification factor is accompanied by a large attenuation, since the input and post-selected polarization are nearly orthogonal. The amplification factor achievable is thus limited by the Signal-to-Noise ratio available at the detection stage.

Figure 6.4(b) shows the expected shift of the centroid of the spectrum as a function of the temperature difference, for three different output polarization projections that corresponds to three values of the amplification factor. Notice the large enhancement of wavelength shift that can be achieved for a given temperature difference when different output polarization states are selected.

## 6.3 Experimental implementation

Figure 6.5 depicts the experimental scheme implemented. A laser generates pulses with central frequency $\nu_0$ (central wavelength: 1549 nm) that are linearly polarized at +45° by using a half-wave-plate ($HWP_1$) followed by a linear polarizer ($POL_1$). This constitute the pre-selection stage. The laser is a femtosecond fiber laser (Calmar Laser - Mendocino) that generates 320 fs pulses (bandwidth: 11 nm) with a Gaussian-like spectrum, average power 3 mW and repetition rate 20 MHz. The Fiber Bragg Gratings where fabricated in the iTEAM Institute at the Universidad Politècnica de Valencia.

The two orthogonal polarizations ($H$ and $V$) are divided by a polarizing beam splitter ($PBS_1$) and follow different paths. The signal in each path is connected to FBGs ($FBG_1$ and $FBG_2$) by means of circulators ($CIRC_1$ and $CIRC_2$). The signal traversing each arm of the interferometer is focused into a single-mode (SM) fiber that is connected to the first port the circulator. The second port is connected to the FBG that filters out the input signal with an efficiency of 14%, and leaves the FBG with a Gaussian-like

spectrum, 2.5 nm wide Full Width at Half Maximum (FWHM), centered at $\approx 1551$ nm.

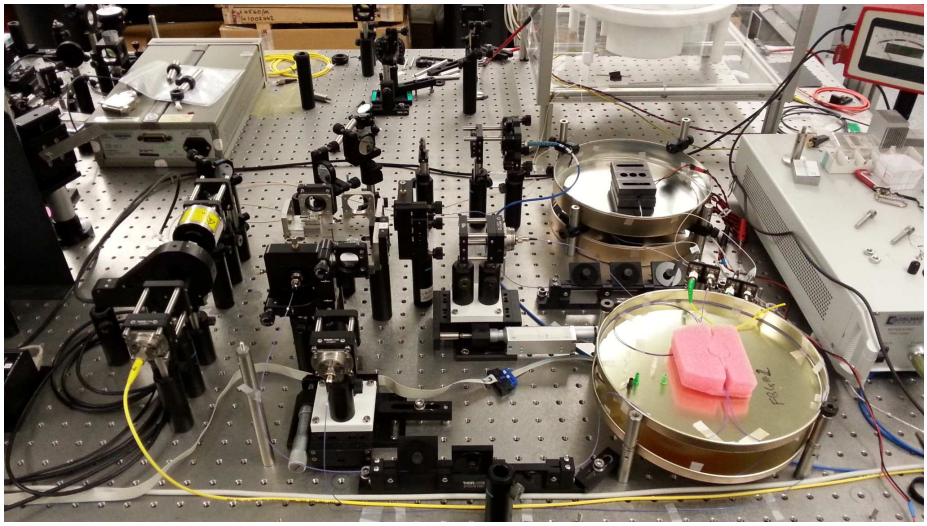

(a)

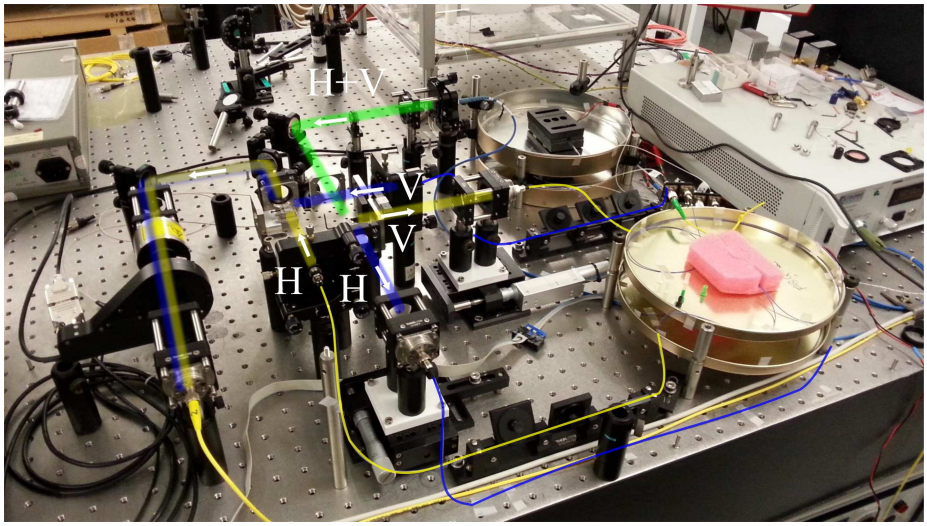


(b)

Figure 6.5: (a). Experimental setup. (b). Optical beam layout. The input beam is indicated by a green line and the output beam is indicated by a blue and yellow beam, with orthogonal polarizations. The input and output beams of circulator 1 (2) are indicated by blue (yellow) lines. Its corresponding polarizations and direction of propagation are also indicated.

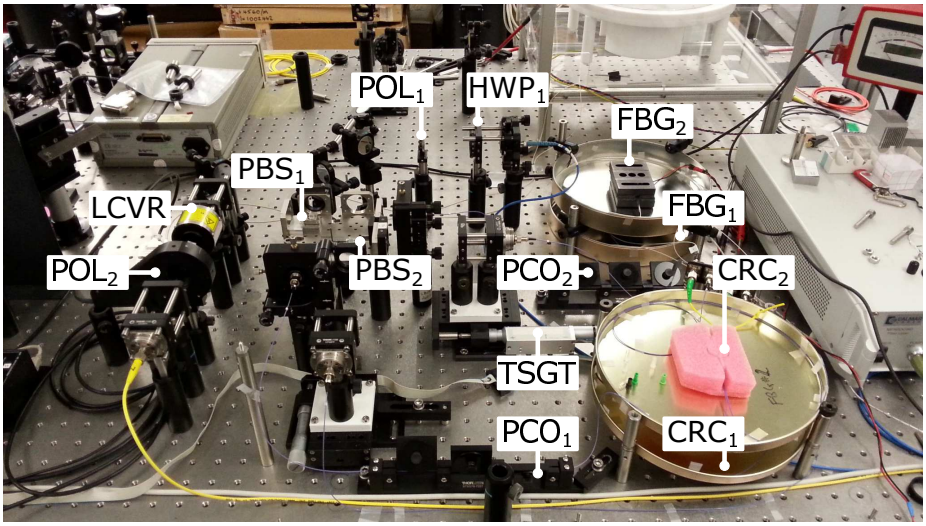


(c)

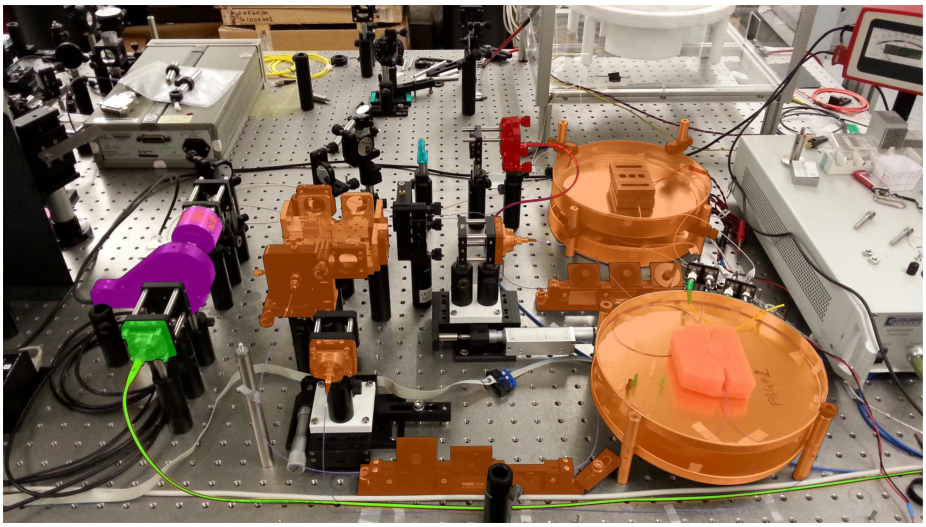

(d)

Figure 6.5: (c). Detail of the components used. HWP: half-wave plate, PBS: polarizing beam splitter, POL: polarizer, PCO: polarization controller, TSTG: translation stage, LCVR: liquid crystal variable retarder. (d). Stages used to: i) select the initial state of polarization (cyan), ii) perform the weak measurement (orange), iii) select the final state of polarization (magenta). The input port and output ports, are colored in red and green respectively.

Each FBG is embedded into an oven that is set to a different temperature, $T_1$ and $T_2$. The FBG acts as a filter whose central frequency is determined by the temperatures of the corresponding oven. If the bandwidth of the input pulse is larger than the bandwidth of the FBG, the effect of a temperature difference is to generate two similar pulses with orthogonal polarizations and different central frequencies. The third port of each circulator is connected to a collimator lens that launches the output beams towards a second PBS ($PBS_2$), that combines the two pulses into a single beam.

Before reaching ($PBS_2$), and due to polarization changes introduced by the circulators and FBGs, the state of polarization of each pulse is rectified after leaving the circulators using polarization controllers ($PCO_1$ and $PCO_2$). In this way, we assure that before recombining again the two pulses in $PBS_2$, the pulse that traversed $FBG_1$ is horizontally polarized and its central frequency is $\nu_1$, whereas the pulse that traversed $FBG_2$ is vertically polarized and is spectrum is centered at $\nu_2$. In all cases, we are interested in detecting small temperature changes, so that the frequency shift $\nu_1 - \nu_2$ is smaller than the FBG bandwidth $B$. To compensate the phase introduced due to birefringence in the circulators and Single-Mode (SM) fibers, a Liquid Crystal Variable Retarder (LCVR) (Thorlabs - LCC1113-C) is added after $PBS_2$.

The output is finally focused on a single-mode fiber connected to an optical spectrum analyzer (Yokogawa - AQ6370). The output spectrum measured is composed of 1000 points in a range of 14 nm around 1551 nm, which corresponds to a resolution of 14 pm. The estimation of the centroid of the signal was done in a time of 2 s, which included acquisition of data, saving and processing. This is in no way a fundamental limit for the measurement time. Faster detection, by reducing the bandwidth, and faster electronic processing can substantially reduce the overall time needed for a measurement.

## 6.4 Experimental results

For the sake of example, Fig. 6.6 shows the spectra of the signals reflected from $FBG_1$ ($\beta = -90°$) and $FBG_2$ ($\beta = 0°$). Figure 6.6(a) corresponds to the signal reflected from $FBG_2$ at a fixed temperature, while Fig. 6.6(b) corresponds to the reflection from $FBG_1$ at different temperatures. The spectrum of the signal reflected from each FBG is composed of a principal lobe $\sim 2.5$ nm wide (FWHM), and a side lobe with smaller amplitude that

appear as a result of the high contrast in index of refraction in the gratings.

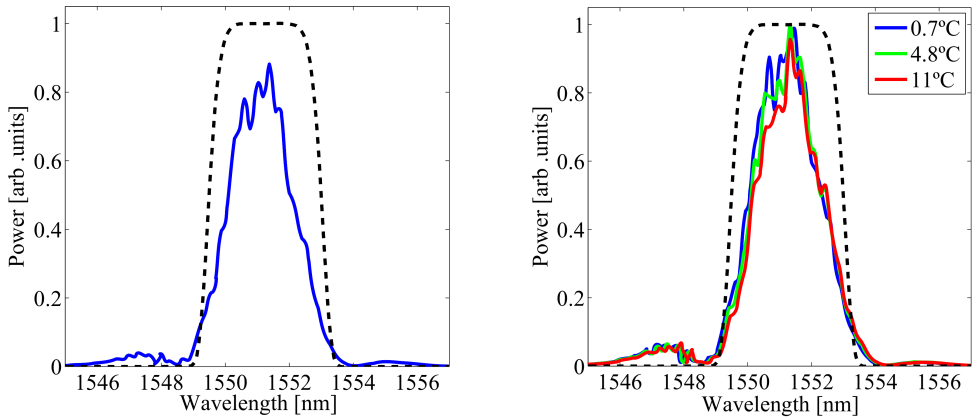


(a) (b)

Figure 6.6: (a) Spectrum of the signal reflected from $FBG_2$ at a fixed temperature ($\beta = -90°$). (b) Spectrum of measured from $FBG_1$ at different temperatures ($\beta = 0°$). Dashed lines: transmission function of the super-Gaussian filter used to get rid of the unwanted side lobes present in the signal.

Figure 6.6(b) also illustrates the difficulties regarding the detection process. Even though the three spectra correspond to a considerably large scan in temperature, ranging from 0.7°C to 11°C, they overlap almost completely and make necessary a detection scheme that can resolve sub-nm displacements in wavelength.

Figure 6.7(a) presents the measured shift of the centroid of the output spectrum for $T_1 - T_2 = 11°$C and different post-selection angles (dots). For small angle deviations around $\beta = -45°$, shifts of the centroid of the spectrum up to $\pm 0.6$ nm are observed. This corresponds to a three-fold enhancement with respect to the initial shift of 0.19 nm given by the FBGs with no weak amplification scheme. The solid line indicates the best theoretical fit obtained using Eq. (6.7). Fig. 6.7(b) shows some selected spectra measured after performing the super-Gaussian filtering. In general, there is a trade-off between the centroid shift observable for a specific temperature difference and the amount of losses that can be tolerated to keep a good SNR.

Since our scheme relies on the measurement of the centroid of a Gaussian-like spectra given a post-selection, the presence of non-negligible side lobes

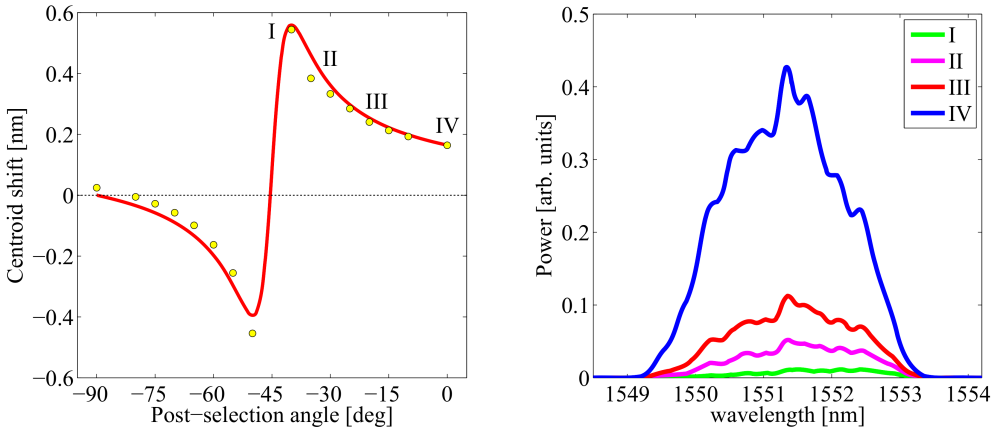


(a) (b)

Figure 6.7: (a) Shift of the centroid of the spectrum for $T_1 - T_2 = 11°C$ and different post-selection angles (dots) in the interval $-90° \leq \beta \leq 0°$. (b) Output spectrum measured for some selected cases: $\beta = -40°$ (I), $\beta = -35°$ (II), $\beta = -25°$ (III) and $\beta = 0°$ (IV).

can alter the measurements. To avoid this effect, each measured spectrum is filtered numerically using a super-Gaussian filter indicated by the dashed line in Fig. 6.6. From the measurements performed, the side lobes become relevant with respect to the main lobe of the output spectrum for post-selection angles within the interval $-50° \leq \beta \leq -40°$. For this reason, a maximum amplification factor of $\approx 4$ is obtained for such angles.

Figure 6.8 is the main result of this chapter. It shows the measured variation of the centroid position of the output spectra as a function of the temperature difference for a given post-selection. Circles indicate the case when the output signal is projected into a polarization state with $\beta = -40°$, so that the output spectrum centroid drifts $\sim 0.035$nm/°C (solid line). For the sake of comparison, asterisks show the case where no weak amplification is used ($\beta = 0°$), generating a spectrum centroid variation of $\sim 0.009$nm/°C (dashed line). The use of the WVA provides a four-fold enhancement of the sensitivity.

The existence of a temperature-dependent group delay between two orthogonal polarizations used to interrogate the FBGs is the key enabling element in WVA. Here we chose to generate the group delay by illuminating two FBGs embedded in a Mach-Zehnder interferometer. Environmental

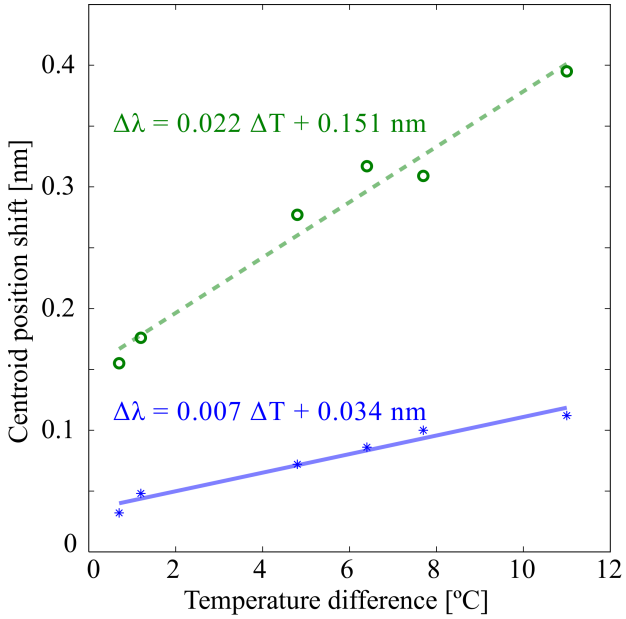


Figure 6.8: Variation of the centroid of the output spectra as a function of the temperature difference for a fixed post-selection angle. The case $\beta = 0°$ (asterisks) illustrates the situation where no WVA scheme is used. The case $\beta = -40°$ (circles) shows the case where the centroid shift is enhanced by a factor of $\approx 4$ by means of the the WVA scheme.

perturbations may affect the measurement, since any measurement based on interferometers requires a precise control. Therefore, in terms of applications, the present scheme is intended for short-range applications like health applications and metrology. However, for an out-of-the-lab implementation of the technique, we are exploring more simple schemes using tailored FBGs that will allow an all-fiber solution to generate two orthogonally-polarized reflected signals with a measurable temperature-dependent delay.

# Conclusions

In this chapter, we have demonstrated that WVA can be used to enhance the sensitivity of sensors based on Fiber Bragg Gratings. Without a WVA scheme, the shift of the spectrum of the signal reflected by a FBG due to temperature changes was measured to be $\sim 0.009\,\mathrm{nm/°C}$. With a weak amplification scheme, we measured a change of $0.035\,\mathrm{nm/°C}$, a fourfold increase.

The proposed scheme is compatible with wavelength division multiplexing (WDM) and time division multiplexing (TDM) being possible to obtain a quasi-distributed measurement. Besides, WVA is compatible with the use of other schemes that enhance the sensitivity of FBGs sensors, such as the use of extrinsic FBG structures. In this way, WVA can multiply the resolution gained with the help of the extrinsic FBG structures.

In scenarios where the measurable shift of the spectrum is limited by the detection stage, but the decrease of signal energy that accompanies still keeps the signal-to-noise ratio at an usable level, weak value amplification is a promising scheme to enhance the capabilities of FBG-based sensor systems.

We should notice that while we consider a temperature sensor, other characteristics as well, such as strain can also be considered as targets. In this respect, the method is general and can be applied to measuring all kinds of physical parameters, provided they could generate a measurable change of the response of FBGs when interrogated by appropriate light beams.

## Main publications by the author related to the contents of this chapter

**L. J. Salazar-Serrano**, D. Barrera, W. Amaya, S. Sales, V. Pruneri, J. Capmany, and J. P. Torres, "Enhancement of the sensitivity of a temperature sensor based on fiber Bragg gratings via weak value amplification", Optics Letters **40**, 3962 (2015).

CHAPTER

# SEVEN

# THE TRUE USEFULNESS OF WEAK VALUE AMPLIFICATION: WHAT WE CAN DO AND WHAT WE CANNOT

> *In theory, there is no difference between theory and practice. But, in practice, there is.*
>
> Jan L. A. van de Snepscheut , *1984*

Weak Value Amplification (WVA) [2] is a concept that has been extensively used in a myriad of applications with the aim of rendering measurable tiny changes of a variable of interest. In spite of this, there is still an ongoing debate about its *true* nature and whether is really needed for achieving high sensitivity. Here we aim at helping to clarify the puzzle, using a specific example and some basic concepts from quantum estimation theory, highlighting what the use of the WVA concept can offer and what it can not. While WVA cannot be used to go beyond some fundamental sensitivity limits that arise from considering the full nature of the quantum states, WVA can notwithstanding enhance the sensitivity of *real and specific* detection schemes that are limited by many other things apart from the quantum nature of the states involved, i.e. *technical noise*. Importantly, it can do that in a straightforward and easily accessible manner.

As shown in the previous chapters with numerous examples, the WVA concept has been used under a great variety of experimental conditions to reveal tiny changes of a variable of interest. In all the cases presented, a

priori sensitivity limits were not due to the quantum nature of the light used (*photon statistics*), but instead to the insufficient resolution of the detection system, what might be termed generally as *technical noise*. WVA was a feasible choice to go beyond this limitation. In spite of this extensive evidence, "its interpretation has historically been a subject of confusion" [38]. For instance, while some authors [39] show that "weak-value-amplification techniques (which only use a small fraction of the photons) compare favorably with standard techniques (which use all of them)", others [73] claim that WVA "does not offer any fundamental metrological advantage", or that WVA [74] "does not perform better than standard statistical techniques for the tasks of single parameter estimation and signal detection". However, these conclusions are criticized by some authors based on the idea that "the assumptions in their statistical analysis are irrelevant for realistic experimental situations" [75]. This can explain why recently some papers have appeared [39, 76] with the aim at *re-evaluating and re-considering* in a more general context what WVA can offer for metrology.

In this chapter we analyze from a new perspective, in terms of the concept of quantum trace distance, and by means of a particular example, but representative of a wide class of WVA experimental implementations, the pros and cons of using WVA, quantifying how much can be gained under appropriate circumstances. In other words, we will see, with an approach centered on how different quantum states are distinguished in specific experimental implementations, why some authors can say that WVA offers no advantage in metrology. At the same time we will put numbers to the idea that WVA can be *judged 'handy'* [76] in certain cases.

The approach used here is slightly different from what other analysis of WVA do, where most of the times the tool used to estimate its usefulness is the Fisher information and the related Cramér-Rao bound. The Fisher information requires to know the probability distribution of possible experimental outcomes for a given value of the variable of interest. Therefore, it can look for sensitivity bounds for measurements by including *technical characteristics* of specific detection schemes [39]. Therefore we offer a very basic and physical understanding of how WVA works, based on the idea of how WVA schemes transform very close quantum states.

The chapter is organized as follows. In Section 7.1 we consider the question of what is the real usefulness of detection schemes based on WVA by means of a representative example. From these results, in Section 7.2, we discuss the advantages and disadvantages of using WVA in terms of the concept of trace distance. Subsequently, we compare our results with respect

to other approaches based on the evaluation of the Fisher information and the related Cramér-Rao bound. In the last section, some final remarks are made.

## 7.1 WVA: What is its real *value*?

There are two sides to consider when analyzing in which sense WVA can be useful. On the one hand, WVA measures specific information of a quantum state state obtained after transformations that in most cases make use of unitary operations. Therefore, it cannot modify the statistics of photons involved. Basic quantum estimation theory states that the post-selection of an appropriate output state obtained after unitary transformations, the basic element where WVA is embedded, cannot be better than the use of the input state [77]. Moreover, WVA uses some selected, useful but partial, information about the quantum state that cannot be better that considering the full state. Indeed, due to the unitarian nature of the operations involved in the overall transformation where WVA is embedded, it should be equally good any transformation of the input state than performing no transformation at all. In other words, when considering only the quantum nature of the light used, WVA cannot be expected to enhance the precision of measurements [78].

On the other hand, a more general analysis that goes beyond only considering the quantum nature of the light, shows that WVA can be useful when certain technical limitations are considered (for instance, consider the examples presented in references [39, 75]). In this sense, it might increase the ultimate resolution of the detection system by effectively lowering the value of the smallest quantity that can detected. In most scenarios, although not always [11], the signal detected is severely depleted, due to the quasi-orthogonality of the input and output states selected. However, in many applications, limitations are not related to the low intensity of the signal [3], but to the smallest change that the detector can measure irrespectively of the intensity level of the signal.

### 7.1.1 An example of the use of the weak value amplification concept: measuring small temporal delays with large bandwidth pulses

Measuring tiny quantities is essentially equivalent to distinguishing between nearly parallel quantum states. The concept of trace distance provides a clear and direct measure of the degree of distinguishability of two quantum states. Indeed, the trace distance gives us the minimum probability of error of distinguishing two quantum states that can be achieved under the best detection system one can imagine [1].

For the sake of example, consider the weak amplification scheme [28] depicted in Fig. 7.1 that aims at measuring very small temporal delays $\tau$, or correspondingly tiny phase changes [29], with the help of optical pulses of much larger duration. The scheme has been recently demonstrated experimentally [15, 30] and is described in more detail in chapter 4. We consider this specific case because it contains the main ingredients of a typical WVA scheme and it allows to derive analytical expressions of all quantities involved, which facilitates the analysis of main results. Moreover, the scheme makes use of linear optics elements only and also works with large-bandwidth partially-coherent light [32]. More importantly, even though the scheme is aimed at measuring ultra-small temporal delays, it is representative of a long list of *fundamentally equivalent* WVA schemes. The use of a specific experimental configuration where WVA has demonstrated its *practical* utility in the lab, providing an enhancement in sensitivity, can help to identify more clearly the role of important concepts of our discussion such as quantum distance or technical noise. However, some of our conclusions might not apply to all WVA schemes without further consideration.

As mentioned in chapter 2, a WVA scheme requires three main ingredients: (i) the consideration of two subsystems (here two degrees of freedom: the polarization and the spectrum of an optical pulse) that are weakly coupled (here we make use of a polarization-dependent temporal delay that is introduced with the help of a Michelson interferometer); (ii) the *pre-selection* of the input state of both subsystems; and (iii) the *post-selection* of the state in one of the subsystems (the state of polarization) and the measurement of the state of the remaining subsystem (the spectrum of the pulse). With appropriate *pre-* and *post-selection* of the polarization of the output light, tiny changes of the temporal delay $\tau$ can cause anomalously large changes of its spectrum, rendering in principle detectable very small temporal delays.

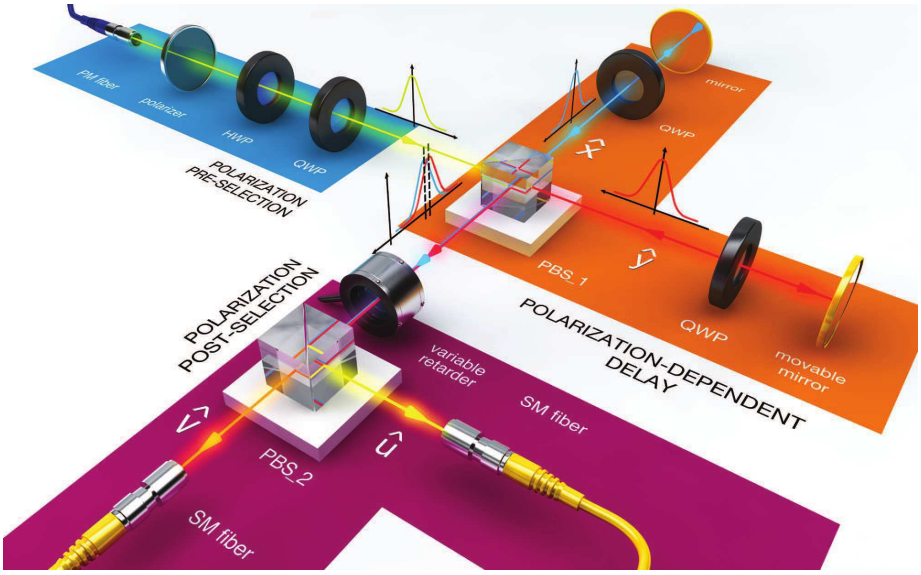


Figure 7.1: Weak value amplification scheme aimed at detecting extremely small temporal delays. The input pulse polarization state is selected to be left-circular by using a polarizer, a quarter-wave plate (QWP) and a half-wave plate (HWP). A first polarizing beam splitter ($PBS_1$) splits the input into two orthogonal linear polarizations that propagate along different arms of the interferometer. An additional QWP is introduced in each arm so that after traversing the QWP twice, before and after reflection in the mirrors, the beam polarization is rotated by 90° to allow the recombination of both beams, delayed by a temporal delay $\tau$, in a single beam by the same PBS. After $PBS_1$, the output polarization state is selected with a liquid crystal variable retarder (LCVR) followed by a second polarizing beam splitter ($PBS_2$). The variable retarder is used to set the parameter $\theta$ experimentally. Finally, the spectrum of each output beam is measured using an optical spectrum analyzer (OSA). ($\hat{\mathbf{x}}$,$\hat{\mathbf{y}}$) and ($\hat{\mathbf{u}}$,$\hat{\mathbf{v}}$) correspond to two sets of orthogonal polarizations.

Let us be more specific about how all these ingredients are realized in the scheme depicted in Fig. 7.1. Notice that parts of what it follows might have been already commented in Chapter 4, however we include them also here for the sake of convenience, for making the discussion as simple to follow as possible. An input coherent laser beam (mean number of photons, $N$) shows circular polarization, $\hat{\mathbf{e}}_{\mathrm{i}} = (\hat{\mathbf{x}} - i\hat{\mathbf{y}})/\sqrt{2}$, and a Gaussian shape with temporal width $T_0$ (Full-width-half maximum, $\tau \ll T_0$). The normalized

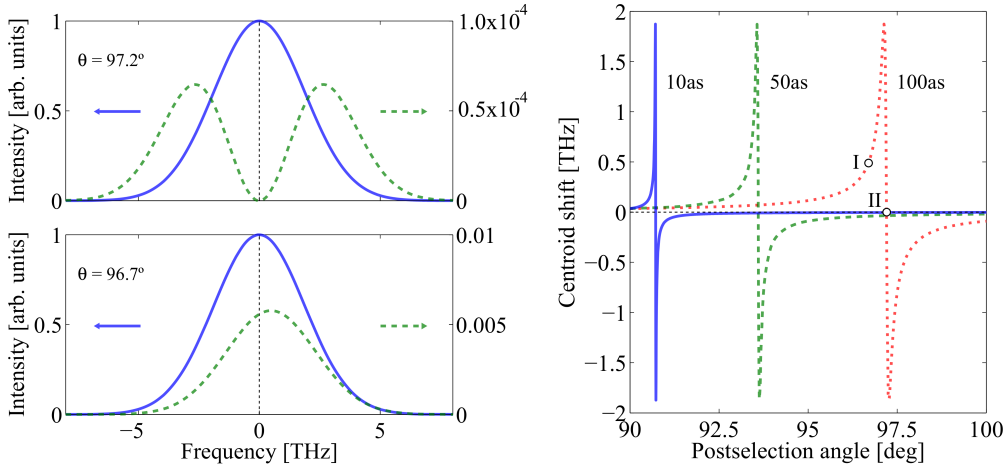


(a) (b)

Figure 7.2: Spectrum of $\Phi_u(\Omega)$ measured at the corresponding output port of $PBS_2$. (a) Spectral shape of the mode functions for $\tau = 0$ (solid blue line) and $\tau = 100$ as (dashed green line). In the upper panel, the post-selection angle $\theta$ is 97.2°, so as to fulfill the condition $\omega_0\tau - \Gamma = \pi$. In the lower panel, the angle $\theta$ is 96.7°. (b) Shift of the centroid of the spectrum of the output pulse after projection into the polarization state $\hat{\mathbf{u}}$ in $PBS_2$, as a function of the post-selection angle $\theta$. Green solid line: $\tau = 10$ as; Dotted red line: $\tau = 50$ as, and dashed blue line: $\tau = 100$ as. Label **I** corresponds to $\theta = 96.7°$ (mode for $\tau = 100$ as shown in the lower panel of (a)). Label **II** corresponds to $\theta = 97.2°$, where the condition $\omega_0\tau - \Gamma = \pi$ is fulfilled (mode for $\tau = 100$ as shown in the upper panel of (a)). It yields the minimum mode overlap between states with $\tau = 0$ and $\tau \neq 0$. Data: $\lambda_0 = 1.5\,\mu$m and $T_0 = 100$ fs.

temporal and spectral shapes of the pulse read

$$\Psi(t) = \left(\frac{4\ln 2}{\pi T_0^2}\right)^{1/4} \exp\left(-\frac{2\ln 2}{T_0^2}\, t^2\right), \tag{7.1}$$

$$\Phi(\Omega) = \left(\frac{T_0^2}{4\pi\ln 2}\right)^{1/4} \exp\left(-\frac{T_0^2}{8\ln 2}\, \Omega^2\right), \tag{7.2}$$

where $t$ is time, $\Omega$ is the angular frequency deviation from the central angular frequency $\omega_0$ and $\Phi(\Omega) = (2\pi)^{-1/2} \int \mathrm{d}t\, \Psi(t) \exp(i\Omega t)$. The input beam is divided into the two arms of a Michelson interferometer with the help of a polarizing beam splitter ($PBS_1$). Light beams with orthogonal polarizations traversing each arm of the interferometer are delayed $\tau_0$ and $\tau_0 + \tau$,

respectively, which constitute the weak coupling between the two degrees of freedom. After recombination of the two orthogonal signals in the same $PBS_1$, the combination of a liquid-crystal variable retarder (LCVR) and a second polarizing beam splitter ($PBS_2$) performs the post-selection of the polarization of the output state, projecting the incoming signal into the polarization states $\hat{\mathbf{u}} = (\hat{\mathbf{x}} + \exp(i\theta)\hat{\mathbf{y}})/\sqrt{2}$ and $\hat{\mathbf{v}} = (\hat{\mathbf{x}} - \exp(i\theta)\hat{\mathbf{y}})/\sqrt{2}$. The spectral shape of the signals in the two output ports write (not normalized)

$$\Phi_u(\Omega) = \frac{\Phi(\Omega)}{2} \exp\left[i(\omega_0 + \Omega)\tau_0\right] \left\{1 + \exp\left[i(\omega_0 + \Omega)\tau - i\Gamma\right]\right\} \quad (7.3)$$

$$\Phi_v(\Omega) = \frac{\Phi(\Omega)}{2} \exp\left[i\left(\omega_0 + \Omega\right)\tau_0\right] \left\{1 - \exp\left[i(\omega_0 + \Omega)\tau - i\Gamma\right]\right\} , \quad (7.4)$$

where $\tau_0$ and $\tau_0 + \tau$ are the delays and $\Gamma = \pi/2 + \theta$.

After the signal projection performed after $PBS_2$, the WVA scheme distinguishes different states, corresponding to different values of the temporal delay $\tau$, by measuring the spectrum of the outgoing signal in the selected output port. The different spectra obtained for delays $\tau = 0$ and $\tau = 100$ as, for two different polarization projections, are shown in Fig. 7.2(a) and Fig. 7.2(b). To characterize different modes one can measure the centroid shift of the spectrum of the signal in one output port as a function of the delay $\tau$. If we consider the signal $\Phi_u(\Omega)$, the shift of the centroid is given by $\Delta f = (2\pi)^{-1} \int \mathrm{d}\Omega\, \Omega\, |\Phi_u(\Omega)|^2 / \int \mathrm{d}\Omega\, |\Phi_u(\Omega)|^2$. Fig. 7.2(b) shows the centroid shift of the output signal $\Phi_u(\Omega)$ for $\tau \neq 0$, which reads

$$\Delta f = -\frac{\tau \ln 2}{\pi T_0^2} \frac{\gamma \sin\left(\omega_0\tau - \Gamma\right)}{1 + \gamma \cos\left(\omega_0\tau - \Gamma\right)} , \quad (7.5)$$

where

$$\gamma = \exp\left(-\ln 2 \, \frac{\tau^2}{T_0^2}\right) . \quad (7.6)$$

The differential power between both signals (with $\tau = 0$ and $\tau \neq 0$) reads

$$\frac{P_{\mathrm{out}}(\tau) - P_{\mathrm{out}}(\tau = 0)}{P_{\mathrm{i}}} = \frac{1}{2} \left[\cos\Gamma - \cos\left(\omega_0\tau - \Gamma\right)\right] . \quad (7.7)$$

When there is no polarization-dependent time delay ($\tau = 0$), the centroid of the spectrum of the output signal is the same than the centroid of the input laser beam, i.e., there is no shift of the centroid ($\Delta f = 0$). However, the presence of a small $\tau$ can produce a large and measurable shift of the centroid of the spectrum of the signal.

### 7.1.2 View of WVA from quantum estimation theory

Detecting the presence ($\tau \neq 0$) or absence ($\tau = 0$) of a temporal delay between the two coherent orthogonally-polarized beams after recombination in $\mathrm{PBS}_1$, but before traversing $\mathrm{PBS}_2$, is equivalent to detecting which of the two quantum states,

$$|\Phi_0\rangle = |\Phi_{\tau_0}(\Omega)\rangle_x |\Phi_{\tau_0}(\Omega)\rangle_y \,, \tag{7.8}$$

or

$$|\Phi_1\rangle = |\Phi_{\tau_0}(\Omega)\rangle_x |\Phi_{\tau_0+\tau}(\Omega)\rangle_y \,, \tag{7.9}$$

is the output quantum state which describes the coherent pulse leaving $\mathrm{PBS}_1$. $(x, y)$ designates the corresponding polarizations. The spectral shape (mode function) $\Phi$ writes

$$\Phi_{\tau_0+\tau}(\Omega) = \Phi(\Omega) \exp\left[i(\omega_0 + \Omega)(\tau_0 + \tau)\right] \,, \tag{7.10}$$

where $\Phi(\Omega)$ is the spectral shape of the input coherent laser signal.

The minimum probability of error that can be made when distinguishing between two quantum states is related to the trace distance between the states [79]. For two pure states, $\Phi_0$ and $\Phi_1$, the (minimum) probability of error is [1, 80, 81]

$$P_{\text{error}} = \frac{1}{2}\left(1 - \sqrt{1 - |\langle\Phi_0|\Phi_1\rangle|^2}\right) \,. \tag{7.11}$$

For $\Phi_0 = \Phi_1$, $P_{\text{error}} = 0.5$. On the contrary, to be successful in distinguishing two quantum states with low probability of error ($P_{\text{error}} \sim 0$) requires $|\langle\Phi_0|\Phi_1\rangle| \sim 0$, i.e., the two states should be close to orthogonal.

The coherent broadband states considered here can be generally described as single-mode quantum states where the mode is the corresponding spectral shape of the light pulse. Let us consider two single-mode coherent beams

$$\begin{aligned} |\alpha\rangle &= \exp\left(-\frac{|\alpha|^2}{2}\right) \sum_{n=0}^{\infty} \frac{\alpha^n \left(A^\dagger\right)^n}{n!} |0\rangle \,, \\ |\beta\rangle &= \exp\left(-\frac{|\beta|^2}{2}\right) \sum_{n=0}^{\infty} \frac{\beta^n \left(B^\dagger\right)^n}{n!} |0\rangle \,, \end{aligned} \tag{7.12}$$

where $A$ and $B$ are the two modes

$$\begin{aligned} A^\dagger &= \int d\Omega F(\Omega) a^\dagger(\Omega) \,, \\ B^\dagger &= \int d\Omega G(\Omega) a^\dagger(\Omega) \,, \end{aligned} \tag{7.13}$$

and $|\alpha|^2$ and $|\beta|^2$ are the mean number of photons in modes $A$ and $B$, respectively. The mode functions $F$ and $G$ are assumed to be normalized, i.e., $\int d\Omega |F(\Omega)|^2 = \int d\Omega |G(\Omega)|^2 = 1$. The overlap between the quantum states, $|\langle\beta|\alpha\rangle|^2$, reads

$$|\langle\beta|\alpha\rangle|^2 = \exp\left(-|\alpha|^2 - |\beta|^2 + \rho\alpha\beta^* + \rho^*\alpha^*\beta\right) , \tag{7.14}$$

where we introduce the mode overlap $\rho$ that reads

$$\rho = \int d\Omega F(\Omega) \left[G(\Omega)\right]^* . \tag{7.15}$$

In order to obtain Eq. (7.14) we have made use of $\langle 0|B^n \left[A^\dagger\right]^m |0\rangle = n!\rho^n \delta_{nm}$. For $\rho = 1$ (coherent beams in the same mode but with possibly different mean photon numbers) we recover the well-known formula for single-mode coherent beams [82]: $|\langle\beta|\alpha\rangle|^2 = \exp\left(-|\alpha - \beta|^2\right)$. Making use of Eqs. (7.9), (7.14) and (7.15) we obtain

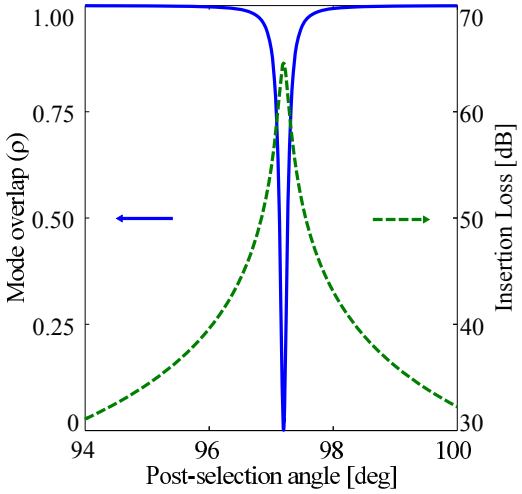


Figure 7.3: Mode overlap and insertion loss as a function of the post-selection angle. Mode overlap $\rho$ of the mode functions corresponding to the quantum states with $\tau = 0$ and $\tau = 100$ as, as a function of the post-selection angle $\theta$ (solid blue line). The insertion loss, given by $10\log_{10}\, P_{\rm out}/P_{\rm i}$ is indicated by the dotted green line. The minimum mode overlap, and maximum insertion loss, corresponds to the post-selection angle $\theta$ that fulfills the condition $\omega_0\tau - \Gamma = \pi$, which corresponds to $\theta = 97.2°$. Data: $\lambda_0 = 1.5\,\mu$m, $T_0 = 100$ fs.

$$\begin{aligned} |\langle\Phi_0|\Phi_1\rangle|^2 &= |\langle\Phi(\tau_0)|\Phi(\tau_0)\rangle_x|^2 |\langle\Phi(\tau_0)|\Phi(\tau_0+\tau)\rangle_y|^2 \\ &= \exp\left[-N\left(1 - \gamma\cos\omega_0\tau\right)\right] , \end{aligned} \tag{7.16}$$

In the WVA scheme considered here, the signal after $\mathrm{PBS}_2$ is projected into the orthogonal polarization states $\hat{\mathbf{u}}$ and $\hat{\mathbf{v}}$, and as a result the signals in both output ports are given by Eqs. (7.3) and (7.4). Making use of Eqs. (7.3), (7.4) and (7.15) we obtains that the mode overlap (for $\Phi_u$) reads

$$\begin{aligned}\rho &= \frac{1+\cos\Gamma+\gamma\cos\omega_0\tau+\gamma\cos(\omega_0\tau-\Gamma)}{2\left[1+\cos\Gamma\right]^{1/2}\left[1+\gamma\cos(\omega_0\tau-\Gamma)\right]^{1/2}} \\ &- \frac{i\left[\sin\Gamma+\gamma\sin\omega_0\tau+\gamma\sin(\omega_0\tau-\Gamma)\right]}{2\left[1+\cos\Gamma\right]^{1/2}\left[1+\gamma\cos(\omega_0\tau-\Gamma)\right]^{1/2}}\,, \end{aligned} \tag{7.17}$$

For $\tau=0$, and therefore $\gamma=1$, we obtain $\rho=1$. Fig. 7.3 shows the mode overlap of the signal in the corresponding output port for a delay of $\tau=100$ as. The mode overlap has a minimum for $\omega_0\tau-\Gamma=\pi$, where the two mode functions becomes easily distinguishable, as shown in Fig. 7.2. The effect of the polarization projection, a key ingredient of the WVA scheme, can be understood as a change of the mode overlap (*mode distinguishability*) between states with different delay $\tau$.

However, an enhanced mode distinguishability in this output port is accompanied by a corresponding increase of the insertion loss, as it can be seen in Fig. 7.3. The insertion loss, $P_{\mathrm{out}}(\tau)/P_{\mathrm{i}}=1/2\,\left[1+\gamma\cos(\omega_0\tau-\Gamma)\right]$, is the largest when the modes are close to orthogonal ($\rho\sim 0$). The quantum overlap between the states reads

$$\begin{aligned}|\langle\Phi_u(\tau_0)|\Phi_u(\tau_0+\tau)\rangle|^2 &= |\langle\Phi_v(\tau_0)|\Phi_v(\tau_0+\tau)\rangle|^2 \\ &= \exp\left[-\frac{N}{2}\left(1-\gamma\cos\omega_0\tau\right)\right]\,, \end{aligned} \tag{7.18}$$

so

$$\begin{aligned}|\langle\Phi_0|\Phi_1\rangle|^2 &= |\langle\Phi_u(\tau_0)|\Phi_u(\tau_0+\tau)\rangle_u|^2|\langle\Phi_v(\tau_0)|\Phi_v(\tau_0+\tau)\rangle_v|^2 \\ &= \exp\left[-N\left(1-\gamma\cos\omega_0\tau\right)\right]\,, \end{aligned} \tag{7.19}$$

which is the same result (see Eq. (7.16)) obtained for the signal after $\mathrm{PBS}_1$, but before $\mathrm{PBS}_2$. Both effects indeed compensate, as it should be, since the trace distance between quantum states is preserved under unitary transformations.

We can also see the previous results from a slightly different perspective making use of quantum estimation theory (see chapter 4 in [1]). The WVA scheme considered throughout can be thought as a way of estimating the value of the single parameter $\tau$ with the help of a light pulse in a coherent

state $|\alpha\rangle$. Since the quantum state is pure, the lower bound to the variance of an unbiased estimate of the parameter $\tau$ variance reads

$$\mathrm{Var}\,(\hat{\tau}) \geq \frac{1}{4}\left[\langle\frac{\partial\alpha}{\partial\tau}|\frac{\partial\alpha}{\partial\tau}\rangle - \left|\langle\alpha|\frac{\partial\alpha}{\partial\tau}\rangle\right|^2\right]^{-1}. \tag{7.20}$$

For a coherent product state of the form $|\alpha\rangle = \prod_i |\alpha_i\rangle$, where the index $i$ refers to different frequency modes, we obtain that $Q = \sum_i Q_i$, where $Q = \langle\partial\alpha/\partial\tau|\partial\alpha/\partial\tau\rangle - |\langle\alpha|\partial\alpha/\partial\tau\rangle|^2$ and $Q_i = \langle\partial\alpha_i/\partial\tau|\partial\alpha_i/\partial\tau\rangle - |\langle\alpha_i|\partial\alpha_i/\partial\tau\rangle|^2$. If $\alpha_i = \beta_i \exp(i\varphi_i)$, where $|\beta_i|^2$ is the mean number of photons in frequency mode $i$ and only $\varphi_i$ depends on the parameter $\tau$ as $\varphi_i = (\omega_0+\Omega_i)\tau$, we obtain that $|\partial\alpha_i/\partial\tau\rangle = i\,(\partial\varphi_i/\partial\tau)\,\alpha_i a_i^\dagger|\alpha_i\rangle$, where $a_i^\dagger$ is the creation operator of the corresponding frequency mode. Making use of Eq. (7.9), we obtains that here the lower bound reads

$$\mathrm{Var}\,(\hat{\tau}) \geq \frac{1}{2N\,(\omega_0^2 + B^2)}\,, \tag{7.21}$$

where $B = \sqrt{2\ln 2}/T_0$ is the rms bandwidth in angular frequency of the pulse. In all cases of interest $B \ll \omega_0$. This limit is a fundamental limit that set a bound to the minimum variance that any measurement can achieve. It is unchanged by unitary transformations and only depends on the quantum state considered.

Inspection of Eqs. (7.16) and (7.19) seems to indicate that a measurement after projection in any basis, the core element where it is embedded the weak amplification scheme, provides no fundamental advantage in metrology. The fact that there might be no fundamental advantage in quantum noise limited measurements for WVA, under certain general conditions, has been pointed out previously [83], even though they also stated that alternative assumptions can also change its conclusions. Moreover, it is important to notice that this *lack of enhancement of sensitivity* is related to the fact that alternative schemes to WVA that use other characteristics of the quantum state at hand can offer better sensitivity (for instance, see an example in [84]). Notice that the result obtained implies that the only relevant factor limiting the sensitivity of detection is the quantum nature of the light used (a *coherent state* in our case). We are implicitly assuming that a) we have full access to all relevant characteristics of the output signals; and b) detectors are ideal, and can detect any change, as small as it might be, if enough signal power is used. If this is the case, weak value amplification provides no enhancement of the sensitivity.

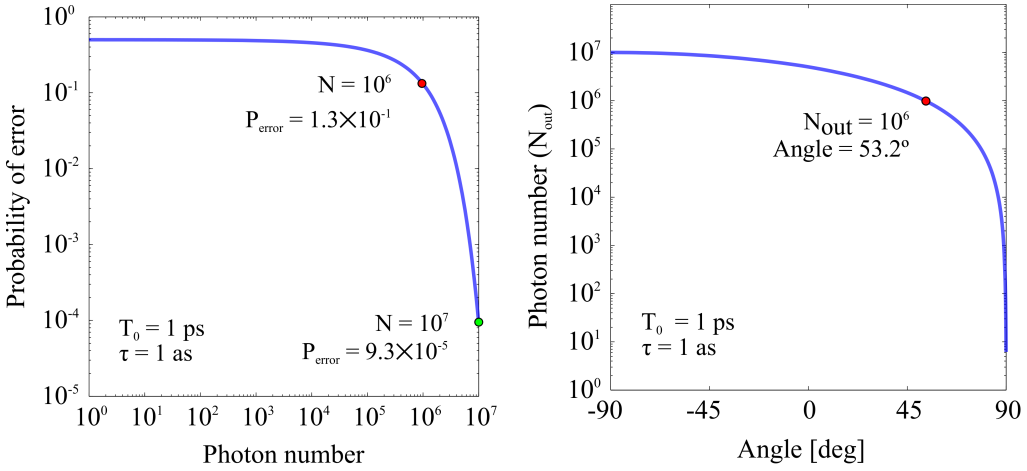


Figure 7.4: Reduction of the probability of error using a weak value amplification scheme. (a) Minimum probability of error as a function of the photon number $N$ that enters the interferometer. The two points highlighted corresponds to $N = 10^6$, which yields $P_{\text{error}} = 1.3 \times 10^{-1}$, and $N = 10^7$, which yields $P_{\text{error}} = 9.3 \times 10^{-5}$. (b) Number of photons ($N_{\text{out}}$) after projection in the polarization state $\hat{\mathbf{u}} = (\hat{\mathbf{x}} + \hat{\mathbf{y}} \exp(i\theta))/\sqrt{2}$, as a function of the angle $\theta$. The input number of photons is $N = 10^7$. The dot corresponds to the point $N_{\text{out}} = 10^6$ and $\theta = 53.2°$. Pulse width: $T_0$=1 ps; temporal delay: $\tau$= 1 as.

However, these assumptions can be far from truth in many realistic experimental situations. In the laboratory, the quantum nature of light is an important factor, but not the only one, limiting the capacity to measure tiny changes of variables of interest. On the one hand, most of the times we detect only certain characteristic of the output signals, probably the most relevant, but this is still partial information about the quantum state. On the other hand, detectors are not ideal and noteworthy limitations to its performance can appear. To name a few, they might no longer work properly above a certain photon number input, electronics and signal processing of data can limit the resolution beyond what is allowed by the specific quantum nature of light, conditions in the laboratory can change randomly effectively reducing the sensitivity achievable in the experiment. Surely, all of these are *technical* rather than *fundamental* limitations, but in many situations the ultimate limit might be *technical* rather than *fundamental*. In this scenario, we show below that weak value amplification can be a *valuable* and an *easy* option to overcome all of these technical limitations, as it has been

demonstrated in numerous experiments.

## 7.2 Advantages of using WVA

The question if WVA can be turned useful for metrology applications when considering that the amount of data is finite has been at the center of the discussion about the *true utility* of WVA schemes. In [83] they noticed that their conclusions might not hold in this case, while in [74] they claim that WVA is sub-optimal for any amount of data. The advantage of using WVA under the restriction of finite data is pointed out by [75] as one of its main characteristics, and its technical advantages are also discussed in [39]. Here we quantify, making use of the concept of trace distance, how much can be gained using WVA in the implementation of WVA considered versus not using any projection at all. Again, it is important to notice that we are comparing two approaches (projection vs not projection) for a certain measurement that refers to partial information available about the quantum states. Therefore our results might not contradict claims about the existence, maybe in principle, of other experimental approaches that can equal, or even improve, what WVA can achieve.

### 7.2.1 Detection limited by photon number

Let us suppose that we have at hand light detectors that cannot be used with more than $N_0$ photons. Fig. 7.4(a) shows the minimum probability of error as a function of the number of photons ($N$) entering the interferometer. For $N = N_0 = 10^6$, inspection of the figure shows that the probability of error is $P_{\text{error}} = 1.3 \times 10^{-1}$. This is the best we can do with this experimental scheme and these particular detectors without resorting to weak value amplification.

However, if we project the output signal from the interferometer into a specific polarization state, and increase the flux of photons, we can decrease the probability of error, without necessarily going to a regime of high depletion of the signal [11]. For instance, with $\theta = 53.2°$, and a flux of photons of $N = 10^7$, so that after projection $N_{\text{out}} = N_0 = 10^6$ photons reach the detector, the probability of error is decreased to $P_{\text{error}} = 9.3 \times 10^{-5}$, effectively enhancing the sensitivity of the experimental scheme (see Fig. 7.4(b)). The probability of error can be further decreased, also for other projections, at the expense of further increasing the input signal $N$.

In general, the overlap between the states, independent of any projection,

is

$$|\langle\Phi_0|\Phi_1\rangle|^2 = \exp\left[-N\left(1-\gamma\cos\omega_0\tau\right)\right] , \tag{7.22}$$

where $N$ is the number of input photons. If the detectors cannot handle more than $N_0$ photons, without a WVA scheme the input signal is limited by $N < N_0$ , so that the minimum overlap achievable is

$$|\langle\Phi_0|\Phi_1\rangle|^2 = \exp\left[-N_0\left(1-\gamma\cos\omega_0\tau\right)\right] , \tag{7.23}$$

that sets a lower bound to the minimum probability of error that can be achieved in this type of measurements.

Notwithstanding, by making use of a WVA scheme, we can select a post-selection angle $\Gamma$ and increase the input photon flux so that $N_0$ photons reach the detector. In this case we need to enhance the input number of photons to be

$$N = \frac{2N_0}{1+\gamma\cos(\omega_0\tau-\Gamma)} . \tag{7.24}$$

The new quantum overlap, still taking into account that only $N_0$ can be handled by the detectors, is

$$|\langle\Phi_0|\Phi_1\rangle|^2 = \exp\left[-\frac{2N_0\left(1-\gamma\cos\omega_0\tau\right)}{1+\gamma\cos\left(\omega_0\tau-\Gamma\right)}\right] . \tag{7.25}$$

This shows that when the number of photons that the detection scheme can handle is limited, projection into a particular polarization state, at the expense of increasing the signal level, can be advantageous since the minimum probability of error achievable is decreased. From a quantum estimation point of view, WVA decreases the minimum probability of error reachable, since the projection makes possible to use the maximum number of photons available ($N_0$) with a corresponding decrease in mode overlap. Notice that the effect of using different polarization projections can be beautifully understood as reshaping of the balance between signal level and mode overlap.

### 7.2.2 Detector cannot differentiate between two signals

All experimental configurations show a limit on the amount of signal they can handle and how much sensitivity they can offer. On each specific experimental implementation, one or the other can be the main limiting factor that determines the tiniest change of a variable that can be measured. In

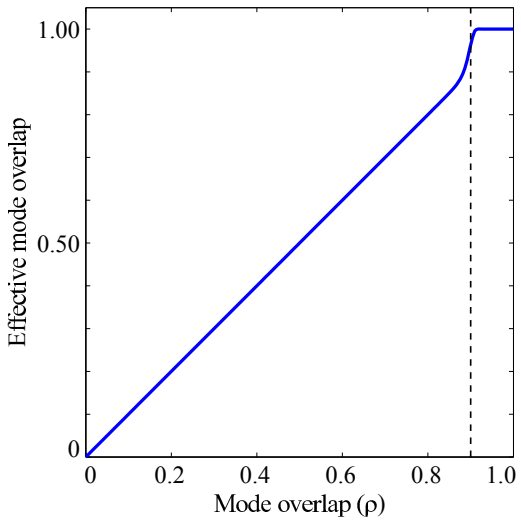


Figure 7.5: Effective mode overlap. For $\rho > 0.9$ the detection system cannot distinguish the states of interest. Data: $a = 0.9$ and $n = 100$.

many cases of interest, where the amount of signal can be safely increased, technical characteristics of the measuring apparatus establish a lower bound on the level of resolution achievable in the experiment. As a typical example, the experimental arrangement used in [30] to demonstrate the WVA scheme considered throughout this paper, it could no detect shifts of the centroid of any spectral distribution below $\delta\lambda \sim 0.01$ nm due to technical limitations of the equipment available. On practical terms, one can increase the signal to obtain a better resolution for $\delta\lambda \geq 0.01$ nm, while this was not feasible for $\delta\lambda \leq 0.01$ nm.

To be more specific, let us consider that specific experimental conditions makes hard, even impossible, to detect very similar modes, i.e., with mode overlap $\rho \sim 1$. We can represent this by assuming that there is an *effective* mode overlap ($\rho_{\text{eff}}$) which takes into account all relevant experimental limitations of a specific set-up, given by

$$\rho \Longrightarrow \rho_{\text{eff}} = 1 - (1 - \rho) \exp\left[-\left(\frac{\rho}{a}\right)^n\right] . \tag{7.26}$$

Fig. 7.5 shows an example where we assume that detected signals corresponding to $\rho > 0.9$ cannot be safely distinguished due to technical restrictions of the detection system. For $\rho > 0.9$, $\rho_{\text{eff}} = 1$, so the detection system cannot distinguish the states of interest even by increasing the level of the signal. On the contrary, for smaller values of $\rho$, accessible making use of a weak amplification scheme, this limitation does not exist since the detection

system can resolve this modes when enough signal is present.

### 7.2.3 Enhancement of the Fisher information

Up to now, we have used the concept of trace distance to look for the minimum probability of error achievable in *any* measurement when using a given quantum state. In doing that, we only considered how the quantum state changes for different values of the variable to be measured, without any consideration of how this quantum state is going to be detected. If we would like to include in the analysis additional characteristics of the detection scheme, one can use the concept of Fisher information, that requires to consider the probability distribution of possible experimental outcomes for a given value of the variable of interest. In this approach, one chooses different probability distributions to describe formally *characteristics* of specific detection scheme [39].

Let us assume that to estimate the value of the delay $\tau$, we measure the shift of the centroid ($\Delta f$) of the spectrum $\Phi_{\mathrm{u}}(\Omega)$, given by Eq. (7.4). A particular detection scheme will obtain a set of results $\{(\Delta f)_i\}$, $i = 1..M$ for a given delay $\tau$. $M$ is the number of photons detected. The Fisher information $I(\tau)$ provides a bound of $\mathrm{Var}\,(\hat{\tau})$ for any unbiased estimator when the probability distribution $p(\{(\Delta f)_i\}\,|\tau)$ of obtaining the set $\{(\Delta f)_i\}$, for a given $\tau$, is known.

In general, to determine the value of a parameter of interest $\tau$, we perform repeated measurements to estimate its value. From the measurements we obtain a distribution of outcomes $\{x\}$ which can be characterized by a probability distribution $p(x|\tau)$ that depends on the value of $\tau$. The variance of any unbiased estimator that makes use of the ensemble $\{x\}$ is bounded from below by $\mathrm{Var}(\hat{\tau}) \geq 1/I(\tau)$, where the Fisher information $I(\tau)$ reads $I(\tau) = -\int \mathrm{d}x\, p(x|\tau)\partial_\tau^2 p(x|\tau)$. When the Fisher function can be written as $I[\eta(\tau)]$, where $\eta$ is the variable that we measure, the Fisher information can be written as $I(\tau) = I(\eta)\left(\frac{\partial\eta}{\partial\tau}\right)^2$. If we assume that the probability distribution $p(\{(\Delta f)_i\}\,|\tau)$ is Gaussian, with mean value $\Delta f$ given by Eq. (7.5) and variance $\sigma^2$, determined by the errors inherent to the detection process, the Fisher information reads

$$I(\tau) = \frac{N}{\sigma^2}\left[\frac{\partial\Delta f}{\partial\tau}\right]^2, \tag{7.27}$$

where

$$\frac{\partial\Delta f}{\partial\tau} = \frac{\gamma B^2\left[B^2\tau^2\sin\phi - \omega_0\tau\left(\gamma+\cos\phi\right) - \sin\phi\left(1+\gamma\cos\phi\right)\right]}{2\pi\,\left(1+\gamma\cos\phi\right)^2} \tag{7.28}$$

and $\phi = \omega_0\tau - \Gamma$.

For $\phi = 0$, i.e., the angle of post-selection is $\theta = -\pi/2 + \omega_0\tau$, the flux of photons detected is$N = (N_0/2)\,(1+\gamma)$ and the Fisher information is

$$I_0 = \frac{N_0}{2}\,(1+\gamma) \times \frac{\gamma^2 B^4(\omega_0\tau)^2}{4\pi^2\sigma^2(1+\gamma)^2} = \frac{\gamma^2 B^4(\omega_0\tau)^2}{8\pi^2\sigma^2(1+\gamma)}\,. \tag{7.29}$$

Notice that $\theta = -\pi/2$ corresponds to considering equal input and output polarization state, i.e., no weak value amplification scheme.

For $\phi = \pi$, where the angle of post-selection is $\theta = \pi/2 + \omega_0\tau$, the flux of photons detected is $N = (N_0/2)\,(1-\gamma)$, and we have

$$I_\pi = \frac{N_0}{2}\,(1-\gamma) \times \frac{\gamma^2 B^4(\omega_0\tau)^2}{4\pi^2\sigma^2(1-\gamma)^2} = \frac{\gamma^2 B^4(\omega_0\tau)^2}{8\pi^2\sigma^2(1-\gamma)}\,, \tag{7.30}$$

where $\theta = \pi/2$ corresponds to considering an output polarization state orthogonal to the input polarization state i.e., when the effect of weak value amplification is most dramatic, as it can be easily observed in the upper panel of Fig. 7.2(a).

The Fisher bound for $\Phi = \pi$ is a factor $I_\pi/I_0 = (1+\gamma)/(1-\gamma)$ larger than the bound for $\Phi = 0$, so WVA achieves enhancement of the Fisher information. This Fisher information enhancement effect, which does not happen always, has been observed for certain WVA schemes [17, 39]. We should note that the enhancement of the Fisher information obtained comes from comparing two different and specific measurements, the results of projecting the signal that bears the sought-after information in different states in each case. Since we are not considering more general measurements to obtain the optimum measurement that maximize the Fisher information, it might be possible that other measurement schemes could further increase the Fisher information.

There is no contradiction between the facts that the minimum probability of error, obtained by making use of the concept of trace distance, is not enhanced by WVA, while at the same time there can be enhancement of the Fisher information with a particular measurement setup. By selecting a particular probability distribution to evaluate the Fisher information, we include information about the detection scheme. In our case, we estimate the value of $\tau$ by measuring the $\tau$-dependent shift of the centroid of the spectrum of the signal in one output port after $\mathrm{PBS}_2$, which is only part of all the information available, given by the full signal in Eqs. (7.3) and (7.4). We also assumed a Gaussian probability distribution with a constant variance $\sigma^2$ independent of $\tau$. The minimum probability of error that was obtained

making use of the trace distance depends on the full information available (the quantum state) before any particular detection. An unitary transformation, as the one where WVA is embedded, does not modify the bound. On the contrary, the Fisher information, by using a particular probability distribution to describe the possible outcomes in an particular experiment, selects certain aspects of the quantum state to be measured (*partial information*), and this bound can change in a WVA scheme, although the bound should be obviously always above the one determined by the minimum probability of error. In this restrictive scenario, the use of certain polarization projections can be preferable.

The existence and nature of these different bounds might possibly explain certain confusion about the capabilities of WVA, whether WVA is considered to provide any metrological advantage or not. On the one hand, if we consider the trace distance, or the quantum Cramér-Rao inequality, without any consideration about how the quantum states are detected, post-selection inherent in WVA does not lower the minimum probability of error achievable, so from this point of view WVA offers no metrological advantage. On the other hand, in certain scenarios, the Fisher information, when it takes into account *information about the detection scheme*, can be enhanced due to post-selection. In this sense, one can think of WVA as an advantageous way to optimize a particular detection scheme.

# Conclusions

WVA is embedded into measurement schemes that makes use of linear optics unitary transformations. Therefore, if the only limitations in a measurement are due to the quantum nature (*intrinsic statistics*) of the light, for instance, the presence of Shot noise in the case of coherent beams, WVA does not offer any advantage regarding any decrease of the minimum probability of error achievable. This is shown by making use of the trace distance between quantum states, which set sensitivity bounds that are independent of any particular post-selection. However, notice that this implicitly assume that full information about the quantum states used can be made available, and detectors are ideal, so they can detect any change of the variable of interest, as small as it might be, provided there is enough signal power. For instance, here we decided to measure the centroid shift of the spectral shape (specific information) in a given projection (we neglected all information concerning the other orthogonal projection. Therefore WVA cannot do better than using the full information contained in the quantum state.

Nevertheless, these assumptions are in many situations of interest far from true. These limitations, sometimes refereed as *technical noise*, even though not fundamental (one can always imagine using a better detector or a different detection scheme) are nonetheless important, since they limit the accuracy of specific detection systems at hand. In these scenarios, the importance of weak value amplification is that by decreasing the mode overlap associated with the states to be measured and possibly increasing the intensity of the signal, the weak value amplification scheme allows, in principle, to distinguish them with lower probability of error.

We have explored some of these scenarios from an quantum estimation theory point of view. For instance, we have seen that when the number of photons usable in the measurement is limited, the minimum probability of error achievable can be effectively decreased with weak value amplification. We have also analyzed how weak value amplification can differentiate between *in practice*-indistinguishable states by decreasing the mode overlap between its corresponding mode functions.

Finally we have discussed how the confusion about the usefulness of weak value amplification can possibly derive from considering different bounds related to how much sensitivity can, in principle, be achieved when estimating a certain variable of interest. One might possibly say that the advantages of WVA *have nothing to do with fundamental limits and should not be viewed as addressing fundamental questions of quantum mechanics* [85]. However, *from a practical rather than fundamental point of view*, the use of WVA can be advantageous in experiments where sensitivity is limited by experimental (technical), rather than fundamental, uncertainties. In any case, if a certain measurement is *optimum* depends on its capability to effectively reach any bound that might exist.

## Main publication by the author related to the contents of this chapter

J. P. Torres, and **L. J. Salazar-Serrano**, "Weak value amplification: a view from quantum estimation theory that highlights what it is and what isn't", Scientific Reports **6**, 19702 (2016).

CHAPTER

# EIGHT

# SUMMARY

In each previous chapter we included a section of conclusions devoted to summarize the main results of the piece of research discussed there. This final chapter is a brief section of overall conclusions. The aim is to summarize what are the main contributions of our research from a more general perspective.

Weak Value Amplification (WVA) is a concept that has been widely considered, and used in experiments, since first introduced by Aharonov, Albert and Vaidman in 1988 [2]. In 1991 the first experimental realization of the idea was done by Ritchie, Story and Hulet [5]. Over the next years, numerous experiments have made use, and still continue to use, the concept of WVA to measure tiny changes of a variable of interest. However, and *somehow surprisingly*, there is still and on-going debate about the *true usefulness* of the method for metrology, with papers highlighting its importance [39], and some others diminishing it [74].

In this thesis we have contributed to this field in three different aspects:

- First, we have applied the concept of WVA to enhance the sensitivity of experimental set-ups in two new scenarios: to measure extremely small temporal delays and to enhance the sensitivity of temperature sensors based on Fiber Bragg Gratings.

  In the first scenario, we have implemented a WVA scheme aimed at measuring a temporal delay between two optical pulses that is very small compared to the pulses duration [30]. Specifically, we have presented experiments in which we were able to measure a small delay ($\sim$ 20 fs between two pulses of duration $\sim$ 300 fs) applying a new method.

By measuring the spectrum of the output signal, a reshaping of the input spectrum is observed in which the shift of the central frequency reveals the value of the temporal delay itself.

Importantly, we have found that the central frequency shifts can be observed even in a regime, not so-often considered, where insertion losses are small, which broadens the applicability of the method demonstrated. The experimental scheme is implemented by using only linear optics elements and requires spectral measurements, hence making its implementation practical.

Moreover, we estimate that the ultimate sensitivity of the scheme implemented can provide observable frequency shifts for temporal delays of the order of attoseconds using femtosecond laser sources. The scheme developed thus appears as a promising method for measuring small and rapidly varying temporal delays.

In the second scenario, we have demonstrated that WVA can be used to enhance the sensitivity of sensors based on the use of Fiber Bragg Gratings [33]. With the proposed scheme, we were able to improve the sensitivity of a standard measuring methods. Even though we have demonstrated its feasibility to measure temperatures, the scheme is general and can be applied to measuring all kinds of physical parameters, provided they could generate a measurable change of the response of FBGs when interrogated by appropriate light beams.

With the scheme implemented, we have been able to reach a sensitivity of $0.035\,\mathrm{nm/^{\circ}C}$, a fourfold increase with respect to the use of the same FBG technologies, that offers $\sim 0.009\,\mathrm{nm/^{\circ}C}$. From our results we have found that in scenarios where the measurable shift of the spectrum is limited by the detection stage, but the decrease of signal energy that accompanies still keeps the signal-to-noise ratio at an usable level, weak value amplification is a promising scheme to enhance the capabilities of FBG-based sensor systems.

- We have also proposed and demonstrated a new device: a highly sensitive beam displacer [26] based on the concept of WVA that allows to displace the centroid of a Gaussian beam a distance much smaller than its beam width without the need to use movable optical elements. The beam's centroid position can be displaced by controlling the linear polarization in a post-selection stage where the dependence between the centroid's position and the angle of polarization is almost linear. From the experimental results we were able to shift the centroid of

a Gaussian beam with a beam waist of $\sim 600\,\mu$m, over the interval $-120\,\mu$m to $+120\,\mu$m in steps of less than $\sim 1\,\mu$m by rotating the post-selection polarizer between $0°$ and $90°$. The scheme presented turns to be advantageous with respect to other alternatives based on reflections or/and refractions induced by the rotation of a specific optical elements because the ultimate sensitivity is determined by the step size of the rotation stage used to rotate the post-selection polarizer which can be very small.

- Finally, we have determined in what sense WVA can be useful, when its use might be considered advantageous [86]. In this respect, we have joined the on-going debate regarding the true nature of WVA schemes and its true usefulness for achieving high sensitivity measurements with respect to other experimental techniques.

  We have introduced a new perspective to the issue by using the concept of quantum trace distance, that allows us to determine the pros and cons of using WVA by quantifying how much can be gained under appropriate circumstances. In particular, we have found that even though basic quantum estimation theory states that the post-selection of an appropriate output state obtained after unitary transformations cannot be better than the use of the input state [77], and thus WVA cannot be expected to enhance the precision of measurements [78], the concept of WVA can be useful when certain technical limitations are considered. In this respect, it might increase the ultimate resolution of the detection system by effectively lowering the value of the smallest quantity that can be detected.

  When using a WVA is inevitable that the signal detected is severely depleted, due to the quasi-orthogonality of the input and output states selected. However, in many applications, limitations are not related to the low intensity of the signal [3], but to the smallest change that the detector can measure irrespectively of the intensity level of the signal. These limitations, sometimes refereed as *technical noise*, even though not fundamental (one can always imagine using a better detector or a different detection scheme) are nonetheless important, since they limit the accuracy of specific detection systems at hand. In these scenarios, the importance of weak value amplification is that by decreasing the mode overlap associated with the states to be measured and possibly increasing the intensity of the signal, the weak value amplification scheme allows, in principle, to distinguish them with lower probability

of error.

As a result, we have found that *from a practical rather than fundamental point of view*, the use of WVA can be advantageous in experiments where sensitivity is limited by experimental (technical), rather than fundamental, uncertainties. In any case, if a certain measurement is *optimum* depends on its capability to effectively reach any bound that might exist.

APPENDIX

# A

# MATHEMATICAL DESCRIPTION OF WEAK VALUE AMPLIFICATION: QUANTUM AND CLASSICAL VIEWS

In this appendix we provide a more mathematical description of several concepts that are core ideas in this thesis: the concepts of weak measurement, weak value amplification and weak value. We do this from both quantum and classical perspectives.

## A.1 Strong and weak measurements

A measurement is a physical process that involves the interaction of two subsystems. One is referred as the *meter*, that is the subsystem that will tell us the state of the other subsystem, referred as the *system*, and whose state we want to measure. When the two subsystems interact, a correlation between the meter and the system is generated, so that a property of the meter changes depending on what it is the state of the system.

Generally speaking, the interaction between the meter and the system, the measurement process, can be described by a Hamiltonian of the form

$$\hat{H}(t) = -g\,\hat{q}\hat{A}\,, \tag{A.1}$$

where $\hat{q}$ is the quantum observable corresponding to the meter, $\hat{A}$ is an operator with eigenvalues $a_n$ and eigenstates $|a_n\rangle$ that describe the physical observable of the system to be measured, and $g$ is a parameter that defines the strength of the interaction.

Before the measurement, the global system (meter and system) is prepared in a joint state

$$|\Xi_{\rm in}\rangle = |\Psi_{\rm i}\rangle\,|\Phi_i\rangle\,, \tag{A.2}$$

that is separable. The meter is prepared in the state $|\Phi_i\rangle$ described by a Gaussian function with spread $\sigma_q$ in the q representation, i.e.,

$$|\Phi_{\rm i}\rangle = \int {\rm d}q\, \exp\left(-\frac{q^2}{2\sigma_q^2}\right)|q\rangle\ . \tag{A.3}$$

The initial quantum state of the system $|\Psi_{\rm in}\rangle$ can be expanded in terms of the eigenstates of the observable $\hat{A}$, that is

$$|\Psi_{\rm i}\rangle = \sum_n \alpha_n\,|a_n\rangle\ . \tag{A.4}$$

When the measurement is performed, the two subsystems interact and the whole system evolves to the entangled state $|\Xi_{\rm out}\rangle$ that reads

$$\begin{aligned} |\Xi_{\rm out}\rangle &= \exp\left(-\frac{i}{\hbar}\int {\rm d}t\,\hat{H}(t)\right)|\Phi_{\rm i}\rangle\,|\Psi_{\rm i}\rangle \\ &= \exp\left(i\epsilon\hat{q}\hat{A}\right)|\Phi_{\rm i}\rangle\,|\Psi_{\rm i}\rangle\ , \end{aligned} \tag{A.5}$$

where $\epsilon = gT/\hbar$ and $T$ is the interaction time. The quantum state after the interaction, given by Eq. A.5, can be written as

$$|\Xi_{\rm out}\rangle = \sum_n \alpha_n \int {\rm d}q\, \exp\left(-\frac{q^2}{2\sigma_q^2}\right)\exp\left(i\epsilon q a_n\right)|a_n\rangle\,|q\rangle\ . \tag{A.6}$$

A quantum state in the q-representation is generally written as

$$|\Phi\rangle = \int {\rm d}dq\, F(q)\,|q\rangle\ .$$

If we define

$$\begin{aligned} |q\rangle &= (2\pi)^{-1/2}\int {\rm d}p\, \exp\left(-ipx\right)|p\rangle \\ F(q) &= (2\pi)^{-1/2}\int {\rm d}p\, G(p)\exp\left(ipx\right)|p\rangle\,, \end{aligned} \tag{A.7}$$

the quantum state in the p-representation reads as

$$|\Phi\rangle = \int {\rm d}p\, G(p)\,|p\rangle\ .$$

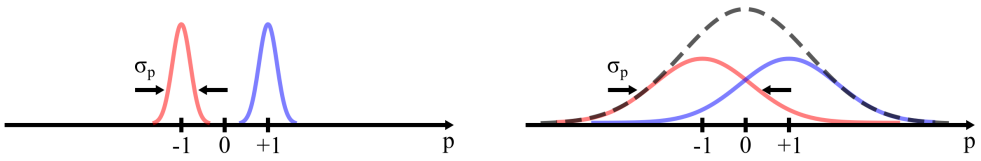


(a) (b)

Figure A.1: (a) Strong measurement. The uncertainty $\sigma_p$ is small compared to the separation between the possible outcomes $\{-1, +1\}$. (b) Weak measurement. The large uncertainty $\sigma_p$ makes impossible to differentiate the possible outcomes since the probability distribution observed is a single peak (dashed line).

Making use of these results, the quantum state given by Eq. (A.6) reads in the p-representation as

$$|\Xi_{\text{out}}\rangle = \sum_n \alpha_n \int \mathrm{d}p \, \exp\left[-\frac{(p-\epsilon a_n)^2}{2\sigma_p^2}\right] |a_n\rangle \, |p\rangle \ , \tag{A.8}$$

where $\sigma_p = 1/\sigma_q$. Inspection of Eq. (A.8) shows that after the interaction the meter and the system are left in an entangled state.

The probability to measure a certain value $p$ of the meter is

$$P(p) = \sum_n |\alpha_n|^2 \exp\left[-\frac{(p-\epsilon a_n)^2}{\sigma_p^2}\right] \ , \tag{A.9}$$

that is a superposition of Gaussian functions of width $\sigma_p$ that are centered in the positions determined by $\epsilon a_n$. As a result, the meter's final position is correlated to the different outcomes (eigenvalues) of the observable $\hat{A}$.

Depending on the relation between the spacing between adjacent outcomes and the meter's uncertainty $\sigma_p$, two different regimes of operation are considered. If $\sigma_p$ is small compared to the spacing between adjacent outcomes, the measurement is termed as a *strong measurement* since the distribution in Eq. (A.9) is composed of widely separated peaks as shown in Fig. A.1(a). On the contrary, if $\sigma_p$ is larger that the spacing between possible outcomes, the interaction is referred as *weak measurement* and the probability distribution becomes a single broad peak like the one shown in Fig. A.1(b).

In the case of a weak measurement, shown in Fig. A.1(b), the meter's uncertainty $\sigma_p$ is much larger than the spread of the values $\epsilon a_n$. In this

regime, the eigenvalues of the observable are not resolved by the measuring device since the probability distribution of Eq. (A.9) corresponds to a single broad Gaussian that is centered in the mean value of $\hat{A}$ given by $\langle \hat{A} \rangle = \sum_n |\alpha_n|^2 a_n$. Therefore, a single measurement does not provide any valuable information about the possible outcomes $a_n$ since $\sigma_p \gg \langle \hat{A} \rangle$. However, in situations where the measurement can be performed a large number of times, the probability distribution can be reconstructed and the quantity $\langle \hat{A} \rangle$ can be estimated to an accuracy that depends on the number of realizations.

## A.2 From weak measurements to the concept of weak value

While the weakness of the coupling between meter and system can be seen at first sight as disadvantageous in a measurement, Aharonov, Albert, and Vaidman [2] showed that when appropriate initial and final states of the system are selected (pre- and post-selection), the value of the meter can be shifted by an unexpectedly large amount. It was soon suggested that these ideas may find application in metrology [38, 53].

To illustrate this new idea, consider the state given by Eq. A.5. If we consider a weak interaction and expand the exponential to first order in $\epsilon$, we obtain

$$|\Xi_{\text{out}}\rangle = |\Phi_{\text{i}}\rangle |\Psi_{\text{i}}\rangle + i\epsilon \hat{q}\hat{A} |\Phi_{\text{i}}\rangle |\Psi_{\text{i}}\rangle . \tag{A.10}$$

If we project the state of the system into the final state $|\Psi_{\text{f}}\rangle$ (post-selection), the quantum state of the meter after projection of the state of the system reads

$$|\Phi_{\text{out}}\rangle = \langle \Psi_{\text{f}}|\Psi_{\text{i}}\rangle \left\{ |\Phi_{\text{i}}\rangle + i\epsilon A_w \hat{q} |\Phi_{\text{i}}\rangle \right\} , \tag{A.11}$$

where

$$A_w = \frac{\langle \Psi_{\text{f}}| \hat{A} |\Psi_{\text{i}}\rangle}{\langle \Psi_{\text{f}}|\Psi_{\text{i}}\rangle} \tag{A.12}$$

is the so-called *weak value* of $\hat{A}$. Notice that the weak value $A_w$ is in general a complex number.

To first order, we can rewrite Eq. (A.11) as

$$|\Phi_{\text{out}}\rangle = \langle \Psi_{\text{f}}|\Psi_{\text{i}}\rangle \exp\left(i\epsilon A_w \hat{q}\right) |\Phi_{\text{i}}\rangle . \tag{A.13}$$

For the sake of simplicity, we assume that the weak value is real. In this case, in the p-representation, the probability to obtain a certain p value is

now

$$P(p) = \frac{1}{(\pi\sigma_p^2)^{1/4}} \exp\left[-\frac{(p-\epsilon A_w)^2}{\sigma_p^2}\right], \tag{A.14}$$

so the centroid of the probability distribution that describes the possible outcomes of the meter is now shifted to $\epsilon A_w$.

This is an important result since the weak value can become arbitrarily large, as we will see, when the initial and final quantum states $|\Psi_\mathrm{i}\rangle$ and $|\Psi_\mathrm{f}\rangle$ are almost orthogonal. As a result, Eq. (A.14) states the meter's position may lie outside the range of the observable's eigenvalues. In this way the shift of the centroid can be extremely large, what is sometimes termed as Weak Value Amplification. This has been demonstrated to be very useful in metrology since it enables the measurement of extremely small physical quantities characterized by the parameter $\epsilon$.

## A.3 Real and Imaginary weak values

Given a specific interaction, the selection of the initial and final states of the quantum system defines the nature of the weak value, and determines in which domain the *weak value amplification* effect can be observed. In particular, for the interaction defined by the Hamiltonian in Eq. (A.1), a real weak value yields an amplification effect observed in the p-domain. This situation is clearly seen from Eq. (A.14), where the meter's centroid of p possible p values is amplified from $\epsilon$ to $\epsilon A_w$ by a factor $\mathrm{Re}[A_w]$.

Conversely, for an imaginary weak value, the amplification effect is observed in the q-domain. In this case, the state of the meter is

$$|\Phi_\mathrm{out}\rangle \sim \int \mathrm{d}q \, \exp\left(-\frac{q^2}{2\sigma_q^2}\right)(1+\epsilon \mathrm{Im}[A_w]q)\,|q\rangle \ . \tag{A.15}$$

The centroid of the possible q-values of the meter is $\epsilon\sigma_q^2\mathrm{Im}[A_w]$.

To illustrate both cases with an example, let us consider the observable

$$\hat{A} = |H\rangle\langle H| - |V\rangle\langle V| = \begin{pmatrix} 1 & 0 \\ 0 & -1 \end{pmatrix}, \tag{A.16}$$

where $|H\rangle$ and $|V\rangle$ denote states of horizontal and vertical polarization.

To generate a real weak value we require states of linear polarization to perform the pre-selection and post-selection operations. That is, we pre-select the system in the state $|\Psi_\mathrm{i}\rangle = (|H\rangle + |V\rangle)/\sqrt{2}$, and after the weak interaction we post-select it in the state $|\Psi_\mathrm{f}\rangle = \cos(3\pi/2+\zeta)\,|H\rangle + \sin(\pi/2+$

$\zeta)\,|V\rangle$, where $\zeta = 0$ corresponds to the case where both polarization states are orthogonal. Following Eq. (A.12), we obtain that the weak value of $\hat{A}$ is a real quantity given by

$$A_w = \cot(\zeta) \approx \frac{1}{\zeta}\,. \tag{A.17}$$

In contrast, to generate an imaginary weak value we make use of states of circular polarization given by $|\Psi_\mathrm{i}\rangle = (|H\rangle + \exp(-i\pi/2)\,|V\rangle)/\sqrt{2}$ for pre-selection, which corresponds to a state of left-handed circular polarization, and $|\Psi_\mathrm{f}\rangle = (|H\rangle + \exp(i\Gamma)\,|V\rangle)/\sqrt{2}$ for the post-selection. In the particular case where the post-selection angle $\Gamma$ is given by $\Gamma = \pi/2 + \zeta$, where $\zeta = 0$ corresponds to a state of right-handed circular polarization (a state orthogonal to the input state), the weak value reads

$$A_w = i\cot(\zeta/2) \approx \frac{2i}{\zeta}\,, \tag{A.18}$$

which is an imaginary quantity.

## A.4 WVA explained as a classical interference effect

Although the concept of weak value amplification originates from research on quantum theory, the phenomenon of weak value amplification can be readily understood in terms of constructive and destructive interference between probability amplitudes in a quantum mechanics context [4], or in terms of interference of classical waves [11, 19]. Indeed, most of the experimental implementations of the concept, since its first demonstration in 1991 by Ritchie and colleagues [5], belong to the last type.

### A.4.1 Case of a real weak value

To illustrate the concept of WVA from a classical interference point of view, we will analyze first the demonstration of the concept of weak value amplification from 1991, which corresponds to the example of real weak value discussed in Chapter 2.

Let us consider a polarized input optical beam (input polarization $\hat{\mathbf{e}}_\mathrm{in} = (\hat{\mathbf{x}} + \hat{\mathbf{y}})/\sqrt{2}$

$$\mathbf{E}_\mathrm{in} = E_0 \exp\left[-\frac{x^2}{2w^2}\right]\left(\frac{\hat{\mathbf{x}} + \hat{\mathbf{y}}}{\sqrt{2}}\right)\,, \tag{A.19}$$

where $w$ is the beam waist and $\hat{\mathbf{x}}$, $\hat{\mathbf{y}}$ designate horizontal and vertical polarizations, respectively. The beam enters a medium where is subjected to a polarization dependent spatial displacement $\Delta$ (coupling of polarization and location of the beam). After the interaction, the electric field writes

$$\mathbf{E}_{\text{out}} = \frac{E_0}{\sqrt{2}} \left\{ \exp\left[ -\frac{(x-\Delta)^2}{2w^2} \right] \hat{\mathbf{x}} + \exp\left[ -\frac{(x+\Delta)^2}{2w^2} \right] \hat{\mathbf{y}} \right\} . \tag{A.20}$$

After projection of the optical signal into a polarization state $\hat{\mathbf{e}}_{\text{out}} = \cos\alpha\, \hat{\mathbf{x}} + \sin\alpha\, \hat{\mathbf{y}}$, the amplitude $A$ of the optical beam writes

$$A = \frac{E_0}{\sqrt{2}} \left\{ \cos\alpha \exp\left[ -\frac{(x-\Delta)^2}{2w^2} \right] + \sin\alpha \exp\left[ -\frac{(x+\Delta)^2}{2w^2} \right] \right\} . \tag{A.21}$$

From Eq. (A.21), the centroid of the intensity distribution of the beam is

$$\langle x \rangle = \frac{\int \mathrm{d}x\, x\, |A|^2}{\int \mathrm{d}x\, |A|^2} = \left( \frac{\cos 2\alpha}{1 + \gamma \sin 2\alpha} \right) \Delta \,, \tag{A.22}$$

where

$$\gamma = \exp\left( -\frac{\Delta^2}{w^2} \right) , \tag{A.23}$$

which is close to 1 since $\Delta \ll w$ in a weak interaction regime.

If we select $\alpha = -\pi/2 + \zeta$, being $\zeta$ small, we obtain

$$\begin{aligned} \cos 2\alpha &= \sin 2\zeta \sim 2\zeta \\ \sin 2\alpha &= -\cos 2\zeta \sim -1 + 2\zeta^2 \,, \end{aligned} \tag{A.24}$$

where $\zeta = 0$ corresponds to an output polarization that is orthogonal to the input polarization. The location of the centroid of the intensity distribution is

$$\langle x \rangle = \left( \frac{2 \sin\zeta \cos\zeta}{1 - \gamma \cos^2\zeta + \gamma \sin^2\zeta} \right) \Delta \,. \tag{A.25}$$

Considering that $\gamma \sim 1$ in the weak regime, we obtain

$$\langle x \rangle = \Delta \frac{1}{\tan\zeta} = A_w \Delta \sim \frac{\Delta}{\zeta} \,. \tag{A.26}$$

### A.4.2 Case of an imaginary weak value

Let us consider the experiment performed in 2008 by Hosten and Kwiat [3], where a polarization-dependent displacement of the order of one angstrom was measured in the direction perpendicular to a refractive index gradient.

In the experiment, an input optical beam horizontally polarized, given by

$$\mathbf{E}_{\text{in}} = E_0 \exp\left[-\frac{p^2 w^2}{2}\right] \left(\frac{\hat{\mathbf{R}} + \hat{\mathbf{L}}}{\sqrt{2}}\right) , \tag{A.27}$$

where $p$ is the transverse wavenumber in one dimension, $w$ is the beam waist, $\hat{\mathbf{R}} = (\hat{\mathbf{x}} + i\hat{\mathbf{y}})/\sqrt{2}$ designates right-handed circular polarization and $\hat{\mathbf{L}} = (\hat{\mathbf{x}} - i\hat{\mathbf{y}})/\sqrt{2}$ designates left-handed circular polarization, refracts in the interface between two dielectric media. The gradient in index of refraction produces a polarization dependent p-dependent phase shift. After the interaction, the electric field writes

$$\mathbf{E}_{\text{out}} = \frac{E_0}{\sqrt{2}} \left\{ \exp\left[-\frac{p^2 w^2}{2} - ip\delta\right] \hat{\mathbf{R}} + \exp\left[-\frac{p^2 w^2}{2} + ip\delta\right] \hat{\mathbf{L}} \right\} . \tag{A.28}$$

After post-selecting the optical signal into a polarization state given by $\hat{\mathbf{e}}_{\text{out}} = (\exp(-i\zeta)\,\hat{\mathbf{R}} + \exp(i\zeta)\,\hat{\mathbf{L}})/\sqrt{2}i$, the amplitude $A$ of the output optical beam becomes

$$A = E_0 \exp\left(-\frac{p^2 w^2}{2}\right) \sin\left(p\delta + \zeta\right) . \tag{A.29}$$

The centroid of the intensity distribution in the p-domain is

$$\langle p \rangle = \frac{\int \mathrm{d}p\, p\, |A|^2}{\int \mathrm{d}p\, |A|^2} = \frac{(2\delta\zeta)/w^2}{\zeta^2 + \delta^2/w^2} = \frac{2\delta}{w^2\zeta} \frac{1}{1 + \delta^2/(w\zeta)^2} . \tag{A.30}$$

If $\delta \ll \zeta w$, we have

$$\langle p \rangle = \frac{2\delta}{w^2\zeta} , \tag{A.31}$$

which corresponds to the case of an imaginary weak value.

APPENDIX

# B

# PRODUCT THEOREM FOR GAUSSIAN FUNCTIONS

In this appendix we present a result that is widely used in this thesis to derive many of the expressions that we have obtained. For instance, the derivation of Eq. (5.4) and Eq. (6.3) have made use of the result discussed here. This is the product theorem for Gaussian functions [87] that states that the product of two Gaussian functions is also a Gaussian function. The peak amplitude, centroid and width of the new Gaussian function depends on the peak amplitude, centroid and width of each one of the original Gaussian functions.

Let us be more specific. Let us consider two Gaussian function of the variable $x$:

$$G_1(x) = A_1 \exp\left[-\frac{(x-\mu_1)^2}{2\sigma_1^2}\right]$$
$$G_2(x) = A_2 \exp\left[-\frac{(x-\mu_2)^2}{2\sigma_2^2}\right] \tag{B.1}$$

where $\mu_i$ $(i = 1, 2)$ corresponds to the centroid of each Gaussian function, $\sigma_i$ are the widths and $A_i$ are the corresponding peak amplitudes

The product $G_1(x)G_2(x)$ of the functions can be written as a new Gaussian function $G_3(x)$ that reads as

$$G_3(x) = A_1 A_2 \exp\left[-\frac{(\mu_1-\mu_2)^2}{2(\sigma_1^2+\sigma_2^2)}\right] \exp\left[-\frac{(x-\mu)^2}{2\sigma^2}\right] . \tag{B.2}$$

The theorem shows that the centroid of the new Gaussian function is

$$\mu = \frac{\mu_1\sigma_1^2 + \mu_2\sigma_2^2}{\sigma_1^2+\sigma_2^2} , \tag{B.3}$$

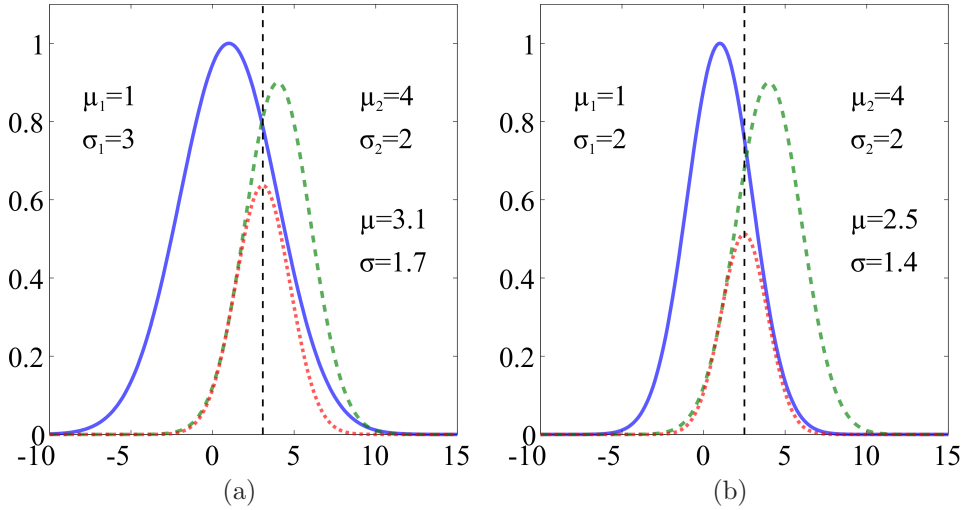


Figure B.1: (a) Product of Gaussian functions with different widths. $G_1(x)$ (continuous blue line) is a Gaussian function centered at $\mu_1 = 1$, with width $\sigma_1 = 3$ and peak amplitude $A_1 = 1$. $G_2(x)$ (green dashed line) is centered at $\mu_1 = 4$, its width is $\sigma_2 = 2$ and its peak amplitude is $A_2 = 0.9$. The product (red dotted line) is a narrower Gaussian function with height 0.63, width $\tilde{\sigma} = 1.7$, centered at $\tilde{\mu} = 3.1$. (b) Product of two Gaussian functions with equal widths $\sigma_1 = \sigma_2 = 2$. Since $G_1(x)$ (continuous blue line) is centered at $\mu_1 = 4$ and $G_2(x)$ (green dashed line) is centered at $\mu_1 = 1$, one obtains that the centroid of the product is $\tilde{\mu} = (\mu_1 + \mu_2)/2 = 2.5$. The Gaussian with is reduced by a factor of $\sqrt{2}$ and the height is 0.51.

its width is

$$\sigma^2 = \frac{\sigma_1^2 \sigma_2^2}{\sigma_1^2 + \sigma_2^2}\,, \tag{B.4}$$

and its peak amplitude is reduced to

$$A_0 = A_1 A_2 \exp\left[-\frac{(\mu_1 - \mu_2)^2}{2(\sigma_1^2 + \sigma_2^2)}\right]\,. \tag{B.5}$$

When the two Gaussian functions have the same width ($\sigma_1 = \sigma_2 = \sigma$) but

are centered in different locations, Eqs. (B.3), (B.4) and (B.5) simplify to

$$\mu = \frac{\mu_1 + \mu_2}{2} \tag{B.6}$$

$$\sigma^2 = \frac{\sigma^2}{2} \tag{B.7}$$

$$A_0 = A_1 A_2 \exp\left[-\frac{(\mu_1 - \mu_2)^2}{4\sigma^2}\right], \tag{B.8}$$

respectively. To visualize these results, Fig. B.1 shows two representative cases where two Gaussian functions are multiplied. In both cases the result is a Gaussian function that is narrower than both original functions and centered in between the two original centroids, $\mu_1$ and $\mu_2$.

# BIBLIOGRAPHY


[1] C. W. Helstrom, ed., *Quantum Detection and Estimation Theory* (Academic press, 1976).

[2] Y. Aharonov, D. Albert, and L. Vaidman, "How the result of a measurement of a component of the spin of a spin-1/2 particle can turn out to be 100," Phys. Rev. Lett. **60**, 1351 (1988).

[3] O. Hosten and P. G. Kwiat, "Observation of the Spin Hall Effect of Light via Weak Measurements," Science **319**, 787 (2008).

[4] I. M. Duck, P. M. Stevenson, and E. C. G. Sudarshan, "The sense in which a "weak measurement" of a spin-1/2 particle's spin component yields a value 100," Phys. Rev. D **40**, 2112 (1989).

[5] N. Ritchie, J. Story, and R. Hulet, "Realization of a measurement of a "weak value"," Phys. Rev. Lett. **66**, 1107 (1991).

[6] C. Cohen-Tannoudji, B. Diu, and F. Laloë, *Quantum mechanics* (Wiley, 1977).

[7] B. E. Y. Svensson, "Pedagogical Review of Quantum Measurement Theory with an Emphasis on Weak Measurements," Quanta **2**, 18 (2013).

[8] A. Cho, "Furtive approach rolls back the limits of quantum uncertainty," Science **333**, 690 (2011).

[9] A. Peres, "Quantum measurements with postselection," Phys. Rev. Lett. **62**, 2326 (1989).

[10] A. J. Leggett, "Comment on How the result of a measurement of a component of the spin of a spin-1/2 particle can turn out to be 100," Phys. Rev. Lett. **62**, 2325 (1989).

[11] J. P. Torres, G. Puentes, N. Hermosa, and L. J. Salazar-Serrano, "Weak interference in the high-signal regime," Opt. Express **20**, 18869 (2012).

[12] X. Zhou, X. Ling, H. Luo, and S. Wen, "Identifying graphene layers via spin Hall effect of light," Appl. Phys. Lett. **101**, 251602 (2012).

[13] P. B. Dixon, D. J. Starling, A. N. Jordan, and J. C. Howell, "Ultrasensitive Beam Deflection Measurement via Interferometric Weak Value Amplification," Phys. Rev. Lett. **102**, 173601 (2009).

[14] M. Pfeifer and P. Fischer, "Weak value amplified optical activity measurements," Opt. Express **19**, 16508 (2011).

[15] X.-Y. Xu, Y. Kedem, K. Sun, L. Vaidman, C.-F. Li, and G.-C. Guo, "Phase Estimation with Weak Measurement Using a White Light Source," Phys. Rev. Lett. **111**, 033604 (2013).

[16] D. J. Starling, P. B. Dixon, A. N. Jordan, and J. C. Howell, "Precision frequency measurements with interferometric weak values," Phys. Rev. A **82**, 063822 (2010).

[17] G. I. Viza, J. Martínez-Rincón, G. a. Howland, H. Frostig, I. Shomroni, B. Dayan, and J. C. Howell, "Weak-values technique for velocity measurements," Opt. Lett. **38**, 2949 (2013).

[18] P. Egan and J. a. Stone, "Weak-value thermostat with 0.2 mK precision," Opt. Lett. **37**, 4991 (2012).

[19] J. C. Howell, D. J. Starling, P. B. Dixon, P. K. Vudyasetu, and A. N. Jordan, "Interferometric weak value deflections: Quantum and classical treatments," Phys. Rev. A **81**, 033813 (2010).

[20] D. J. Starling, P. B. Dixon, A. N. Jordan, and J. C. Howell, "Optimizing the signal-to-noise ratio of a beam-deflection measurement with interferometric weak values," Phys. Rev. A **80**, 041803 (2009).

[21] J. M. Hogan, J. Hammer, S.-W. Chiow, S. Dickerson, D. M. S. Johnson, T. Kovachy, a. Sugarbaker, and M. a. Kasevich, "Precision angle sensor using an optical lever inside a Sagnac interferometer," Opt. Lett. **36**, 1698 (2011).

[22] M. D. Turner, C. a. Hagedorn, S. Schlamminger, and J. H. Gundlach, "Picoradian deflection measurement with an interferometric quasi-autocollimator using weak value amplification," Opt. Lett. **36**, 1479 (2011).

[23] X. Zhou, Z. Xiao, H. Luo, and S. Wen, "Experimental observation of the spin Hall effect of light on a nanometal film via weak measurements," Phys. Rev. A **85**, 043809 (2012).

[24] L. Zhou, Y. Turek, C. P. Sun, and F. Nori, "Weak-value amplification of light deflection by a dark atomic ensemble," Phys. Rev. A **88**, 053815 (2013).

[25] G. Jayaswal, G. Mistura, and M. Merano, "Observation of the Imbert-Fedorov effect via weak value amplification," Opt. Lett. **39**, 2266 (2014).

[26] L. J. Salazar-Serrano, D. Guzmán, A. Valencia, and J. P. Torres, "Demonstration of a highly-sensitive tunable beam displacer with no movable elements based on the concept of weak value amplification," Opt. Express **23**, 10097 (2015).

[27] O. S. Magaña Loaiza, M. Mirhosseini, B. Rodenburg, and R. W. Boyd, "Amplification of angular rotations using weak measurements," Phys. Rev. Lett. **112**, 200401 (2014).

[28] N. Brunner and C. Simon, "Measuring Small Longitudinal Phase Shifts: Weak Measurements or Standard Interferometry?" Phys. Rev. Lett. **105**, 010405 (2010).

[29] G. Strübi and C. Bruder, "Measuring Ultrasmall Time Delays of Light by Joint Weak Measurements," Phys. Rev. Lett. **110**, 083605 (2013).

[30] L. J. Salazar-Serrano, D. Janner, N. Brunner, V. Pruneri, and J. P. Torres, "Measurement of sub-pulse-width temporal delays via spectral interference induced by weak value amplification," Phys. Rev. A **89**, 012126 (2014).

[31] D. J. Starling, P. B. Dixon, N. S. Williams, A. N. Jordan, and J. C. Howell, "Continuous phase amplification with a Sagnac interferometer," Phys. Rev. A **82**, 011802 (2010).

[32] C.-F. Li, X.-Y. Xu, J.-S. Tang, J.-S. Xu, and G.-C. Guo, "Ultrasensitive phase estimation with white light," Phys. Rev. A **83**, 044102 (2011).

[33] L. J. Salazar-Serrano, D. Barrera, W. Amaya, S. Sales, V. Pruneri, J. Capmany, and J. P. Torres, "Enhancement of the sensitivity of a temperature sensor based on fiber Bragg gratings via weak value amplification," Opt. Lett. **40**, 3962 (2015).

[34] M. Givens, "Photoelectric Detection of Interference between Two Light Beams Having a Large Path Difference," J. Opt. Soc. Am. **51**, 1030 (1961).

[35] L. Mandel, "Interference and the alford and gold effect," J. Opt. Soc. Am. **52**, 1335 (1962).

[36] W. P. Alford and A. Gold, "Laboratory Measurement of the Velocity of Light," Am. J. Phys. **26**, 481 (1958).

[37] X. Zou, T. Grayson, and L. Mandel, "Observation of quantum interference effects in the frequency domain," Phys. Rev. Lett. **69**, 3041 (1992).

[38] J. Dressel, M. Malik, F. M. Miatto, A. N. Jordan, and R. W. Boyd, "Understanding quantum weak values: Basics and applications," Rev. Mod. Phys. **86**, 307 (2014).

[39] A. N. Jordan, J. Martínez-Rincón, and J. C. Howell, "Technical Advantages for Weak-Value Amplification: When Less Is More," Phys. Rev. X **4**, 011031 (2014).

[40] J. Dressel, K. Lyons, A. N. Jordan, T. M. Graham, and P. G. Kwiat, "Strengthening weak-value amplification with recycled photons," Phys. Rev. A **88**, 023821 (2013).

[41] C. V. S. Borges, M. Hor-Meyll, J. A. O. Huguenin, and A. Z. Khoury, "Bell-like inequality for the spin-orbit separability of a laser beam," Phys. Rev. A **82**, 033833 (2010).

[42] K. H. Kagalwala, G. Di Giuseppe, A. F. Abouraddy, and B. E. a. Saleh, "Bell's measure in classical optical coherence," Nat. Photonics **7**, 72 (2012).

[43] B. N. Simon, S. Simon, F. Gori, M. Santarsiero, R. Borghi, N. Mukunda, and R. Simon, "Nonquantum Entanglement Resolves a Basic Issue in Polarization Optics," Phys. Rev. Lett. **104**, 023901 (2010).

[44] X.-F. Qian and J. H. Eberly, "Entanglement and classical polarization states," Opt. Lett. **36**, 4110 (2011).

[45] J. Kim, J. A. Cox, J. Chen, and F. X. Kärtner, "Drift-free femtosecond timing synchronization of remote optical and microwave sources," Nat. Photonics **2**, 733 (2008).

[46] J. Lee, Y.-J. Kim, K. Lee, S. Lee, and S.-W. Kim, "Time-of-flight measurement with femtosecond light pulses," Nat. Photonics **4**, 716 (2010).

[47] R. Trebino, "Measuring the seemingly immeasurable," Nat. Photonics **5**, 189 (2011).

[48] A. Pe'er, B. Dayan, A. a. Friesem, and Y. Silberberg, "Temporal shaping of entangled photons," Phys. Rev. Lett. **94**, 073601 (2005).

[49] F. Boitier, A. Godard, J. Bonnet, E. Rosencher, and C. Fabre, "Measuring photon bunching at ultrashort timescale by two-photon absorption in semiconductors," Nat. Phys. **5**, 267 (2009).

[50] C. K. Hong, Z. Y. Ou, and L. Mandel, "Measurement of Subpicosecond Time Intervals between Two Photons by Interference," Phys. Rev. Lett. **59**, 2044 (1987).

[51] A. Steinberg, P. Kwiat, and R. Chiao, "Measurement of the single-photon tunneling time," Phys. Rev. Lett. **71**, 708 (1993).

[52] R. Kaltenbaek, J. Lavoie, D. N. Biggerstaff, and K. J. Resch, "Quantum-inspired interferometry with chirped laser pulses," Nat. Phys. **4**, 864 (2008).

[53] Y. Aharonov and L. Vaidman, "Properties of a quantum system during the time interval between two measurements," Phys. Rev. A **41**, 11 (1990).

[54] B. Povazay, K. Bizheva, A. Unterhuber, B. Hermann, H. Sattmann, A. F. Fercher, W. Drexler, A. Apolonski, W. J. Wadsworth, J. C.

Knight, P. S. J. Russell, M. Vetterlein, and E. Scherzer, "Submicrometer axial resolution optical coherence tomography," Opt. Lett. **27**, 1800 (2002).

[55] V. J. Fowler and J. Schlafer, "A survey of laser beam deflection techniques," Appl. Opt. **5**, 1675 (1966).

[56] N. Treps, U. Andersen, B. Buchler, P. K. Lam, a. Maître, H.-a. Bachor, and C. Fabre, "Surpassing the standard quantum limit for optical imaging using nonclassical multimode light," Phys. Rev. Lett. **88**, 203601 (2002).

[57] T. Mu, C. Zhang, Q. Li, L. Zhang, Y. Wei, and Q. Chen, "Achromatic Savart polariscope: choice of materials," Opt. Express **22**, 5043 (2014).

[58] M. Fiorentino and R. G. Beausoleil, "Compact sources of polarization-entangled photons," Opt. Express **16**, 20149 (2008).

[59] T. I. Xu Y., "Interferometric imaging of hydrogels undergoing volume changes," Macromolecules **32**, 4596 (1999).

[60] E. J. Galvez, "Achromatic polarization-preserving beam displacer," Opt. Lett. **26**, 971 (2001).

[61] X. Yin, L. Hesselink, Z. Liu, N. Fang, and X. Zhang, "Large positive and negative lateral optical beam displacements due to surface plasmon resonance," Appl. Phys. Lett. **85**, 372 (2004).

[62] Y. Li, "Laser beam scanning by rotary mirrors. II. Conic-section scan patterns," Appl. Opt. **34**, 6417 (1995).

[63] L. J. Salazar-Serrano, A. Valencia, and J. P. Torres, "Tunable beam displacer," Rev. Sci. Instrum. **86**, 033109 (2015).

[64] G. Fowles, *Introduction to Modern Optics* (Dover Publications, 1975).

[65] M. Feldman, A. El-Amawy, A. Srivastava, and R. Vaidyanathan, "Adjustable Wollaston-like prisms," Rev. Sci. Instrum. **77**, 066109 (2006).

[66] J. Chen, B. Liu, and H. Zhang, "Review of fiber bragg grating sensor technology," Frontiers of Optoelectronics in China **4**, 204 (2011).

[67] R. Kashyap, *Fiber Bragg Gratings* (Academic Press, 1999).

[68] B. A. Tahir, J. Ali, and R. Abdul Rahman, "Fiber bragg grating based system for temperature measurements," Int.l J. of Mod. Phys. B **23**, 2349 (2009).

[69] B. Culshaw, "Optical fiber sensor technologies: opportunities and-perhaps-pitfalls," J. Light. Technol. **22**, 39 (2004).

[70] A. L. Ricchiuti, D. Barrera, K. Nonaka, and S. Sales, "Temperature gradient sensor based on a long fiber bragg grating and time waveform analysis," in "Advanced Photonics," (Optical Society of America, 2014), p. SeW3C.5.

[71] G. D. VanWiggeren and R. Roy, "Transmission of linearly polarized light through a single-mode fiber with random fluctuations of birefringence," Appl. Opt. **38**, 3888 (1999).

[72] L. J. Salazar-Serrano, A. Valencia, and J. P. Torres, "Observation of spectral interference for any path difference in an interferometer," Opt. Lett. **39**, 4478 (2014).

[73] G. C. Knee and E. M. Gauger, "When amplification with weak values fails to suppress technical noise," Phys. Rev. X **4**, 011032 (2014).

[74] C. Ferrie and J. Combes, "Weak Value Amplification is Suboptimal for Estimation and Detection," Phys. Rev. Lett. **112**, 040406 (2014).

[75] L. Vaidman, "Comment on "Weak value amplification is suboptimal for estimation and detection"," arXiv:1511.06615 [quant-ph] (2014).

[76] G. C. Knee, J. Combes, C. Ferrie, and E. M. Gauger, "Weak-value amplification : state of play," arXiv:1410.6252 [quant-ph] (2015).

[77] M. Nielsen and I. Chuang, *Quantum Computation and Quantum Information* (Cambridge University Press, 2000).

[78] L. Zhang, A. Datta, and I. Walmsley, "Precision metrology using weak measurements," Phys. Rev. Lett. **114**, 210801 (2015).

[79] C. a. Fuchs and J. D. Van Graaf, "Cryptographic distinguishability measures for quantum-mechanical states," IEEE Trans. Inf. Theory **45**, 1216 (1999).

[80] Z. Y. Ou, "Complementarity and Fundamental Limit in Precision Phase Measurement," Phys. Rev. Lett. **77**, 2352 (1996).

[81] B.-G. Englert, "Fringe Visibility and Which-Way Information: An Inequality," Phys. Rev. Lett. **77**, 2154 (1996).

[82] R. J. Glauber, "Coherent and incoherent states of the radiation field," Phys. Rev. **131**, 2766 (1963).

[83] S. Tanaka and N. Yamamoto, "Information amplification via postselection: A parameter-estimation perspective," Phys. Rev. A **88**, 042116 (2013).

[84] G. C. Knee and W. J. Munro, "Fisher information versus signal-to-noise ratio for a split detector," Phys. Rev. A **92**, 012130 (2015).

[85] J. Combes, C. Ferrie, Z. Jiang, and C. M. Caves, "Quantum limits on postselected, probabilistic quantum metrology," Phys. Rev. A **89**, 052117 (2014).

[86] J. P. Torres and L. J. Salazar-Serrano, "Weak value amplification: a view from quantum estimation theory that highlights what it is and what isn't," Sci. Rep. **6**, 19702 (2016).

[87] E. Wolf, J. T. Foley, and F. Gori, "Frequency shifts of spectral lines produced by scattering from spatially random media," J. Opt. Soc. Am. A **6**, 1142 (1989).